

ALMA MATER STUDIORUM · UNIVERSITÀ DI BOLOGNA

SCUOLA DI SCIENZE
Corso di Laurea Magistrale in Fisica

FOOT: an experiment to measure fragmentation cross sections for hadrontherapy

Monte Carlo data analysis and preliminary results
from GSI and CNAO data taking

Relatore:
Chiar.ma Prof.ssa
Gabriella Sartorelli

Presentata da:
Andrea Ubezio

Correlatore:
Dott. Roberto Spighi

Anno Accademico 2019-2020

Abstract

Hadrontherapy is a cancer treatment that exploits the irradiation with heavy charged particles. Its main advantage derives from the depth-dose profile of these particles, which release most of their energy in a narrow region inside the patient body. One of the major problems of hadrontherapy is nuclear fragmentation, which is not a fully understood phenomenon. The main goal of the FOOT experiment is to study the fragmentation of heavy-ion beams onto H-enriched targets in order to identify the produced fragments and to measure the differential cross sections of such processes of relevant interest for hadrontherapy. The use of the inverse kinematic approach should provide important information to better understand the effect of the proton/hadron therapy on patient tissues. The FOOT detector has been designed to perform high-precision identification of the produced fragments by measuring their trajectory, velocity, momentum and energy. Monte Carlo simulations and test beams are ongoing in order to verify the detector capability. In this thesis, an analysis of Monte Carlo data has been carried out in order to show the FOOT capability in identifying fragments and reconstructing the fragmentation cross sections. The data taken performed at the GSI has been also studied; the preliminary results confirm, in agreement with Monte Carlo data, an excellent precision in charge identification.

Sommario

L'adroterapia è un trattamento antitumorale che sfrutta l'irraggiamento con particelle cariche pesanti (adroni). Il vantaggio principale di questa tecnica deriva dalla particolare interazione delle particelle adroniche con la materia, le quali rilasciano la maggior parte della loro energia in una regione ristretta all'interno del corpo del paziente. Uno dei maggiori problemi dell'adroterapia è il fenomeno della frammentazione nucleare, il quale non è ancora del tutto compreso. L'esperimento FOOT ha come obiettivo lo studio di processi di frammentazione che interessano l'adroterapia, sfruttando le collisioni tra fasci di particelle cariche pesanti su target contenenti idrogeno e misurandone le sezioni d'urto. L'utilizzo della cinematica inversa permette di comprendere meglio la frammentazione nucleare e gli effetti che essa può produrre sui tessuti del paziente. Il rivelatore di FOOT è stato progettato per identificare i frammenti nucleari con precisione elevata, essendo in grado di misurarne traccia, velocità, quantità di moto ed energia. Simulazioni di Monte Carlo e test beam sono in corso per verificare le performance del rivelatore. In questa tesi viene discussa un'analisi di dati di Monte Carlo al fine di mostrare le capacità di FOOT nell'identificare i frammenti e ricostruire le sezioni d'urto di frammentazione. Un'altra analisi coinvolge i dati raccolti presso il GSI; i risultati preliminari confermano, in accordo con i dati Monte Carlo, un'eccellente precisione nell'identificazione della carica dei frammenti.

Indice

Abstract	i
Sommario	ii
Introduction	1
1 Hadrontherapy	3
1.1 Physical principles	3
1.1.1 The Bethe-Bloch formula	4
1.1.2 Bragg peak and range of the particles	7
1.1.3 Nuclear fragmentation	11
1.2 Radiobiological considerations	14
1.2.1 Dosimetric quantities	14
1.2.2 Biological effects of radiation	15
1.2.3 LET and RBE	17
1.2.4 Oxygen Enhancement Ratio	20
1.2.5 Cell survival curve	21
1.3 Treatments with heavy charged particle	25
1.3.1 History of hadrontherapy	25
1.3.2 Proton therapy	27
1.3.3 Ion therapy	34
1.3.4 Other particle therapies	38

2	The FOOT experiment	42
2.1	Motivations and aims	43
2.2	Experimental setup	46
2.2.1	Design Criteria	46
2.2.2	Electronic setup for heavy fragment detection	48
2.2.3	Emulsion setup for light fragments detection	63
2.3	Inverse kinematic approach	70
2.4	DAQ and trigger	72
3	Monte Carlo Data Analysis	75
3.1	Charge identification	76
3.2	Mass identification	81
3.2.1	Mass reconstruction methods	81
3.2.2	χ^2 and ALM fit	88
3.3	Cross section calculation	95
3.3.1	Background evaluation	98
3.3.2	Unfolding	100
3.3.3	Efficiency	105
3.3.4	Fragmentation cross sections and FLUKA cross sections comparison	105
4	GSI data analysis	118
4.1	Scintillator calibration and performance	119
4.1.1	ToF system calibration and Z reconstruction	125
4.2	Fragmentation measurement	131
4.2.1	CNAO calibration and Z identification	134
	Conclusions	138
	A General information about cross section	140
	B Analysis of data from ^{16}O (200 MeV/u) on C target	142
	C Comparison of differential cross sections and FLUKA differential cross sections	157

Elenco delle figure

1.1	Mass stopping power in function of $\beta\gamma$. In each plot one can see a β^{-2} trend at low momenta, a minimum when $\beta \sim 0.96$ and an increase at higher β values (relativistic rise).	6
1.2	Bragg curve for protons in relative stopping power; the plot shows the sharp deposition of energy known as the Bragg peak[5].	8
1.3	(a) Relative fraction of the fluence in a heavy charged particle beam as a function of depth in the <i>Continuous-Slowing-Down Approximation</i> (CSDA). (b) A more realistic behaviour of the fluence: not all particles stop at the same depth, we can see the range distribution known as <i>range straggling</i>	9
1.4	Mean range as a function of initial kinetic energy. The plot shows values related to different ions in water [7].	11
1.5	A simplified model of the nuclear fragmentation due to peripheral collisions of projectile and target nucleus [13].	13
1.6	RBE as a function of LET. The diagram illustrates why radiation with a LET of 100 keV/ μm has the greatest RBE: for this LET, the average separation between ionizing events coincides with the diameter of the DNA double helix (i.e., about 2 nm). Radiation of this quality is most likely to produce a double-strand break from one track for a given absorbed dose [17].	18
1.7	Comparison between different particles RBE curves as functions of LET [18].	19

1.8	<i>Oxygen enhancement ratio (OER) as a function of Linear Energy Transfer (LET). The vertical line ($LET = 10 \text{ keV}/\mu\text{m}$) separates low-LET values from high-LET values [21].</i>	21
1.9	ionization and free radicals formation induced by high-LET and low-LET radiations. In a high-LET regime, subsequent ionizations are separated by a distance of about 10^2 - 10^3 pm, while the formation of the H^\bullet radical occurs about 15 nm away from the primary ionization process; in this case, the $\text{OH}^\bullet + \text{OH}^\bullet$ recombination (that produce hydrogen peroxide) is favoured. In a low-LET regime, ionizations occur every tens of nm, thus OH^\bullet and H^\bullet couples are closer than two OH^\bullet radicals, then their recombination (that produce H_2O) is favoured.	22
1.10	Ionization density in a medium irradiated by X-rays (a) and high LET particles (b). The small circles represent biological targets and the dots represent ionizations produced along the tracks [22]	23
1.11	Cell survival as a function of dose for densely and sparsely ionizing radiation. The fraction of cells surviving is plotted on a logarithmic scale against dose on a linear scale [25].	24
1.12	Representation of the RBE as the ratio between dose values from different radiation given a fixed surviving fraction value. According to linear quadratic model, RBE is maximal when dose $\rightarrow 0$. If the fractional dose increases, the RBE converges to a minimal value [27].	25
1.13	Absorbed dose D as a function of depth z in water from an unmodulated (pristine) proton Bragg peak produced by a broad proton beam with an initial energy of 154 MeV. The various regions that are labeled are defined in the text. Note that the electronic buildup region, which spans only a few millimeters, is not visible in this plot. This type of dose distribution is clinically useful because of the relatively low doses delivered to normal tissues in the sub-peak and distal-falloff regions with respect to the target dose delivered by the peak [29].	28

1.14	(a) Proton fluence $I(0, x)$ along the beam central axis as a function of the depth x in water. Curves are shown for beams with circular cross sections with radius between 1 and 4 mm. Some protons are lost because of scattering events that deflect them from the central axis. This is increasingly observed for small beams and at large depths. (b) The corresponding central-axis absorbed-dose curves. Note how the fluence depletion reduces the absorbed dose at the peak with respect to the entrance dose [30].	30
1.15	Absorbed dose D as a function of depth z in water from a spread-out Bragg peak (SOBP) (uppermost curve) and its constituent pristine Bragg peaks (lower curves; for clarity, all but the deepest pristine Bragg peak are only partly drawn). In many cases, the clinical target volume is larger than the width of a pristine Bragg peak. By appropriately modulating the proton range and fluence of pristine peaks, the extent of the high-dose region can be widened to cover the target volume with a uniform dose [29].	31
1.16	Absorbed dose D as a function of depth z in water from a spread-out proton Bragg peak (SOBP). Various locations and regions that are indicated on the plot are defined in the text. Note that the electronic buildup region, which spans only a few millimeters, is not visible in this plot [29].	32
1.17	The total proton-induced non-elastic nuclear reaction cross section in oxygen versus proton energy, showing a threshold corresponding to the Coulomb barrier at approximately 6 MeV [31].	33
1.18	Measured Bragg curves of ^{12}C ions stopping in water [51].	36
1.19	Bragg curve for 670 MeV/u ^{20}Ne ions in water measured at GSI (circles) and calculated contributions of primary ions, secondary and tertiary fragments [52].	37
1.20	Cross-section for photon scattering from carbon showing the contributions of photoelectric, elastic (Rayleigh), inelastic (Compton) and pair-production cross sections to the total cross sections. Also shown are the experimental data (open circles). The energy of photons used in conventional radiotherapy starts from few tens of keV up to ~ 10 MeV [54].	39

1.21	Depth-dose distributions from X-rays, proton beams, and carbon ion beams superimposed with each other for comparison [55].	40
2.1	illustrative image of the expected relative impact of the target fragmentation in the entrance and in the peak regions as compared to the effect of the inactivation by ionization [61].	43
2.2	Full spectra of fragments from target media in the case of a prostate irradiation with protons of 160 MeV, integrated in the complete range of beam propagation [63].	44
2.3	Schematic view of the FOOT electronic setup [69].	49
2.4	Picture of the Start Counter mechanical frame.	50
2.5	Technical draw of the beam monitor [69].	51
2.6	Photo of the inside of the Beam Monitor.	52
2.7	3D model of the two magnets in Halbach configuration designed for the magnetic spectrometer [69].	53
2.8	Magnetic field intensity B as a function of z along the beam central axis ($x = y = 0$). The plot shows the double gaussian trend produced by two separated Halbach magnets (simulation performed with the OPERA code version 16R1) [69].	54
2.9	Target and vertex tracker geometrical scheme (left) and a M28 pixel sensor picture (right) [69].	55
2.10	Upper left and right panel: beam profile in the two M28 sensors (units on both axes are in μm). Bottom panel: reconstructed angular divergence of the beam in mrad [69].	56
2.11	Inner tracker scheme. On the right we see how the four modules are located in the global structure. Each module has two connectors, in red and green color, respectively on the front and back side of the ladder [69].	57
2.12	Picture of a MSD layer prototype.	58
2.13	Picture of a SCN bar prototype (left) and the entire scintillator (right). .	59
2.14	STC-SCN measurement of the time of flight performed at the GSI test beam (April 2019) with the electronic setup. The standard deviation of the fitted distribution (boxed in red) represents the time resolution. . . .	60

2.15	Schematic view of the CAL crystals setup.	61
2.16	Energy resolution of the BGO crystals as a function of energy for different particle beams obtained at GSI and CNAO.	62
2.17	Emulsion spectrometer setup inside the FOOT detector [69].	64
2.18	Schematic overview of the ECC layout (not to scale) [69] (è quello di OPERA?).	65
2.19	Scheme of the ES Section 1: vertex and tracking detector [69].	66
2.20	Scheme of ES section 2: charge identification detector.	67
2.21	Scheme of ES section 3 dedicated to the momentum measurement [69].	67
2.22	Scheme of the tracks reconstruction: a micro-track consists of a sequence of aligned clusters in one of the two layers (top or bottom), while a base-track is constituted by geometrically aligned top and bottom micro-tracks. [69].	68
3.1	Energy resolution in the scintillator as a function of the energy deposition of the fragment.	78
3.2	Time resolution as a function of the fragment charge.	79
3.3	Charge number Z of fragments produced in the fragmentation in linear scale (a) and in logarithmic y scale (b). The element relating to the charge peak is indicated in blue.	80
3.4	Mass numbers A_1 from 1 to 16 reconstructed with the ToF and momentum measurement.	84
3.5	Mass numbers A_2 from 1 to 16 reconstructed with the kinetic energy and momentum measurement.	85
3.6	Mass numbers A_3 from 1 to 16 reconstructed with the ToF and kinetic energy.	86
3.7	Distribution of the ratio between the measured kinetic energy (energy deposition in the scintillator plus energy deposition in the calorimeter) and the true kinetic energy (generated in the simulation) of the fragments produced in the fragmentation reaction $^{16}O + C_2H_4$	89
3.8	Mass numbers distributions obtained with the standard χ^2 minimization method.	91

3.9	Cuttet distributions ($\chi^2 < 5$ events only) of the mass number obtained with the standard χ^2 minimization method.	92
3.10	Mass resolution as a function of the mass number obtained with different mass reconstruction methods.	94
3.11	Mass number of carbon fragments in different kinetic energy range. . . .	97
3.12	Migration histograms for the background evaluation of carbon fragments in different kinetic energy ranges.	99
3.13	Production yields (blue lines) and background events (red lines) as a function of kinetic energy of carbon isotopes.	101
3.14	Production yields background subtracted as a function of kinetic energy of carbon isotopes.	102
3.15	Migration histograms of kinetic energy used in the unfolding procedure. .	103
3.16	Distributions of yields background subtracted (violet) and unfolded distributions (green) with respect to kinetic energy of carbon isotopes.	104
3.17	Reconstruction efficiency as a function of kinetic energy of each carbon isotope.	106
3.18	Energy differential cross section for the production of carbon isotopes in fragmentation reaction induced by a 200 MeV/u oxygen-16 beam impinging on a C ₂ H ₄ target.	108
3.19	Energy differential cross section for the production of carbon isotopes in fragmentation reaction induced by a 200 MeV/u oxygen-16 beam impinging on a C target.	110
3.20	Energy differential cross section for the production of carbon isotopes in fragmentation reaction induced by a 200 MeV/u oxygen-16 beam impinging on a H target.	112
3.21	Ratio between the reconstructed total number of fragments for each carbon isotope and the total number of fragments generated in the simulation (¹⁶ O on C ₂ H ₄).	114
3.22	Ratio between the reconstructed total number of fragment for each carbon isotope and the total number of fragments generated in the simulation (¹⁶ O on C).	115

3.23	Comparison between the energy differential cross sections obtained in this analysis (blue) and the FLUKA cross sections used in the MC simulation (red), relating to the production of ^{12}C fragments in different targets (C_2H_4 , C and H).	116
4.1	Schematic view of the electronic setup used at the GSI test beam. . . .	118
4.2	Schematic view of the scintillator used at the GSI test beam. The highlighted bars are those that have been calibrated at GSI with a 400 MeV 16-oxygen beam.	119
4.3	Mean collected charge at the two ends of a scintillating bar as a function of the position, for a proton beam with the fixed energy of 170 MeV. The 0 position represent the center of the bar. Solid lines represent the fit to the data with eq. 4.2 [91].	120
4.4	Scheme of the scintillator bar read-out. A signal charge independent by the particle hit position can be obtained by multiplying the signal charge at the left end (Q_{left}) by the signal charge at the right end (Q_{right}). . . .	121
4.5	(a) Distributions of signal charge from bar 11 and bar 14 of the rear layer of the scintillator obtained with ^{16}O particles (400 MeV/u); F_{eq} is the equalisation factor. (b) Same distributions after equalisation. The equalisation value has been arbitrarily chosen equal to 70.	122
4.6	Distributions of equalised signal charge from bar 14 of the rear layer. . .	122
4.7	Energy deposited by ^{16}O particles (400 MeV/u) in the bar 14 of the scintillator.	123
4.8	Distribution of the signal charge from the scintillator obtained with a 400 MeV/u ^{16}O beam. The signal charge of each event is given by the sum of the charge collected in the two layers.	125
4.9	Distribution of time measured with the bar 14 of the rear layer of the scintillator before (a) and after the equalisation (b). This distribution has been obtained by detecting only ^{16}O (400 MeV/u) particles coming from the test beam. 10.44 ns is the time that a beam particle takes to travel from the Start Countuer to the scintillator; all the bars has been equalised at this time by subtracting the corresponding time offset.	126

4.10	Distribution of time of flight of beam particles from the intended target position to the scintillator. This time measurement has been obtained as the mean value of the times measured by the two layer of the scintillator.	127
4.11	Z Distribution obtained with the energy loss and the ToF measured by the bar 14 of the scintillator.	129
4.12	Distribution of the charge Z obtained from the scintillator measurements performed on 400 MeV/u ^{16}O particles.	131
4.13	Scheme of the ghosting phenomenon in the scintillator: two impinging fragments produce four bar intersections, as the detector has been hit by four particles.	132
4.14	(a) Distribution of the signal charge from the scintillator obtained with fragmentation events induced by ^{16}O (400 MeV/u) impinging on a C target. (b) Same distribution, but in linear scale; the oxygen peak has not been included in order to better appreciate the other peaks.	133
4.15	Calibration of three scintillator bars. (a) Calibration performed at CNAO with proton and carbon beams. (b) Calibration performed with CNAO and GSI data from proton, carbon and oxygen beams. (c) Calibration performed with CNAO and GSI data; the oxygen point is not in agreement with the other data, therefore it is not included in the fit.	135
4.16	Charge Z of the fragments produced at the GSI data taking by using a 400 MeV/u ^{16}O beam impinging on a C target.	136
B.1	Charge Z distributions of fragments produced in the fragmentation.	143
B.2	Charge Z distributions of fragments produced in the fragmentation in logarithmic y scale.	143
B.3	Mass numbers A_1 from 1 to 16 reconstructed with the ToF and momentum measurement.	144
B.4	Mass numbers A_2 from 1 to 16 reconstructed with the kinetic energy and momentum measurement.	145
B.5	Mass numbers A_3 from 1 to 16 reconstructed with the ToF and kinetic energy.	146

B.6	Mass number distributions obtained with the standard χ^2 minimization method.	147
B.7	Cuttet distributions ($\chi^2 < 5$ events only) of the mass number obtained with the standard χ^2 minimization method.	148
B.8	Mass resolution as a function of the mass number obtained with different mass reconstruction methods.	149
B.9	Mass distributions of carbon fragments in different kinetic energy range. .	150
B.10	Migration histograms for the background evaluation of carbon fragments indifferent energy ranges: true mass number A vs reconstructed mass number A.	151
B.11	Production yields (blue lines) and background events (red lines) as a function of kinetic energy (MeV/u) of carbon isotopes.	152
B.12	Production yields background subtracted as a function of kinetic energy (MeV/u) of carbon isotopes.	153
B.13	Migration histograms of kinetic energy (MeV) used in the unfolding procedure: true kinetic energy vs reconstructed kinetic energy.	154
B.14	Production yields background subtracted before (violet lines) and after (green lines) the unfolding procedure as a function of kinetic energy (MeV/u) of carbon isotopes.	155
B.15	Reconstruction efficiency as a function of kinetic energy (MeV/u) of each carbon isotope.	156
C.1	Differential cross section (mbarn/MeV) as a function of kinetic energy (MeV/u). The blue markers are the differential cross section found in this analysis, the red markers are the differential cross sections used in the FLUKA simulation. The plots refer to the carbon isotopes produced by an oxigen-16 beam (200 MeV/u) impinging on a C ₂ H ₄ target.	158
C.2	Differential cross section (mbarn/MeV) as a function of kinetic energy (MeV/u). The blue markers are the differential cross section found in this analysis, the red markers are the differential cross sections used in the FLUKA simulation. The plots refer to the carbon isotopes produced by an oxigen-16 beam (200 MeV/u) impinging on a C target.	159

C.3	Differential cross section (mbarn/MeV) as a function of kinetic energy (MeV/u). The blue markers are the differential cross section found in this analysis, the red markers are the differential cross sections used in the FLUKA simulation. The plots refer to the carbon isotopes produced by an oxygen-16 beam (200 MeV/u) impinging on a H target.	160
-----	---	-----

Elenco delle tabelle

1.1	weighting factor of different type of radiation; the weighting factor for neutrons can range from ~ 3 up to 20 and it is given by a continuous function of the neutron energy, as discussed in [14].	15
2.1	Average data for target fragments from a 180 MeV proton beam in water, estimated according to a semi-empirical formula.	45
2.2	Overview of the FOOT research program. PMMA refers to Poly(methyl methacrylate) whose chemical formula is $C_5O_2H_8$	46
2.3	Current resolution of the detectors of the FOOT electronic setup.	63
2.4	DAQ components, rates and bandwidths	73
3.1	List of fragments produced in a fragmentation reaction induced by an oxygen-16 beam impinging on a C_2H_4 target.	76
3.2	Scintillator characteristics included in the Bethe-Block formula for the fragment charge determination.	77
3.3	Mean values, standard deviations and resolutions of the charge distributions showed in fig. 3.3	80
3.4	List of the mainly produced isotopes for each charge in a fragmentation reaction induced by an oxygen-16 beam impinging on a C_2H_4 target. These isotopes have been selected to study the mass identification performance of the apparatus.	81
3.5	Resolution of the quantity measured with the simulated FOOT apparatus.	83

3.6	Mean values, standard deviations and resolutions of the mass number distributions obtained with the three methods (A_1 , A_2 , A_3) discussed in section 3.2.1	87
3.7	Mean values, standard deviations and resolutions of the mass number distributions obtained with the standard χ^2 -fit method (top table) and with the application of the $\chi^2 < 5$ selection (bottom table).	93
3.8	Energy ranges within which the energy differential cross section has been calculated.	96
3.9	Differential cross sections (mbarn/MeV) in each considered kinetic energy range for carbon isotopes produced in the fragmentation reaction induced by ^{16}O beam on C_2H_4 target.	107
3.10	Differential cross sections (mbarn/MeV) in each considered kinetic energy range for carbon isotopes produced in the fragmentation reaction induced by ^{16}O beam on C target.	109
3.11	Differential cross sections (mbarn/MeV) in each considered kinetic energy range for carbon isotopes produced in the fragmentation reaction induced by ^{16}O beam on H target.	111
3.12	Total production cross sections (mbarn) of carbon isotopes in fragmentation processes induced by ^{16}O beam on different target. σ_1^{tot} refers to the total cross section obtained by integrating the differential cross sections given in fig. 3.18-3.20 ; σ_2^{tot} has been obtained with the same analysis as described in chapter 3, but performed in a single wide energy range including all the kinetic energy of the produced fragments; σ_2^{tot} is the cross section used in the FLUKA MC simulation.	117
4.1	Equalisation factors of each equalised bar of the scintillator; mean, standard deviation and resolution of the related signal charge distribution obtained with a 400 MeV ^{16}O beam.	124
4.2	Time offset of each calibrated bar; mean, standard deviation and resolution of the ime of flight of 400 MeV ^{16}O particles measured with each scintillator bar.	128

4.3	Mean, standard deviation and resolution of Z distributions obtained from the measures performed by each scintillator bar on a 400 MeV ^{16}O beam. .	130
4.4	Energy lost inside the scintillator layers by the particles used at CNAO for calibration.	134
4.5	Fit parameters of the Birks' function for each calibrated bar of the scintillator.	137

Introduction

According to the *World Health Organization*, cancer is one of the most deadly diseases in the world. Nowadays, tumors are treated with different techniques, including surgery, chemotherapy, radiotherapy and immunotherapy. Radiotherapy now contributes to the treatment of about 23% of all cancer patients, used alone or in combination with surgery, chemotherapy or immunotherapy. In addition to the well-established photon radiotherapy, in the last decade the number of patients treated with heavy charged particle beams has increased. This technique is called *hadrontherapy* and its main advantage derives from the depth-dose profile of charged particles, which is characterised by a low-dose entrance channel and by a following narrow region, the *Bragg peak*, where the maximum of the dose release is reached. The Bragg peak depth depends on the beam energy, which is tunable in the particle accelerators that provides the therapeutic beam. By matching the Bragg peak with the depth of the tumor inside the patient's body, it is possible to affect the cancer cells and, at the same time, to preserve the surrounding healthy tissue.

At present, one of the major problem of hadrontherapy is the nuclear fragmentation, which is not a fully understood phenomenon whose effects can change the dose profile: nuclear reaction inside the patient's body may occurs, resulting in the emission of nuclear fragments, whose type and energy differ from those of primary particles. Both the projectile and the target nuclei can undergoes fragmentation: in heavy ion treatments, the fragments of the projectile (with the same velocity but with lower mass than the projectile itself) can travel farther and can deliver a non-negligible dose beyond the Bragg peak, harming the healthy tissue; in proton therapy the projectile can not fragment at therapeutic energy, but the fragmentation of target nuclei could be an issue, since low energy fragments, consequently with short range ($\sim \mu\text{m}$), are produced, resulting in a

local dose deposition which mainly involves the entrance channel.

FOOT (**F**ragmentati**O**n **O**f **T**arget) is a fixed target experiment equipped with a multipurpose detector for the detection and identification of heavy charged particles. The main goal of this experiment is to fill the lack of experimental data concerning fragmentation cross sections, which are not already studied for the nuclei of the human tissue (mainly H, C and O) in the therapeutic energy range (between tens and hundreds of MeV per nucleon). The main challenge is to investigate target fragmentation processes in proton therapy, since the very short range of the emitted fragments does not allow them to escape the experimental target and, then, to be detected. In order to overcome this problem, FOOT adopts an inverse kinematic approach, which consists in switching the target and the projectile roles, so as to produce fragments with a forward boost. FOOT can also carry out studies on projectile fragmentation by exploiting the ordinary direct kinematics.

In the first chapter of this thesis, the principles of hadrontherapy and interaction of radiation with matter, with particular regard to the radiobiological aspects, are discussed. Furthermore, the nuclear fragmentation phenomenon is introduced. The second chapter describes in detail the FOOT apparatus and its components, showing the tests performed and the resolutions obtained on the various detectors. The third chapter shows an analysis performed on data from a Monte Carlo simulation of the FOOT apparatus, while in chapter 4, two data taking performed at the GSI and CNAO facilities are discussed and analysed. The purpose of this work is to develop an analysis software able to manage the data produced by the experiment, to study the detector precision in particle identification and to obtain the final cross section measurements. The analysis of real data, acquired at GSI, represent the first confirmation of the FOOT capability to detect and identify the fragments with appropriate resolution.

Capitolo 1

Hadrontherapy

Hadrontherapy is an oncological technique that uses protons and ions as projectiles in order to kill cancer cells. This therapy is particularly useful in situations in which standard treatments, like surgery, chemotherapy or the conventionally radiotherapy (that makes use of X-rays and γ -rays), cannot be used, as, for example, cancer located inside or near sensitive organs.

In this chapter the main aspects of hadrontherapy, its working principles and applications are discussed.

1.1 Physical principles

In this section we will see which basic interactions occur when heavy charged particles pass through matter and what effects can be produced. Heavy charged particles (with mass $M \gg m_e$, where m_e is the electron mass) interact with matters in terms of electrons and nuclei, so processes that can occur are both electromagnetic and nuclear. In general, two principal electromagnetic features characterize the passage of heavy charged particles through matter: a loss of energy by the incident particle (inelastic collisions with the atomic electrons) and a deflection of the particle from its original direction (elastic scattering from nuclei). These two phenomena may occur many times in a unit path length in matter. For what concern the nuclear interactions, heavy particles may

also make strong interaction directly with nuclei. This process might produce secondary particles.

While the single particle interactions can be described at the atomic or nuclear level, at the macroscopic level the most important quantity is the *stopping power* that measure the energy loss per unit path length. The stopping power depends on the properties of the charged particle, such as mass, charge, velocity and energy, as well as on the properties of the absorbing medium, such as its density and atomic number.

Below in this section we will discuss the energy loss of a heavy charged particle in matter due to electromagnetic interaction, described by the Bethe-Bloch formula, and we will also see in details the nuclear fragmentation process that leads to secondary particles.

1.1.1 The Bethe-Bloch formula

The e.m. interaction represent the primary cause of energy loss of an heavy charged particle travelling in matter, in particular, this loss is mainly due to inelastic collisions with the atomic electrons. In these processes the energy transfer leads to an excitation (*soft collision*) or ionization (*hard collision*) of the atom. The amount of energy transferred in each collision is a small fraction of the total kinetic energy of the particle, however the number of collisions per unit path length (in dense matter) is large, than a substantial cumulative energy loss could be observed.

Inelastic scattering from nuclei also occurs frequently although not as often as electron collisions. The amount of energy transferred in this way depends on the ratio between the mass of the impinging particle and the mass of the nuclei that constitute the medium. The energy lost is in any case a small fraction of the overall energy loss, since the probability of nuclear scattering is much lower than the probability of interactions with the electrons (the ratio between scattering cross sections is $\sigma_{\text{nucleus}}/\sigma_{\text{atom}} \simeq 10^{-8} - 10^{-10}$)¹. Nevertheless, the atomic nuclei of the medium are responsible for elastic Coulomb scat-

¹To estimate this ratio we used a classical approach that considers particles as hard spheres. In this way, the cross section can be obtained using the relation $\sigma_{\text{nucleus(atom)}} = \pi(2r_{\text{nucleus(atom)}})^2$, where $r_{\text{nucleus(atom)}}$ is a typical nuclear (atomic) radius.

tering that are the main cause of the deflection of the incident particle with respect to its original motion.

So, during its walk through an absorbing medium, a charged particle experiences a large number of interactions before its kinetic energy is completely lost. In each interaction the charged particle may lose some of its kinetic energy and its path may be altered. The energy δE lost in a collision depends on the characteristics of the particle as well as the absorber. However, even with the same particle and medium characteristics, the energy lost δE isn't the same in every collision, but depends on the scattering kinematics. Anyhow, we can consider a statistical quantity dE , based on the average energy loss that does not take into account the kinematics of each process.

The rate of energy loss (typically expressed in MeV) per unit of path length (typically expressed in cm) in an absorbing medium is called *linear stopping power* ($-dE/dx$) [1]. The stopping power for heavy charged particles in matter was first calculated by Bohr using a classical approach [2] and later by Bethe and Bloch using quantum mechanics [3, 4]. The formula obtained by Bethe, Bloch and other physicists is

$$-\frac{dE}{dx} = 2\pi N_A r_e^2 m_e c^2 \rho \frac{Z}{A} \frac{z^2}{\beta^2} \left[\ln \left(\frac{2m_e \gamma^2 \beta^2 c^2 W_{\max}}{I^2} \right) - 2\beta^2 - \delta - 2\frac{C}{Z} \right] \quad (1.1)$$

In this formula we can see a first constant term consisting of the classical electron radius ($r_e = 2.8179403227(19) \times 10^{-13}$ cm), the electron mass ($m_e = 9.1093837015(28) \times 10^{-28}$ g), the Avogadro's number ($N_A = 6.0221409 \times 10^{23}$ mol⁻¹) and the speed of light in vacuum ($c = 299.792458 \times 10^{10}$ cm/s). Then, there is a part depending on the characteristics of the medium (atomic number Z , atomic weight A and density ρ) and a part depending on beam characteristics (the charge of the incident particle z , in unit of e , and its velocity $\beta = v/c$). The logarithmic term depends on beam quantities (such as β and $\gamma = 1/\sqrt{1 - \beta^2}$), the mean excitation potential I and the maximum energy transfer in a single collision W_{\max} .

$$W_{\max} = \frac{2m_e c^2 \beta^2 \gamma^2}{1 + 2\frac{m_e}{M} \sqrt{1 + \beta^2 \gamma^2} + \left(\frac{m_e}{M}\right)^2} \quad (1.2)$$

when M is the mass of the incident particle. If $M \gg m_e$ (that is the case of heavy

charged particles), eq. 1.2 becomes $W_{\max} = 2m_e c^2 \beta^2 \gamma^2$. The last two terms in eq. 1.1 represent the density effect correction δ and the shell correction C . The *density effect correction* is needed to take into account the polarization effect due to a charged particle travelling in a medium full of electrons. Electrons far from the particle path are shielded, so the effective dE/dx is lower. This correction increases with the density of medium density and with the beam energy. The *shell correction* becomes important when the energy of the incident particle is low enough to make the particle velocity comparable or lower than the electrons velocity in the medium. In this situation we can no longer assume that the electron is at rest when the interaction happens, therefore the transferred energy is slightly reduced. Both corrections are negligible in the energy range useful for hadrontherapy.

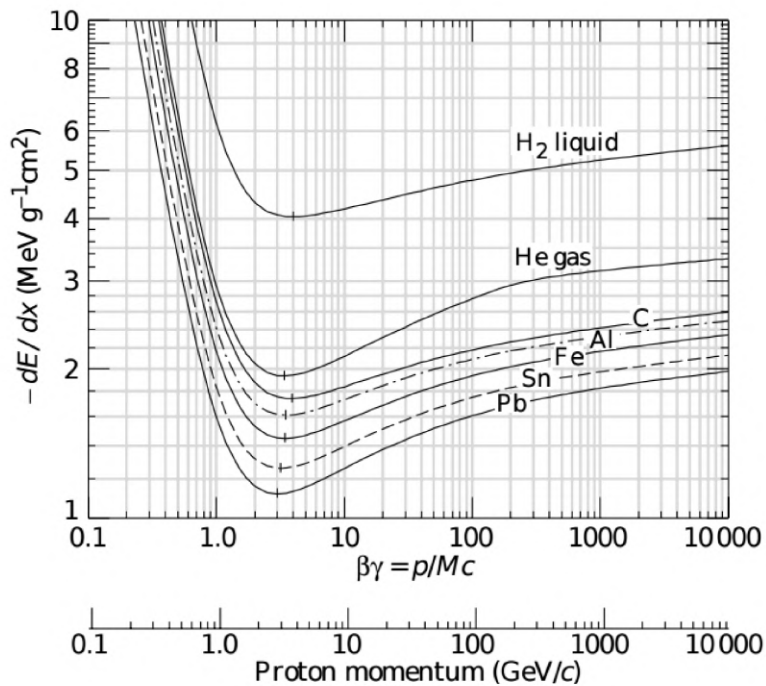


Figura 1.1: Mass stopping power in function of $\beta\gamma$. In each plot one can see a β^{-2} trend at low momenta, a minimum when $\beta \sim 0.96$ and an increase at higher β values (relativistic rise).

Dividing the Bethe-Bloch by the absorbing material density, the *mass stopping power*

is obtained. This quantity is more convenient because the unit path length is now expressed in $\text{g}\cdot\text{cm}^{-2}$ and it doesn't depend on the density of the medium. In figure 1.1 the mass stopping power is shown as a function of the $\beta\gamma$ value of the incident particle for different absorbing materials; one can also see the momentum scale of proton on the x axis.

For a non relativistic particle, dE/dx is dominated by the overall factor $1/\beta^2$ and decreases with increasing velocity until a minimum is reached at $\beta \sim 0.96$. Particles at this minimum point are usually referred to as *Minimum Ionizing Particles* (MIP). As the energy increases beyond the MIP point, dE/dx also increases due to the logarithmic contribution in the Bethe-Bloch formula; this trend is called *relativistic rise*. It is important to notice that hadrotherapy uses proton beams with kinetic energy of ~ 0.2 GeV, which corresponds to a proton momentum of ~ 0.66 GeV, thus, we are in the β^{-2} -dependent region of the Bethe-Bloch.

When different projectiles with the same velocity are compared, the charge z is the only factor that changes outside the logarithmic term, so particles with greater charge have a larger specific energy loss. Instead, studying dE/dx for different materials as absorbers, it can be pointed out its main dependence on the electron density of the medium: the higher is the material density, the higher is the energy loss. If we consider the mass stopping power (as shown in fig. 1.1, there is no more dependence on the material density, thus the only factor that takes into account the properties of the material is the Z/A ratio.

Taking into account all the above considerations, it can be seen that a particle deposits much more energy when its velocity is low. This is the case of a very low energy particle or a particle near the end of its path, which has therefore lost much of its initial energy.

1.1.2 Bragg peak and range of the particles

As we saw in the previous section, a particle travelling through an absorbing medium progressively slows down, because of energy loss, as it goes deep in the material and when a particle is close to rest it releases most of its energy. Thus, we can reinterpret the Bethe-Bloch trend considering the stopping power as a function of depth.

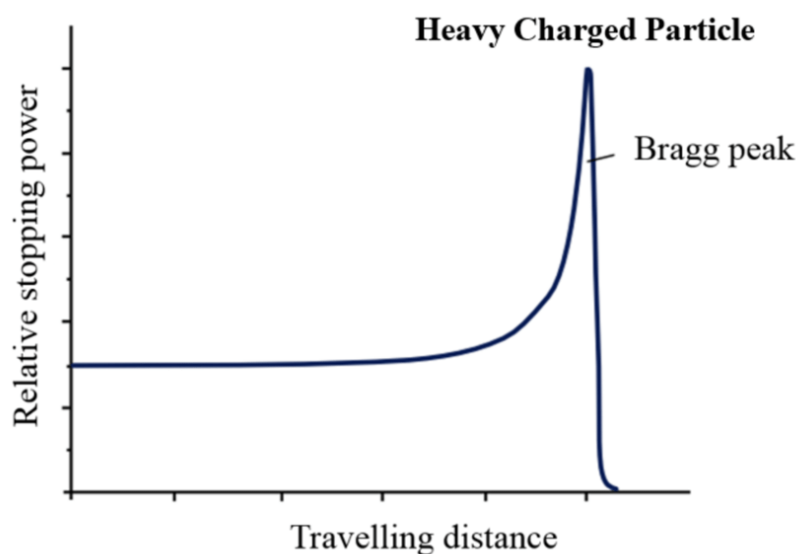


Figura 1.2: Bragg curve for protons in relative stopping power; the plot shows the sharp deposition of energy known as the Bragg peak[5].

Figure 1.2 shows the stopping power for a proton beam with respect the crossed path, also called *Bragg curve*. We can easily see how the dE/dx rises at a certain travelling distance and then it decreases abruptly. This sharp region, known as *Bragg peak*, occurs at a specific depth, depending on the beam energy, that corresponds to the range of the beam particles. In an oncological perspective, this means that, knowing the depth of the tumor in the patient's body, we can set the energy of the beam in order to send most of the ionization power into the tumor and protect the surrounding healthy tissue.

Later (see section 1.3.2 and 1.3.3) we will see in details some Bragg curve from different type of particle beams considering the radiobiological aspects, while below we will define the particle range and see how to find it.

The range is an important parameter because it gives information about the longitudinal energy transfer in the material. We can define the *mean range* as the average length that the particle travels inside an absorbing medium before running out of kinetic energy. Considering a monoenergetic beam, we can assume that it deposits a continuous and constant amount of energy per unit of path length equal to its stopping power. In this *Continuous-Slowing-Down Approximation* (CSDA), all the particles run out of ener-

gy at the same depth, equal to the *CSDA range*. Figure 1.3, curve (a), show this ideal behaviour in terms of fraction of beam particles as a function of depth.

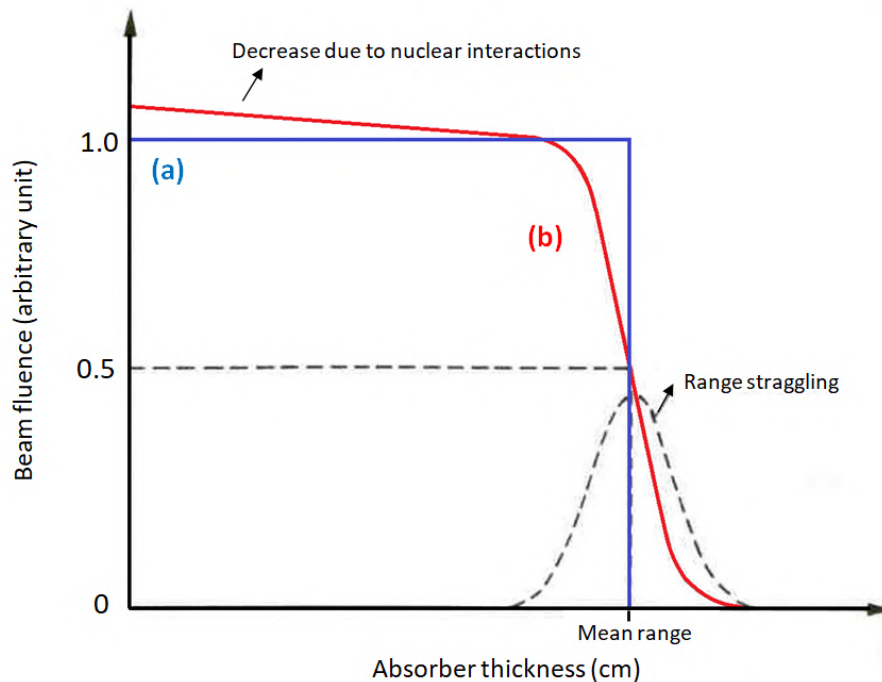


Figure 1.3: (a) Relative fraction of the fluence in a heavy charged particle beam as a function of depth in the *Continuous-Slowing-Down Approximation* (CSDA). (b) A more realistic behaviour of the fluence: not all particles stop at the same depth, we can see the range distribution known as *range straggling*.

However, the energy loss undergoes statistical fluctuations, so the range does the same: not all particles run out of energy at the same depth, but there is an approximately gaussian spread in the distribution of the stopping point (figure 1.3, curve (b)), to which we refer as *range straggling*. In this latter description, we can define the range as the depth at which the beam fluence is half of its initial value.

Another phenomenon to consider, although less important, is the nuclear interaction that a particle can make at any depth, this results in a slight linear decrease of the beam intensity before reaching the stopping depth, since the beam is depleted because of the particles lost in nuclear processes.

The CSDA range R is related to the stopping power and the initial kinetic energy (E_0) of the projectile particle:

$$R(E_0) = \int_0^{E_0} \left(\frac{dE}{dx} \right)^{-1} dE \quad (1.3)$$

Accordingly to eq. 1.3, as the kinetic energy of the primary particle increases, also the range becomes longer. The range dependence on kinetic energy follows a very simple power law, as realized by Bragg and Kleeman [6] early in the last century:

$$R(E_0) = \alpha E_0^p \quad (1.4)$$

where α is a material-dependent constant and p depends on the incident particle type.

The ranges of different ion with equal initial kinetic energy E per atomic mass unit and crossing the same absorber are related as follows:

$$R_2 \frac{z_2^2}{m_2} = R_1 \frac{z_1^2}{m_1} \quad (1.5)$$

This means that, given a certain energy per unit mass, heavier ions have shorter range than lighter ones (fig. 1.4). In fact, according to eq. 1.1, the energy loss is proportional to z^2 , so they lose a greater amount of energy per path length. For instance, being equal the energy per nucleon, the proton range is approximately three times longer than the range of ^{12}C , while protons and ^4He ions have same range, since the z^2/m ratio is the same.

In the field of cancer therapy, a particle beam passes through inhomogeneous tissues composed of different materials. Obtaining a good estimate of range using eq. 1.3 is not an easy task. Fortunately, there are approximations that allow us to simplify the calculation; one example is the *Bragg-Kleeman approximation* (derived from CSDA) which assumes that the mass stopping power for a compound material is [8]

$$\frac{1}{\sigma} \left(\frac{dE}{dx} \right)_{\text{tot}} = \sum_i \frac{W_i}{\sigma_i} \left(\frac{dE}{dx} \right)_i \quad (1.6)$$

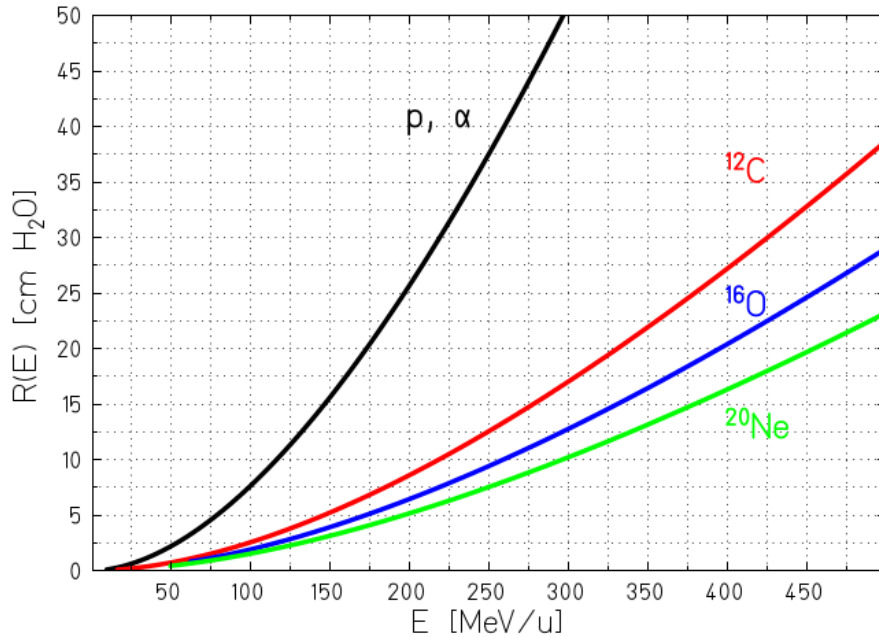


Figura 1.4: Mean range as a function of initial kinetic energy. The plot shows values related to different ions in water [7].

where W_i corresponds to the fraction of atom of the i -th element that composes the absorbing material, σ_i is the density of the i -th element and σ is the overall density of the whole absorbing medium.

Other range calculation strategies and approximations are discussed in [9].

1.1.3 Nuclear fragmentation

When an heavy charged particle travels into an absorber medium, nuclear interactions also occurs. These processes strongly depend on the energy of the incident particle: in a collision on a target nucleus, if the projectile particle energy is below the coulomb barrier, the dominant process is the Coulomb scattering, while strong interactions occurs with very low probability only through quantum tunneling effects [10]; if the energy is over the coulomb barrier, and if the impact parameter is lower than a critical value [11], the strong interaction becomes dominant. Protons and ions used in hadrontherapy have

energy between $\sim 200 - 400$ MeV/u (MeV per nucleon), therefore they are allowed to make nuclear reactions and fragmentation.

The *nuclear fragmentation* is a nuclear collision between the projectile and the target nuclei, that leads to their destruction and to the production of other nuclei (fragments). Depending on the impact parameter², this process can be divided in two categories: *central collisions*, that lead to the complete disintegration of both nuclei, resulting in a multitude of secondary fragments (dissipative processes), and *peripheral collisions*, that involve only a few nucleons (quasielastic processes) and that are described by the simplified *abrasion-ablation model* proposed by Serber [12]. In hadrontherapy, since the energie used is such as to make the second process more probable, the interest is focused on the peripheral collisions.

In case we are using protons as projectile, we have to consider that they can not fragment at therapeutic energy, the only fragmentation that occurs is the target one. In case we are using heavier ions as projectile, nuclear interactions are allowed to produce both target and projectile fragmentation.

In a peripheral collision, the fragmentation process happens in two steps, according to the Serber model. In the first stage (*abrasion*) nucleons are involved: they gain a certain amount of energy due to the collision and they are expelled by the target and, in the same way, some nucleons are expelled from the projectile (in the case of a $Z > 1$ ion). The second stage lasts about 10^{-18} - 10^{-16} s and it is characterized by thermalization and de-excitation of the remaining nuclei that, depending on their mass and excitation energy, can happen in the following ways.

- *γ -emission*: the excited nucleus dissipate its residual energy by emitting photons.
- *Nuclear evaporation*: light fragments ($Z < 2$) escape from the excited residual nucleus.
- *Fermi break-up*: in nuclei of mass $A < 16$ the excitation energy can exceed the binding energy of some fragmentation channels and this cause the break of the nucleus into lighter fragments; this process is relevant in radiotherapy since $A < 16$ elements represent the majority of human body atoms.

²distance in the trasverse plane between the projectile and the target

- *Fission*: the residual nucleus breaks into two separate fragments; this process is relevant only for very heavy nuclei (usually $Z > 65$) that are not present in the human body in normal condition, thus it is negligible for hadrontherapy purpose.

During the abrasion stage, nucleons in the overlapping region also generate the so called *fireball*, which evaporate during the ablation stage (figure 1.5).

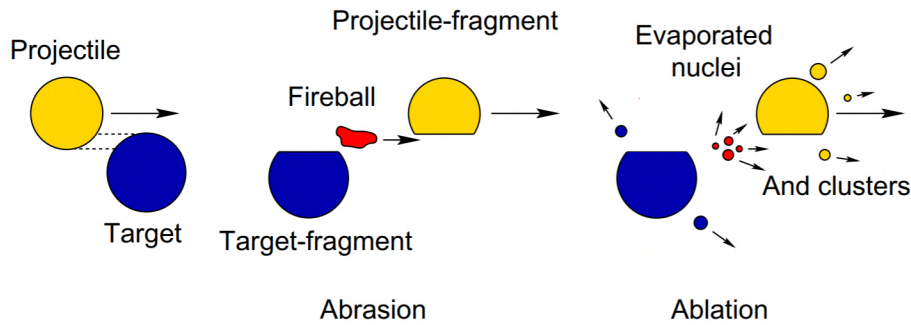


Figura 1.5: A simplified model of the nuclear fragmentation due to peripheral collisions of projectile and target nucleus [13].

The secondary fragments (nucleons or ions) are emitted with velocities slightly lower than the primary particle and they are distributed within a cone of small angular aperture with respect to the direction of the incident particle. Considering the same kinetic energy, a fragment with a lower charge has a lower energy loss (according to eq. 1.1), thus it can travel a longer distance than the primaries before stopping completely. Moreover, because of the angular distribution of the emission, fragmentation also contributes to the lateral spread of the radiation. The importance of these effects increases as a function of the penetration depth and the beam energy. In other words, the reason for our interest in knowing fragmentation is that, as we will discuss later, fragments produced by the projectile³ can reach greater depths than the primary particles and thus release energy and damage the tissues beyond the Bragg peak.

The main goals of FOOT are the study of two processes: the fragmentation of the target (proton on nucleus) and the projectile fragmentation (ion on proton), since the

³in the laboratory frame, the projectile fragments retain much of the kinetic energy of the primary particle and they are emitted strongly forward, while fragments produced by the resting target are emitted with low kinetic energy.

human body can be seen as a target mainly made of hydrogen, oxygen and carbon. The reason why only nuclear processes are studied for clinical purpose, is that hadrontherapy uses beams with energies that are not high enough to produce sub-nuclear interactions (no quarks are involved). One of the problems in the fragments detection is that in peripheral collision the momentum and energy transferred are very small, because the overlap zone is small and only few nucleons interact during the collisions. So, in the case of target fragmentation is very difficult to detect the secondary products, due to their low energy they fail to escape from the target. The solution is to approach this problem with the inverse kinematic, but this part is going to be treated deeper in the next chapter.

1.2 Radiobiological considerations

1.2.1 Dosimetric quantities

Since all physical and chemical effects, and thus biological effects, induced by radiation are a consequence of the energy transfer from the particle to a portion of tissue, we consider the quantities that takes into account the amount of energy received by tissues. The *absorbed dose* (D) is defined as the energy absorbed by a mass unit of the medium.

$$D = \frac{dE}{dm} \quad (1.7)$$

In the International System of Units (SI), the absorbed dose is measured in gray (Gy), corresponding to 1 J/1 kg.

Anyway, different types of radiation exist, so we should introduce the *equivalent dose* (H) as the product of the absorbed dose and a radiation weighting factor w_R taking into account the dangerousness of the radiation. Considering that more than one type of radiation could cross the tissue at the same time, the total equivalent dose will be the sum over the considered radiation types of the aforementioned products:

$$H = \sum_R w_R \cdot D_R \quad (1.8)$$

Radiation type	Radiation weighting Factor (w_r)
X-rays, γ -rays	1
Electrons, positrons	1
Neutrons	continuous function of neutron energy
Protons	2
Alpha particles, fission fragments, heavy ions	20

Tabella 1.1: weighting factor of different type of radiation; the weighting factor for neutrons can range from ~ 3 up to 20 and it is given by a continuous function of the neutron energy, as discussed in [14].

where D_R is the absorbed dose related to the R -th type of radiation. Table 1.1 shows the weighting factor w_r concerning different type of radiation.

If we want to take into account the different radiosensitivity of the various organs and tissues in the human body, we must introduce another weighting factor, w_T , and define the *effective dose* as the sum, over all irradiated tissues T , of the products of the equivalent dose (H_T , related to the T -th tissue) and the tissue weighting factor:

$$E = \sum_T w_T \cdot H_T \quad (1.9)$$

Both equivalent and effective dose are dimensionally the same as absorbed dose, but, in the SI, the unit of measure is the sievert ($1 \text{ Sv} = 1 \text{ J}/1 \text{ kg}$). The sievert is often used in medical physics because it can give a uniform scale to measure radiation damage regardless of the type of radiation that caused it.

1.2.2 Biological effects of radiation

Hadrontherapy and other therapies using radiation, exploit the damage that radiation causes to biological tissues in order to kill cancer cells. A cell is considered dead when its DNA has suffered such irrecoverable damage as to prevent its normal reproduction process. The genetic damage can be caused by the direct absorption of energy by DNA

(*direct damage*) or by the indirect action of free radicals coming from water radiolysis (*indirect damage*) [15].

Free radicals are atoms or molecules with an unpaired electron on the last orbital that makes them very reactive. Considering the high concentration of water in the human body, we will discuss free radicals produced by the radiolysis of water. Supposing to have an electromagnetic radiation of energy $h\nu$ ionizing a water molecule, the occurring reaction is the following:



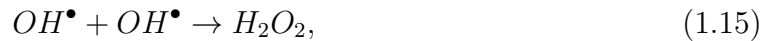
So we have the formation of the positive ion H_2O^+ and the negative ion H_2O^- , which dissociate in the following way:



Thus, we have two ions (H^+ and OH^-) and two free radicals (labelled by the \bullet symbol) as final products, which may take part in other reactions. H^+ and OH^- simply recombine into H_2O , while possible recombination for free radicals may be the harmless reaction



that, again, produces water, or the reaction



that produce hydrogen peroxide, which is dangerous for the cell [16]. Thanks to enzymes and antioxidants the effects of free radicals are under control, but exogenous sources, such as particle irradiation, can increase the free radical production rate and destabilize the balancing imposed by the defense mechanisms of the cell, thus creating an oxidative damage that leads to cellular apoptosis.

We talk about direct damage when the radiation ionizes the DNA of the cell in such a way as to cause breakages in its constituent molecules. This category of damage usually splits into *Single Strand Break* (SSB) and *Double Strand Break* (DSB). A SSB occurs when the radiation breaks one of the DNA helices, leaving the other one intact. SSB is relatively easy to repair: enzymes can recover the information from the undamaged strand and make a complementary DNA segment in order to replace the damaged one. On the other hand, when a DSB occurs, both helices are broken in the same location (or in places separated by only a few base pairs), so this damage is much more difficult to repair and it is the main cause of cell death or mutations that lead to the development of neoplasms. We could also have *clustered lesions* when two or more lesions occur within a few tens of DNA base pairs.

1.2.3 LET and RBE

Another important dosimetric quantity is the *Linear Energy Transfer* (LET), which is strictly related to the stopping power and it is frequently used in radiodosimetry and radiobiology. It is defined as the amount of energy released by a radiation in the traversed material per unit length and, differently from stopping power, it does not take into account radiative energy loss (i.e. the radiative stopping power or Bremsstrahlung) or delta-rays. In fact, LET is defined as follows:

$$LET_{\Delta} = \left(\frac{dE}{dx} \right)_{\Delta} \quad (1.16)$$

and it is usually measured in keV/ μm . In eq. 1.16, dE is the mean energy loss due to collisions with atomic electrons with transferred energy less than a cut-off value Δ ; therefore, the cut-off value excludes secondary electrons with energies greater than δ (the symbol Δ is usually omitted). The reason for this cut-off is to have a quantity that measures only the energy deposition close to the trajectory of the incident particle. Contrariwise, the unrestricted LET (LET_{∞}) takes into account all possible energy transfers.

The LET varies along the incident particles track because, as the particle deposits energy in tissues, it slows down and thus the rate of delivered energy increases. In medical physics, radiations are categorized according to their LET value: ions are considered to be *high LET radiations* (typical values range from tens of keV/ μm to hundreds of keV/ μm),

whereas X-rays and γ -rays are *low LET radiations* (typical values are of the order of few keV/ μm) due to their sparse ionizations.

Since cells response to irradiation is highly dependent on the radiation type, equal doses of different radiations may not produce the same biological response. This effect is quantified by the *Relative Biological Effectiveness* (RBE), which is defined as the ratio of the dose D_X of a reference radiation (typically γ -rays from ^{60}Co or X-rays) to the dose D of the radiation of interest that produces the same biological effect:

$$RBE = \frac{D_X}{D} \Big|_S \quad (1.17)$$

where S is the survival fraction (see section 1.2.5).

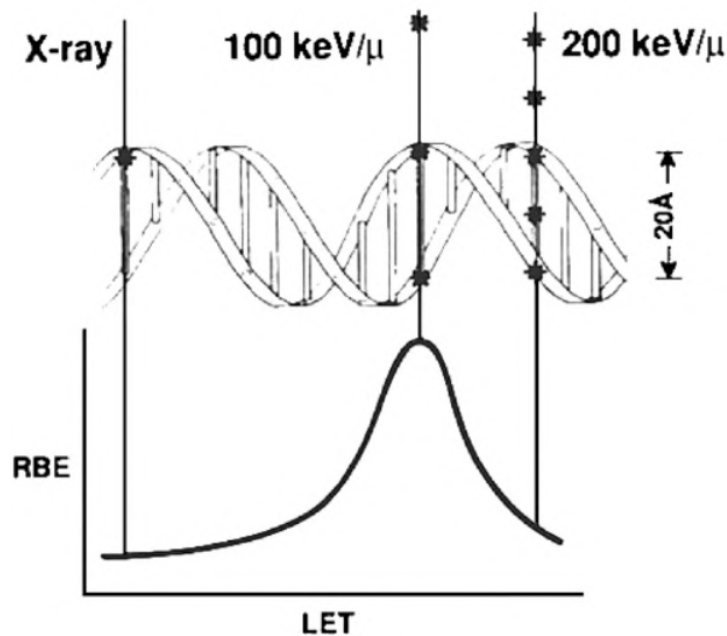


Figure 1.6: RBE as a function of LET. The diagram illustrates why radiation with a LET of 100 keV/ μm has the greatest RBE: for this LET, the average separation between ionizing events coincides with the diameter of the DNA double helix (i.e., about 2 nm). Radiation of this quality is most likely to produce a double-strand break from one track for a given absorbed dose [17].

The RBE depends on many physical and biological parameters, such as LET, dose rate, cell cycle phase, oxygen concentration, etc. Figure 1.6 shows the RBE dependence on LET. Since due to the high energy deposition density the radiation damage is severe, in case of high LET particles the RBE is high.

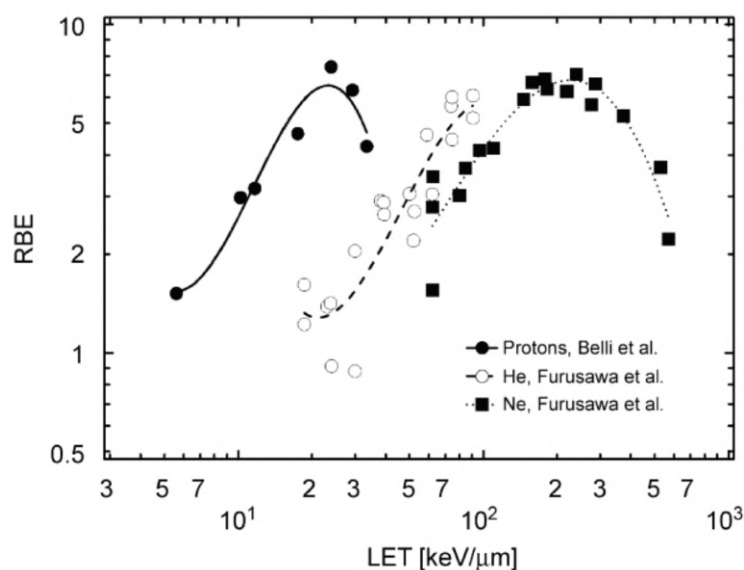


Figura 1.7: Comparison between different particles RBE curves as functions of LET [18].

In clinical practice, proton RBE is considered constant and equal to 1.1 according to ICRU recommendations [19]. Protons are therefore considered 10% more effective than photons, despite of the experimental findings. The choice to consider the proton RBE constant is due to the fact that proton LET along the track does not increase as much as for heavier ions. Other ions RBE, instead, varies significantly, e.g. up to values > 3 in case of carbon ions. In fact, the RBE increases with LET up to an ion dependent maximum value (ranging from about 100 to 200 keV/ μm), reached when the distance between two subsequent interactions is comparable to the transversal dimension of DNA (~ 2 nm), which means increasing DSB occurrences, and drops as LET increases further. This fall is due to the overkilling effect: the energy deposited in a cell by a single particle is higher than the amount required to kill the cell. Thus, the further dose deposited by ions with an even higher LET is “wasted” and the RBE falls. For heavier particles, the maximum is typically shifted to a higher LET (fig. 1.7). In fact, at

the LET corresponding to the protons RBE maximum, heavier ions have broader tracks with reduced ionization density. Therefore, light particles are generally more effective than heavy particles with the same LET.

The RBE is one of the most important quantities in heavy ion treatment planning, since it determines the photon equivalent dose, usually named *biological dose*, obtained by multiplying the absorbed dose by RBE. The biological dose quantifies the dose of conventional radiation that would produce the same biological effect as the radiation of interest. In the past, the most used biological dose units were the Gray-Equivalent (GyE) or Gy(RBE), which is obtained by weighing the physical dose with the RBE measured in the Bragg peak.

1.2.4 Oxygen Enhancement Ratio

When a tumour grows in volume, the phenomenon of angiogenesis takes place: new blood vessels are created in order to supply oxygen to the cells in the tumour center, which are too far from the original vessels to be sufficiently oxygenated. However, often these new vessels are not generated quickly enough or they might also be defective, therefore hypoxic regions are frequent, especially in the core of large tumours.

Anyway, it has been proved that hypoxic cells are more radioresistant, because of the so called *oxygen effect*. This effect is quantified by the *Oxygen Enhancement Ratio* (OER),

$$OER = \frac{D_{\text{hypoxis}}}{D} \Big|_S \quad (1.18)$$

where D_{hypoxic} and D are the doses resulting in the same biological or clinical effect with hypoxic and normoxic cells respectively. S is the survival fraction described in section 1.2.5. Typically, the OER is about 3 for photons, whereas it is greatly reduced to about 1 in the case of higher LET particles [20]. This means that high LET radiation is particularly suited to treat radioresistant tumors, since they are more effective than photons at the same dose level. Figure 1.8 shows the OER value as a function of the radiation LET.

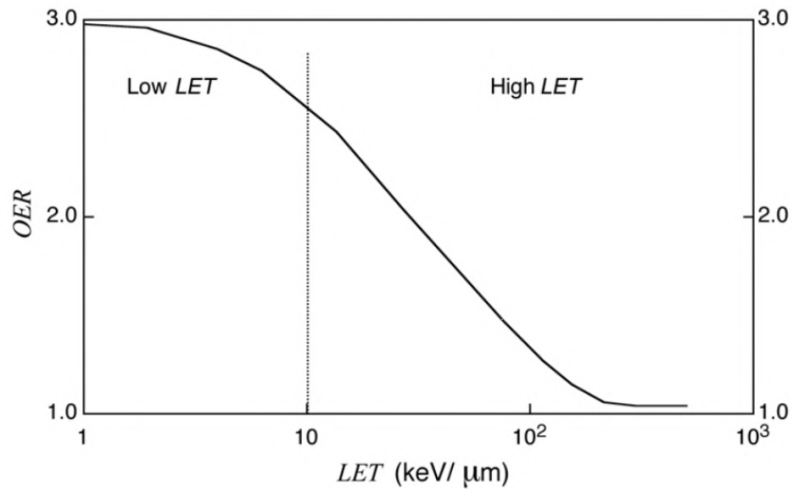


Figura 1.8: *Oxygen enhancement ratio* (OER) as a function of *Linear Energy Transfer* (LET). The vertical line ($LET = 10 \text{ keV}/\mu\text{m}$) separates low-LET values from high-LET values [21].

The oxygen effect is probably related to indirect damage, in fact the presence of oxygen molecules leads to greater formation of free radicals and, consequently, to an increase in the hydrogen peroxide concentration. For this reason, in a low LET regime, hypoxic irradiated cells are less sensitive than normoxic cells. Speaking about high LET irradiation, the influence of oxygen concentration is not so much important, since the amount of hydrogen peroxide resulting from water radiolysis is generally large by itself. This happens because, as shown in figure 1.9, the ionizations along an high LET radiation track are closer than ionizations resulting from a low LET radiation, so the recombination reactions that generate hydrogen peroxide are favored.

1.2.5 Cell survival curve

Remembering the radiation damage discussed in section 1.2.2, the probability of inducing a certain type of damage, is mostly related to particle LET. In fact, the induced damage severity can be explained in terms of the different energy deposition distributions of X-rays and ions. X-rays mostly deposit energy into the cell by photoelectric effect or by Compton effect. Since the cross sections for these processes, considering the typical

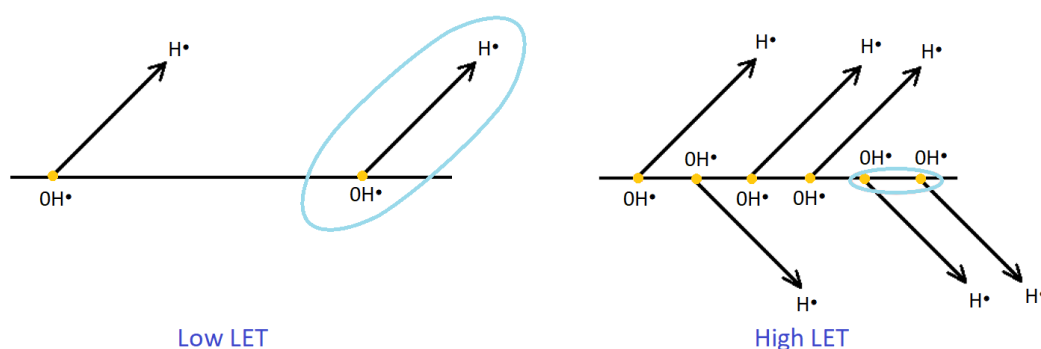


Figura 1.9: ionization and free radicals formation induced by high-LET and low-LET radiations. In a high-LET regime, subsequent ionizations are separated by a distance of about 10^2 - 10^3 pm, while the formation of the H^\bullet radical occurs about 15 nm away from the primary ionization process; in this case, the $OH^\bullet + OH^\bullet$ recombination (that produce hydrogen peroxide) is favoured. In a low-LET regime, ionizations occur every tens of nm, thus OH^\bullet and H^\bullet couples are closer than two OH^\bullet radicals, then their recombination (that produce H_2O) is favoured.

energy of photons used in radiotherapy and the typical target nuclei, are quite small (see section 1.3.4, the number of ionizations per incident photon within a cell volume is also small. Thus, many photons are required in order to deposit a significant dose and the ionization density can be assumed to be homogeneous over the entire cell volume. The spatial distribution of energy is completely different for heavy ions: charged particles have higher LET because of their higher energy deposition along their track (fig. 1.10), which results in a greater probability of causing DNA damages.

For low LET radiations the contribution of indirect DNA damages (about 65%) is larger than the direct ones (about 30%), and only $\sim 30\%$ of DSB are clustered, while for high LET ions, the contribution of direct hits is higher and the clustered damages rise to about 70% [23, 24].

The different behaviour in response to photons and heavy ions can be represented by the *cell survival curve* (fig. 1.11): cell proliferation is analyzed after irradiation and the percentage of surviving colonies is plotted as a function of the delivered dose. The surviving fraction is the ratio between the number of surviving cells and the number of

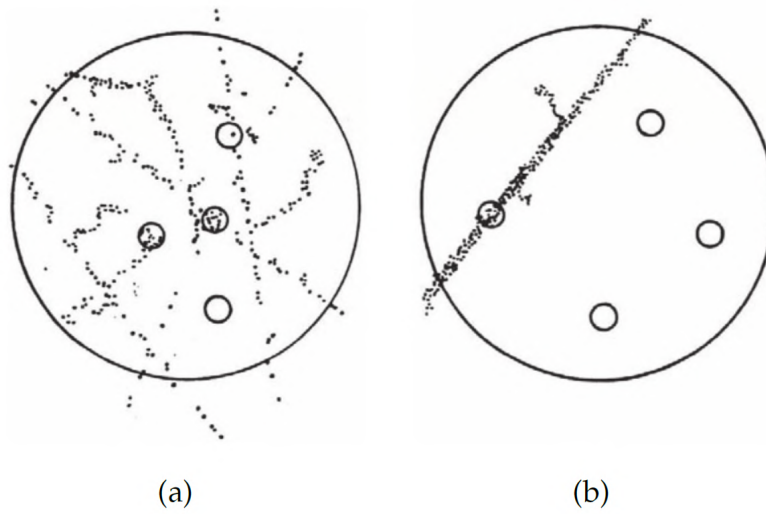


Figure 1.10: Ionization density in a medium irradiated by X-rays (a) and high LET particles (b). The small circles represent biological targets and the dots represent ionizations produced along the tracks [22]

the seeded ones, and it is conventionally plotted versus the dose on a log-linear scale. The shape of the cell survival curve depends on the type of radiation. For low-LET radiation, the curve is characterized by a shoulder region over the low dose range, while for higher doses it tends to be linear. This behavior is well described by the linear-quadratic model:

$$S(D) = e^{-\alpha D - \beta D^2} \quad (1.19)$$

where S is the surviving fraction, D is the absorbed dose and α and β are experimentally determined parameters that measure respectively the lethal and sublethal damage suffered by the cell. Specifically, the βD^2 component takes into account the natural ability of the cell to recover from lethal damage.

The shoulder of the survival curve is determined by the $\frac{\alpha}{\beta}$ ratio, that corresponds to the dose value at which the linear component (αD) and the quadratic component (βD^2) are equal. The $\frac{\alpha}{\beta}$ ratio related to photon irradiation is used to characterize the cell type in terms of radiosensitivity: the so called *late responder* tissues, whose cells are

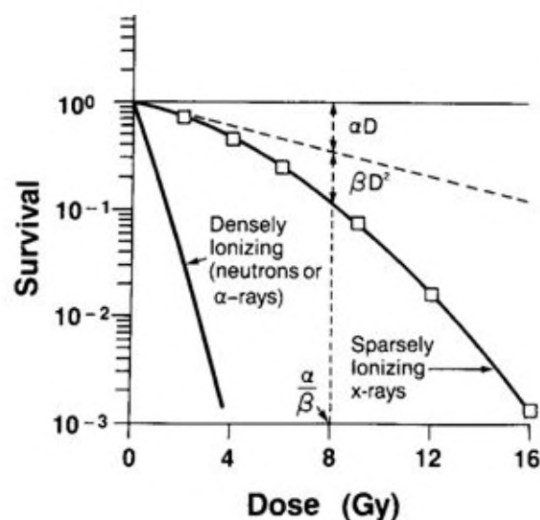


Figure 1.11: Cell survival as a function of dose for densely and sparsely ionizing radiation. The fraction of cells surviving is plotted on a logarithmic scale against dose on a linear scale [25].

characterized by low replicative activity (i.e. spinal cord, cartilage, bone, lung), tend to have a high quadratic component and therefore a low $\frac{\alpha}{\beta}$ ratio (typically between 0.5 and 6 Gy); whereas a high ratio (typically between 7 and 20 Gy) is associated to early responder tissues, characterized by high replicative activity (i.e. skin, bone marrow, intestinal epithelium, tumor tissue). Radiosensitivity depends on the cell type and it is also influenced by the cell cycle phase [26].

As already mentioned in section 1.2.3, we can see in figure 1.12 how to extrapolate the RBE value with respect to a reference radiation. Given a fixed surviving fraction value, RBE is the ratio between the doses obtained from the two curves (the curve of the reference radiation and the curve of the radiation whose RBE we want to know). It is important to note that the RBE of a radiation is not always the same, but decreases with increasing dose.

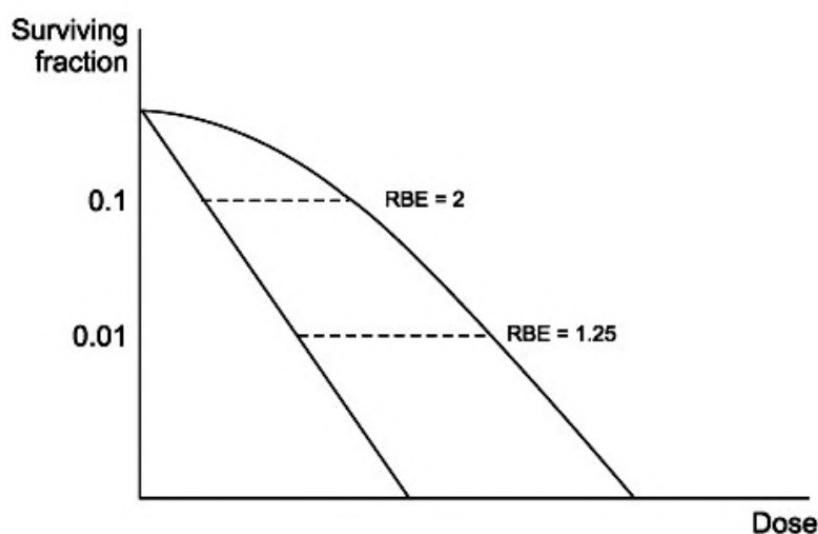


Figura 1.12: Representation of the RBE as the ratio between dose values from different radiation given a fixed surviving fraction value. According to linear quadratic model, RBE is maximal when dose $\rightarrow 0$. If the fractional dose increases, the RBE converges to a minimal value [27].

1.3 Treatments with heavy charged particle

1.3.1 History of hadrontherapy

Over a hundred years ago, in 1895, *William Conrad Röntgen* discovered X-rays: a mysterious radiation that today we know to be photons of energy around 10^4 eV. Observing the absorption of X-rays, Röntgen found their extraordinary properties, as the different absorption coefficient by different tissues. This led to the first radiography.

One year later, in 1896, *Henry Becquerel* discovered the natural radioactivity and, even if the radiobiological effects were not known at that time, the idea to cure cancer with this radiations has been achieved.

In 1931, thanks to *Ernest Lawrence* and *Stan Livingston* who realized the first cyclotron at the University of California (Berkeley), the first application of accelerators in medicine began. Ernest and his brother John (a doctor considered the founder of nuclear medicine) started to irradiate patients with salivary gland tumor using neutron beams.

In 1946, the American physicist *Robert Wilson* was called to lead the team for the design and the construction of a new 160 MeV cyclotron in Harvard. He spent one year in Berkeley, collaborating with Ernest Lawrence, to complete the design of the accelerator. It was then that Lawrence asked him to define the shielding of the new cyclotron, by calculating the interactions with matter of a 100 MeV proton beam. Wilson followed this suggestion and found that protons had completely different trend with depth compared to X-rays.

Protons remove electrons from molecules, ionizing them while slowing down, and the maximum number of ionizations per millimeter occurs just before they stop. This maximum was called Bragg Peak, from the British physicist *William Bragg*, who was the first to observe it in alpha particles. These new knowledge allowed Wilson to propose the use of protons for irradiating solid tumors, as a better therapy than the one based on X-rays. His pioneering and now famous paper, *Radiological Use of Fast Protons*, was published in 1946 in the journal *Radiology* [28].

Two years after Wilson's paper, researchers at the Berkeley Laboratory conducted extensive studies on proton beams and confirmed his predictions. After many animal irradiations, the first patient was treated in 1954 under the guidance of Cornelius Tobias, a Hungarian physicist, who, together with Lawrence, performed the first hadron treatment on humans. The first irradiations were not directly on the tumor but on the pituitary gland, which is responsible for making hormones that stimulate cancer cells to grow. Patients with metastatic breast cancers were treated surgically to remove most of the tumor mass and then irradiated with protons on the pituitary gland to reduce the production of grow hormones and hence the chances of metastatic proliferation. The pituitary gland was a natural site for the first treatments, because the gland location was easily identified with standard X-ray films. Between 1954 and 1974 about 1,000 hypophysis and pituitary tumors were treated with protons with a 50 % success rate.

This technique was called 'hadrontherapy' in 1992 and this term was later used to include all types of non-conventional radiation beams used at the time: protons, helium ions, neon ions, neutrons and pions. Indeed, physicists call 'hadrons'⁴ all the particles that feel the strong interaction since they are made of quarks and antiquarks.

⁴From the greek *adrós* that means 'strong'.

Hadrontherapy is nowadays not widely used compared with the radiotherapy due to some practical difficulties, such as costs and the large size of the machines. In case of radiotherapy, photons are produced by accelerated electrons up to 10 MeV, while protons need to be accelerated to reach higher kinetic energies (up to 200 MeV) in order to have a suitable range in body to reach deep seated tumors. For this reason cyclotrons and synchrotrons are used in hadrontherapy, and they are much more expensive than linear accelerators (LINAC) which are employed in radiotherapy. Hadrontherapy is not a substitution of radiotherapy, but it is more suitable in some situations, for example, to treat tumors that are radioresistant or localized near sensitive organs.

The kind of tumors that are mostly treated with hadrontherapy are *chordoma* and *chondrosarcoma*, which are located in critical areas like the base of the cranium or spine, and *uveal melanoma*, for which the proton therapy produces the same chance of survival than the enucleation⁵. In the first two cases, after a certain time, about 80 % of patients are free from tumor recurrences, instead of the 40 % for patients treated with X-rays. For the uveal melanoma, this percentage grows up to 95 % and more than 80 % of patients also retained the sight capability after the treatment. This and more results brought lots of oncologists to approve the superiority of the proton therapy, especially for children, since it has a lower risk of inducing carcinogenesis.

The evolution of hadrontherapy was not a process that developed only in the USA, but in the '80s a lot of hadrontherapy centers were built also in Japan. Recently also Italy has opened 3 national centers: CATANA, in Catania, where only eye tumors are treated; CNAO, in Pavia, where since 2011 they are using both protons and carbon ions for treatments; the Proton Therapy Center, in Trento, that started to cure patients in 2014.

1.3.2 Proton therapy

Considering all the previously acquired information about Bragg curve and dosimetric quantities, we can now discuss the absorbed dose as a function of depth for a therapeutic

⁵*uveal melanoma* is a cancer (melanoma) of the eye involving the iris, ciliary body, or choroid (collectively referred to as the 'uvea'). *Enucleation* is a type of ocular surgery consisting in the removal of the eyeball, but with the eyelids and adjacent structures of the eye socket remaining.

proton beam. In figure 1.13 a proton Bragg curve is shown, along with labels identifying several regions. This particular type of plot is called *pristine Bragg curve*, which indicates that it is obtained by means of a monoenergetic proton beam sent on the absorbing material, that is, in this case, water ⁶.

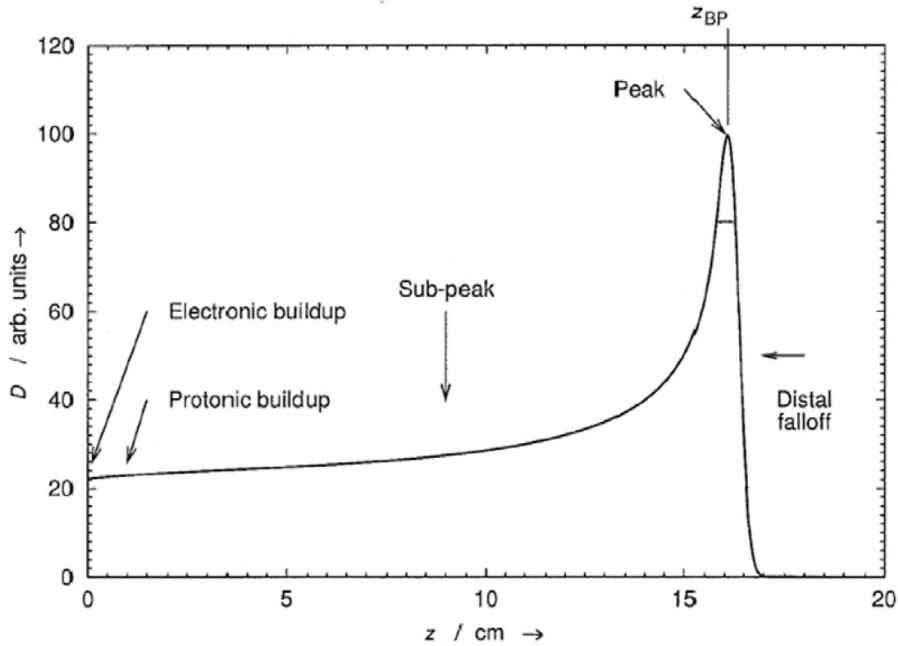


Figura 1.13: Absorbed dose D as a function of depth z in water from an unmodulated (pristine) proton Bragg peak produced by a broad proton beam with an initial energy of 154 MeV. The various regions that are labeled are defined in the text. Note that the electronic buildup region, which spans only a few millimeters, is not visible in this plot. This type of dose distribution is clinically useful because of the relatively low doses delivered to normal tissues in the sub-peak and distal-falloff regions with respect to the target dose delivered by the peak [29].

Here, we use a Cartesian coordinate system with the z axis parallel to and centered on the proton beam central axis. The x and y axis are mutually orthogonal and perpendicular to the z axis. The coordinate system origin is located at the front face of the

⁶Often beams are tested on phantoms made of water, because they are good in simulating the density of the human body.

absorber, e.g. the extended medium in which we consider the absorbed dose distribution. Here below, we will describe in more detail the regions of the pristine curve (fig. 1.13), in order of increasing depth.

First of all, we can find the *electronic buildup region*: a small region near the surface of the absorber where the proton beam is incident. High-energy proton beam liberates δ -rays with sufficient kinetic energy to travel several millimeters in tissue. Under certain circumstances, this region exhibits an increase of dose with increasing depth, asymptotically approaching absorbed dose in the sub-peak region within the depth corresponding to the range of the most penetrating recoil electron. In some cases, electronic buildup is not observed.

Still near the surface of the absorber there is the *protonic buildup region*, where the absorbed dose increases with depth because of the buildup of secondary protons that are attributable to proton-induced non-elastic nuclear interactions (e.g. $^{16}\text{O}(p, xp)$ reactions). As the electronic buildup, the protonic buildup may not be observed in some cases, particularly at low incident proton beam energies.

The *sub-peak region* is the region extending from the surface of the absorber to the depth just proximal to the peak. The physical processes involved here are, in decreasing order of importance, the stopping power's dependence on the inverse-square of the proton velocity, the removal of some protons and the liberation of secondary particles through nuclear reactions, the progressive lateral deflections due to multiple Coulomb scattering (MCS), which leads to lateral protonic disequilibrium and reduction of the proton fluence on the central axis. As we can see in figure 1.14, this lateral spread is more important for small proton beams (e.g. beams less than a few millimeters in width) and leads to a decrease of the longitudinal dose with depth along the beam axis. If we consider large proton beams, the MCS effect is negligible, since the reduction of fluence in the beam core, due to protons deflecting away from the central axis, is compensated by protons deflecting from the external layers of the beam to the internal ones.

The *pristine Bragg peak* is simply the maximum dose near the end of range, and is located at z_{BP} . The physical processes governing the location and/or height of the peak are mainly the proton stopping power and energy straggling, nuclear reactions to a much lesser extent and, for very small fields, MCS.

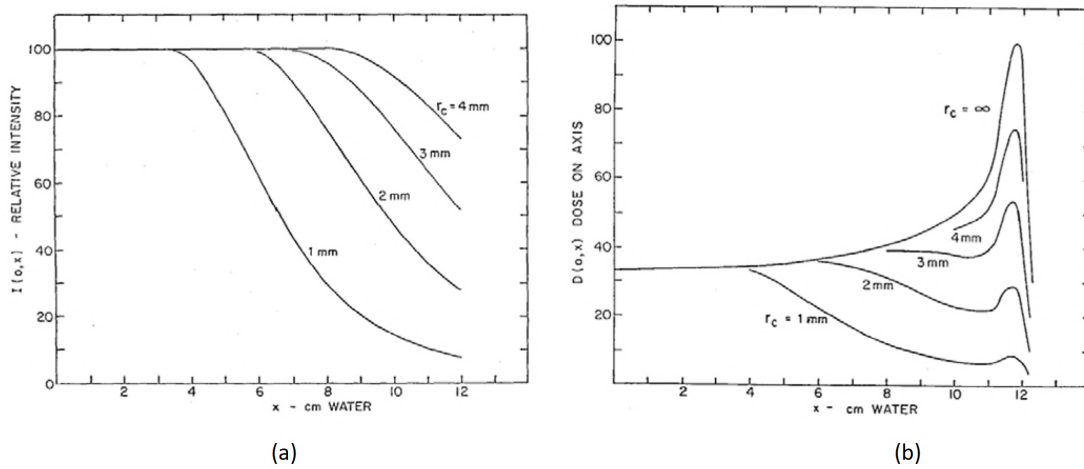


Figure 1.14: (a) Proton fluence $I(0, x)$ along the beam central axis as a function of the depth x in water. Curves are shown for beams with circular cross sections with radius between 1 and 4 mm. Some protons are lost because of scattering events that deflect them from the central axis. This is increasingly observed for small beams and at large depths. (b) The corresponding central-axis absorbed-dose curves. Note how the fluence depletion reduces the absorbed dose at the peak with respect to the entrance dose [30].

At the end we have the *distal falloff region*, which extends from depths greater than the pristine Bragg peak depth, z_{BP} . The width of this region is not restricted, however, in many practical situations, the distal falloff region can be truncated at a depth where the dose falls below a threshold value, e.g. 1 % of the dose at the Bragg peak, $D(z_{BP})$.

The idea behind hadrontherapy is to cure cancer using a particular beam, with a specific energy, in such a way that the dose peak occurs at the depth of the tumor. Anyway, tumors are spatially extended objects, so there is need of techniques to deliver dose over a certain depth range.

The most common technique is to enlarge the Bragg peak by means of a superposition of beams with different energy. In this way, we obtain the *spread out Bragg peak* (SOBP), shown in figure 1.15. The regions of a SOBP curve are, in many ways, similar to those of a pristine Bragg curve, as seen in figure 1.16. However, there are several unique difficulties in characterizing SOBPs because of their sometimes unusual shape. For example, SOBPs

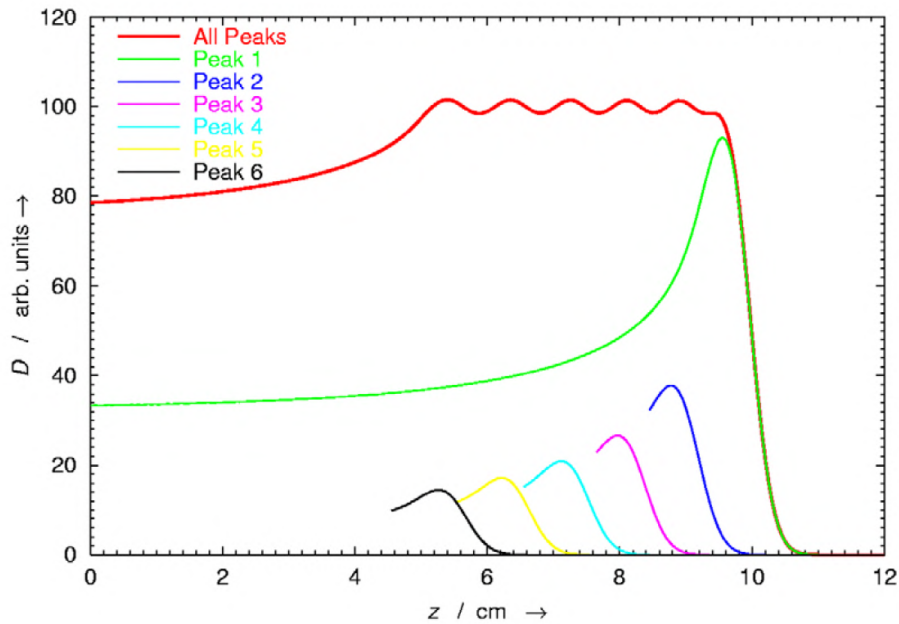


Figure 1.15: Absorbed dose D as a function of depth z in water from a spread-out Bragg peak (SOBP) (uppermost curve) and its constituent pristine Bragg peaks (lower curves; for clarity, all but the deepest pristine Bragg peak are only partly drawn). In many cases, the clinical target volume is larger than the width of a pristine Bragg peak. By appropriately modulating the proton range and fluence of pristine peaks, the extent of the high-dose region can be widened to cover the target volume with a uniform dose [29].

with two or more discrete pristine Bragg curves may have multiple dose maxima in the modulated-peak region (e.g. the ripple shown in figure 1.15). Moreover, instead of Bragg peak, the curve is characterized by the *Modulated-peak region*, extending from z_a to z_b . In general, the values of z_a and z_b are most reliably determined using iterative numerical fitting methods. Conceptually, they are closely related to the proton ranges of the most and least penetrating pristine peaks in the SOBP.

As already mentioned in section 1.1.3, protons may interact with the atomic nucleus via non-elastic nuclear reactions in which the nucleus is irreversibly transformed. To enter the nucleus, protons need to have sufficient energy to overcome the Coulomb barrier, which depends on the atomic number of the nucleus. The total non-elastic cross-section for proton-induced nuclear reactions has a threshold, on the order of 8 MeV in the atomic

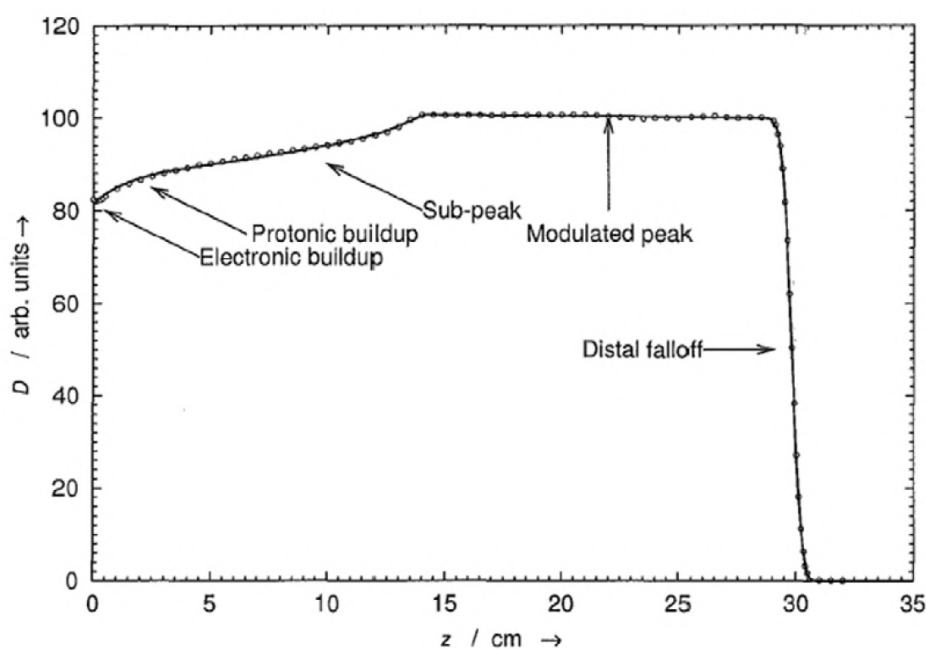


Figura 1.16: Absorbed dose D as a function of depth z in water from a spread-out proton Bragg peak (SOBP). Various locations and regions that are indicated on the plot are defined in the text. Note that the electronic buildup region, which spans only a few millimeters, is not visible in this plot [29].

nuclei of biologically relevant elements, rises rapidly to a maximum at around 20 MeV, then asymptotically declines to about half the maximum value by about 100 MeV. In figure 1.17 this trend is shown for an oxygen target; in this case the energy threshold is 6 MeV.

The main effect of nuclear reactions within a therapeutic region of a proton field is a small decrease in absorbed dose due to the removal of primary protons, which is compensated to a large extent by the liberation of secondary protons and other ions. Secondary protons represent about 10% of the total absorbed dose and they are also responsible for a small, but not negligible, alteration in the spatial dose distribution. Other ions (e.g. d, t, ^3He , ^4He , etc.) are generated in smaller proportions, they represent about or less than 1% of the therapeutic dose, their energy and range are very small and they deposit their kinetic energy locally, i.e. very near their point of creation [32].

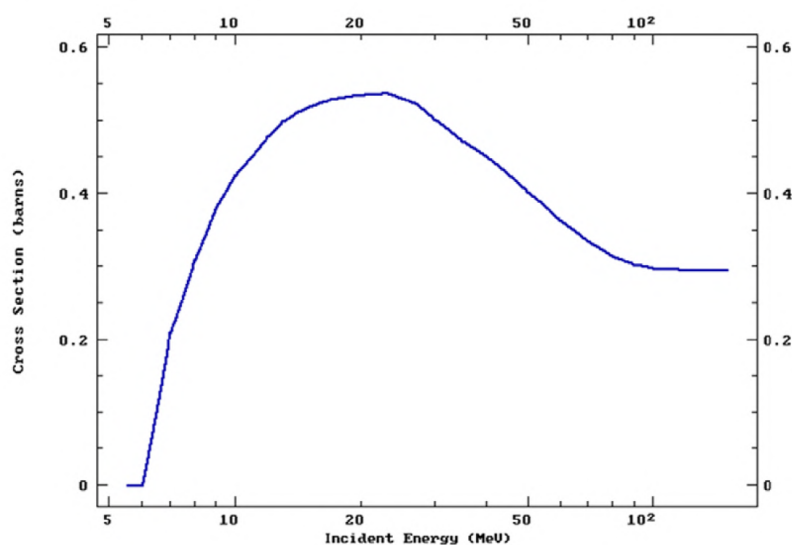


Figura 1.17: The total proton-induced non-elastic nuclear reaction cross section in oxygen versus proton energy, showing a threshold corresponding to the Coulomb barrier at approximately 6 MeV [31].

In nuclear interaction also neutrons are produced in copious quantities. Neutrons span 10 orders of magnitude in energy, their energy distributions depend strongly on the proton beam energy and direction, they are extremely penetrating and their relative biologic effectiveness is as much as about 20 times higher than that of proton radiation [33]. Neutrons can be produced in patient tissues, but also in the equipment which constitute the beam delivery system, generating a diffuse radiation that may irradiate the whole patient body. For all these reasons, neutrons potentially increase the risk of radiogenic late effects [34, 35].

Nuclear reactions inside the patient may provide a non-invasive approach to measure a variety of beam and patient properties, such as proton beam range, elemental composition of tissues, and even intra- or inter-fraction physiology. The basic approach is to detect gamma rays from proton-induced nuclear reactions, such as neutron capture reactions, denoted by (n, γ) . Gamma ray detection approaches have included positron emission tomography camera [36], Compton camera [37], 1D detector arrays [38], and photon counting systems [39]. These techniques are in various stages of research and

development.

1.3.3 Ion therapy

The characteristic Bragg curve of an ion beam has basically the same structure as the one described above. Anyway, ions present some peculiar differences from protons.

To begin with, ions undergo less energy loss fluctuation than protons (these fluctuations are described by the Vavilov distribution [40]), that leads to a lower range straggling. The ratio of the straggling width σ_R and mean range R is nearly constant and can be described by

$$\frac{\sigma_R}{R} = \frac{1}{\sqrt{M}} f\left(\frac{E}{Mc^2}\right) \quad (1.20)$$

where f is a slowly varying function depending on the absorber [41], while E and M are the energy and the mass of the particle. For light ions stopped in water the relative straggling σ_R/R is of the order of 10^{-3} and, because of the $1/\sqrt{M}$ dependence, it is smaller for heavier ions. Ions also have an higher RBE due to their higher charge that increase their LET. This means that, for the same range, ions have an higher and sharper Bragg peak than protons.

Furthermore, the heavier an ion is the less it penetrates and, thus, it needs more energy per nucleon to reach the same depth. In cancer therapies, the deepest point in the human body is about 30 cm from the body surface; in order to reach this depth, a specific beam energy is needed, depending on the type of ion beam we are using. To give some examples, this energy has to be about 220 MeV/u for ^4He (same energy as proton beams), 430 MeV/u for ^{12}C and 600 MeV/u for ^{20}Ne .

Due to their greater mass, ions are hardly deviated by Coulomb interactions with nuclei, which means that the lateral spread is smaller than a proton beam. This is a particular advantage in clinical practice, especially for treatments near organs at risk, since allows better control on the spatial dose distribution. An analytical solution of the statistical distribution function for the resulting scattering angle θ is given by Molière [42]. For small angles the higher-order terms in Molière's solution can be neglected and the angular distribution can be approximated by a Gaussian function with a standard

deviation (σ_θ) given by Highland [43, 44].

$$\sigma_\theta = \frac{14.1 \text{ MeV}}{\beta pc} Z_p \sqrt{\frac{d}{L_{\text{rad}}}} \left[1 + \frac{1}{9} \log_{10} \left(\frac{d}{L_{\text{rad}}} \right) \right] \quad (1.21)$$

where σ_θ is expressed in rad, β , p and Z_p are, respectively, the velocity, momentum and charge number of the projectile ion. The absorber material is characterized by the thickness d and the radiation length L_{rad} (values of L_{rad} for common materials can be found in [44]). The angular spread for heavy charged particles is small (of the order of 1 mrad for a thin target), but increases significantly towards low energies due to the βpc term in the denominator of eq. 1.21. Comparing beams with the same range in water (e.g., 150 MeV protons and 285 MeV/u ^{12}C ions with $R = 15.6$ cm) shows that the angular spread for protons is more than three times larger than that for ^{12}C ions.

While the stopping process of high-energy ions penetrating a thick absorber is governed by collisions with atomic electrons, the probability of nuclear reactions is much smaller, but leads to significant effects at large penetration depths. At energies of several hundred MeV/u violent nuclear spallation reactions may result in a complete disintegration of both projectile and target nuclei or in partial fragmentations (see section 1.1.3). Fragmentation reactions have been extensively studied in nuclear physics [45, 46] and experimental data are available for many projectile-target combinations and for a wide range of beam energies [47].

Some important conclusions can be drawn for the effects of fragmentation relevant to radiotherapy with high-energy ion beams:

1. nuclear reactions cause a loss of primary beam particles and a buildup of lower-Z fragments, these effects become more and more important with increasing penetration depth;
2. the secondary (or higher-order) projectile-like fragments are moving with about the same velocity as the primary ions, they have in general longer ranges and they produce a dose tail behind the Bragg peak;

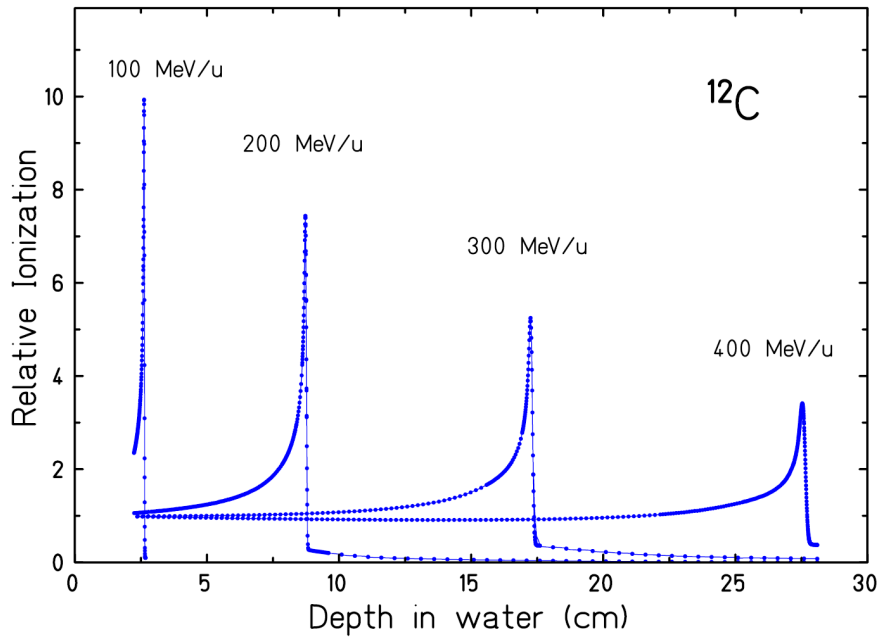


Figure 1.18: Measured Bragg curves of ^{12}C ions stopping in water [51].

3. the angular distributions of fragments are mainly determined by reaction kinematics and it is forward directed, but it is much broader than the lateral spread of the primary ions caused by MCS [48, 49].

In a comparative experimental study of the fragmentation characteristics of ^{10}B , ^{12}C , ^{14}N , ^{16}O , and ^{20}Ne , the total nuclear cross section for reactions changing the charge number Z has been found to be even smaller for ^{12}C than that of ^{10}B , while the value for ^{14}N was relatively high [50]. This indicates that shell-structure effects are still visible in high-energy reactions. Nevertheless, at larger penetration depths a substantial fraction of primary ions is lost through nuclear reactions. For example, in a 400 MeV/u ^{20}Ne beam only 38% of the primary ions reach the Bragg peak at 16 cm depth in water, while the number of surviving ^{12}C ions at the same range is 52%. Regarding fragmentation, carbon ions thus offer relatively good conditions. Furthermore, the positron-emitting fragments ^{10}C and ^{11}C can be utilized for in vivo range monitoring with positron emission tomography (PET) techniques.

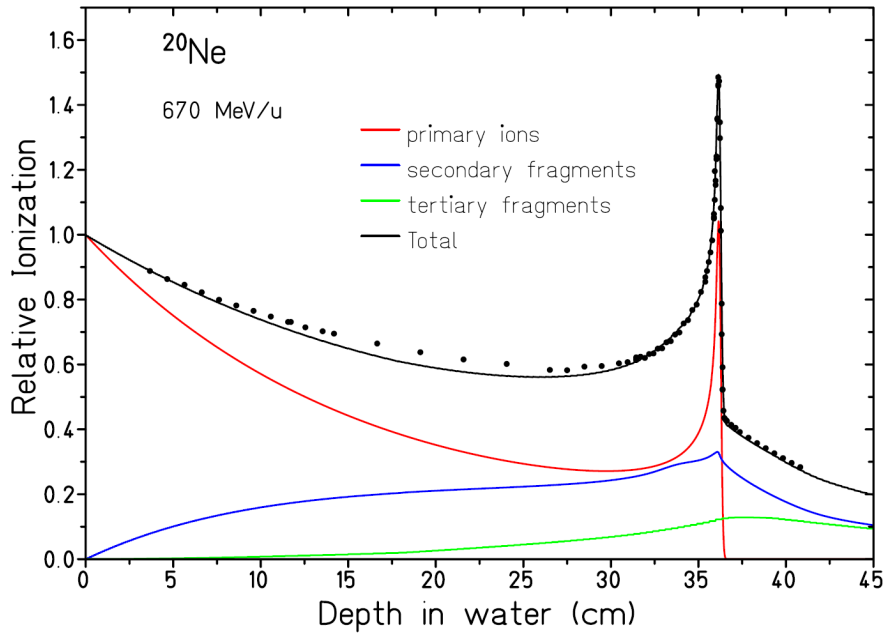


Figure 1.19: Bragg curve for 670 MeV/u ^{20}Ne ions in water measured at GSI (circles) and calculated contributions of primary ions, secondary and tertiary fragments [52].

The impact of nuclear fragmentation on the depth-dose profile is shown in figure 1.18 for ^{12}C beams with different energy. With increasing penetration depth the peak-to-entrance dose ratio becomes gradually smaller, mainly caused by the exponentially diminishing flux of primary ions. The buildup of lower-Z fragments is clearly visible in the dose tail behind the Bragg peak at larger depths. Additionally, the Bragg peaks are increasingly broadened by straggling. In comparison to ^{12}C ions, these effects are much more pronounced in the example shown in figure 1.19 for 670 MeV/u ^{20}Ne ions with a range of about 36 cm in water. The peak-to-entrance dose ratio is only 1.5 in this case. The calculated contributions of the primary ions and second and third generation fragments are based on a semiempirical fragmentation cross-section formula [52].

Finally, we must say that, as in the case of protons, nuclear reactions produce a certain neutron component. Anyway, in heavy ion therapy, the dose contribution of secondary neutrons produced by fragmentation reactions in tissue appears to be small, even considering their enhanced biological effectiveness. The neutron dose in typical

carbon-ion treatments has been estimated to be 8 mGy per treatment Gy, i.e., less than 1% of the treatment dose. This is about ten times less than the dose contributed by charged fragment [53]. The absorbed dose due to neutrons is of course included in the measured Bragg curves, entering as basic input data into the physical model used in heavy-ion treatment planning.

1.3.4 Other particle therapies

Photons interacts with matter in a different way with respect to heavy charged particle. When a photon beam crosses a certain thickness of material, it is attenuated according to the *Lambert-Beer* law:

$$\Phi(x) = \Phi_0 e^{-\frac{x}{\lambda}} \quad (1.22)$$

where Φ is the number of photons after passing through a thickness x , Φ_0 is the initial number of photons and λ is the so called *attenuation length*, that depends on the characteristics of the absorbing medium.

$$\lambda = \frac{A}{\rho N_A \sigma} \quad (1.23)$$

where A and ρ are respectively the mass number and the density of the material, N_A is the Avogadro's number and σ is the total absorption cross section that takes into account any interaction that photons can undergo, i.e. photoelectric effect, Compton scattering and pair production (figure 1.20).

In conventional radiotherapy [56], photons beams are used and, as shown in figure 1.21 (blue line), their energy loss decrease with the depth of their path. This ensures that the dose delivered to the tumor is of the same order as that sent to tissues before and after the tumor itself. The first step in solving this issue is the IMRT (*Intensity Modulated Radiation Therapy*), i.e. the overlap of different photons beams from different directions. This allows to increase the dose in the tumor at each irradiation keeping constant the

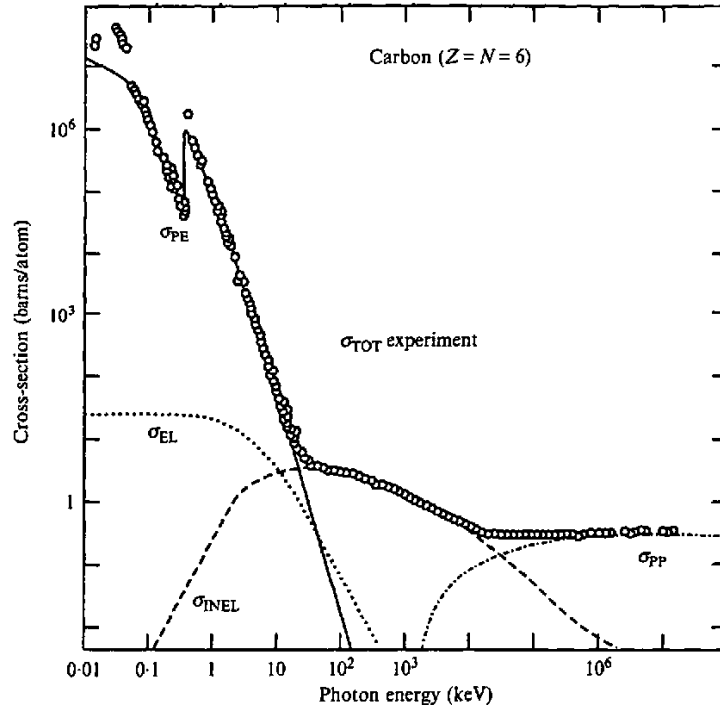


Figura 1.20: Cross-section for photon scattering from carbon showing the contributions of photoelectric, elastic (Rayleigh), inelastic (Compton) and pair-production cross sections to the total cross sections. Also shown are the experimental data (open circles). The energy of photons used in conventional radiotherapy starts from few tens of keV up to ~ 10 MeV [54].

dose in the surrounding tissues. Anyway, dose in healthy cells is still not low enough for being sure to prevent other damages.

Conventional radiotherapy often uses linear accelerators (LINAC) to accelerate electrons and produce X-rays in a controlled manner. To obtain X-rays, an electron beam collides on a target metal plate, where bremsstrahlung and ionization phenomena occur. *Electron Beam Therapy* (EBT) [57] also involves electron beams accurately pre-accelerated within LINACs. This therapy differs from radiotherapy because the beam is collimated and sent directly to the patient. Electrons have low penetrative power and for this reason they are used to treat superficial tumors (e.g. skin cancers). In general,

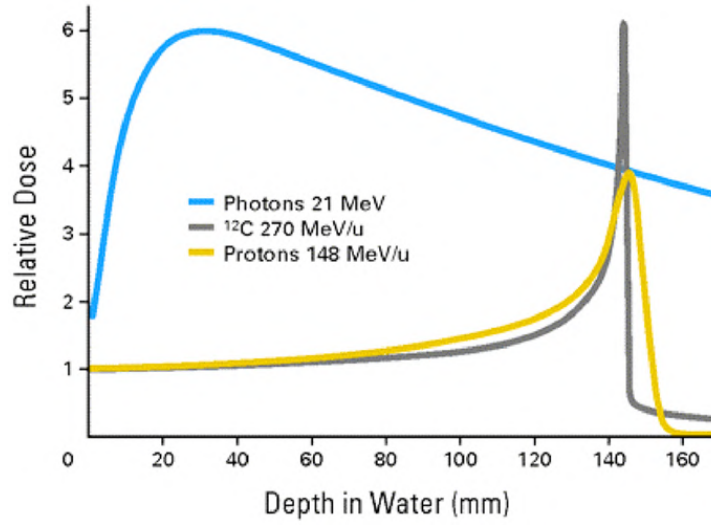


Figure 1.21: Depth-dose distributions from X-rays, proton beams, and carbon ion beams superimposed with each other for comparison [55].

both electrons and photons are characterized by low LET, which does not allow them to reach high depths effectively, and high OER, meaning that the effects of a treatment could be reduced in hypoxic tissues.

Another experimental therapy is the so called *Boron Neutron Capture Therapy* (BNCT) [58], that is based on thermal neutron irradiation (white energy $E_n \approx 0.025$ eV) of the tumor region opportunely enriched with ^{10}B . The neutron capture reaction occurring on boron nuclei leads to formation of excited ^{11}B isotopes, which decay almost instantly into two high energy LET products, an α particle and a ^7Li nucleus:



These products cause ionizations in the region around the capture, in a range of $\sim 9 \mu\text{m}$ for the α particle and $\sim 5 \mu\text{m}$ for the ^7Li nucleus, values slightly lower than the diameter of a cell ($10 \mu\text{m}$). The choice to use ^{10}B is therefore advantageous for the low range of products, which induce effective damage only inside the cell where the neutron capture take place. The difficulties related to this therapy are manifold, including the difficulty

related to the control of boron distribution in the patient body and the control and focusing of the neutron flux, that must be extracted from appropriate nuclear reactors.

Capitolo 2

The FOOT experiment

The FOOT (**F**ragmentati**O**n **O**f **T**arget) experiment has been developed for the purpose of obtaining new measurements of fragmentation cross sections, which will be used in proton and ion therapy to achieve an improvement in the Treatment Planning Systems (TPS). In fact, not all fragmentation processes have been investigated by experimental measurements, especially in the energy range useful for therapeutic application (50 – 250 MeV for protons and 50 – 400 MeV/u for carbon ions). Because of the gaps in the experimental data, the only possibility, at the moment, to describe the fragmentation process is to rely on nuclear models [59, 60], which however are not exact calculable theories and therefore suffer from many uncertainties.

The products of the target fragmentation could be one of the causes of the increase in proton RBE, which now is assumed to be constant and equal to 1.1. New fragmentation measurement will provide a better estimation of the real dose released in healthy tissues in proton therapy.

In the case of proton therapy, only target fragmentation occurs, and this leads to the production of low energy fragments, hence, having a short range. In order to study this process, the FOOT experiment exploits an inverse kinematic approach, in which heavy ion beams (such as carbon or oxygen) are sent on an hydrogen enriched target. This allows to have high-energy and long-range fragments which are able to cross all the detectors.

2.1 Motivations and aims

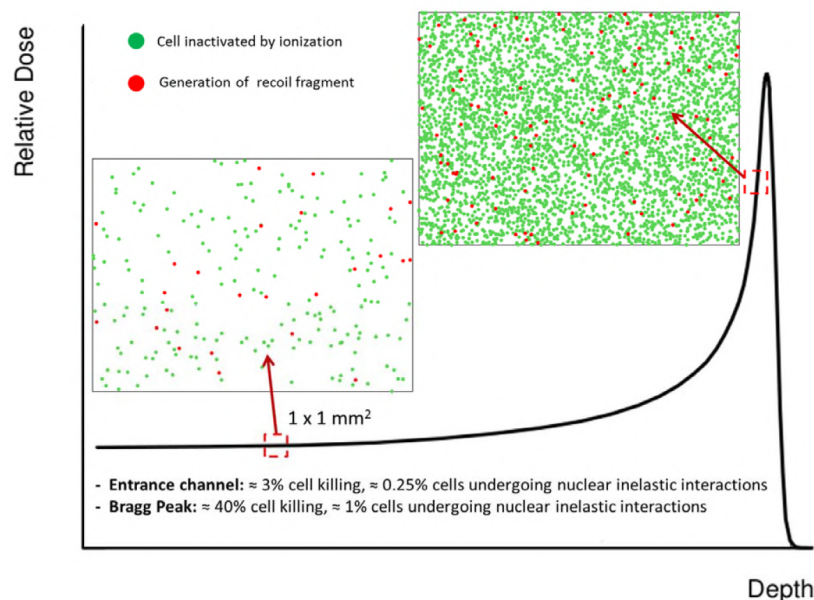


Figure 2.1: illustrative image of the expected relative impact of the target fragmentation in the entrance and in the peak regions as compared to the effect of the inactivation by ionization [61].

Target fragmentation in proton beam irradiation

The target fragmentation in proton beam is more relevant in the entrance channel, as shown in figure 2.1, where the impact of nuclear fragmentation as compared to ionization induced cell killing is less overwhelmed than in the peak region. The fragmentation of the target nuclei in case of proton as projectiles was addressed several years ago [62] and later it was abandoned because of the difficulty to measure those fragments at very low energy with a reasonable accuracy.

As can be seen in figure 2.2, the target fragment spectra are extremely peaked to very low energies, this means that the range of the particles can not be longer than few tens of microns (see tab. 2.1), making the fragments experimental detection extremely difficult, since they would not even be able to escape from the target. This problem can be overcome using the inverse kinematic approach, as discussed in section 2.3.

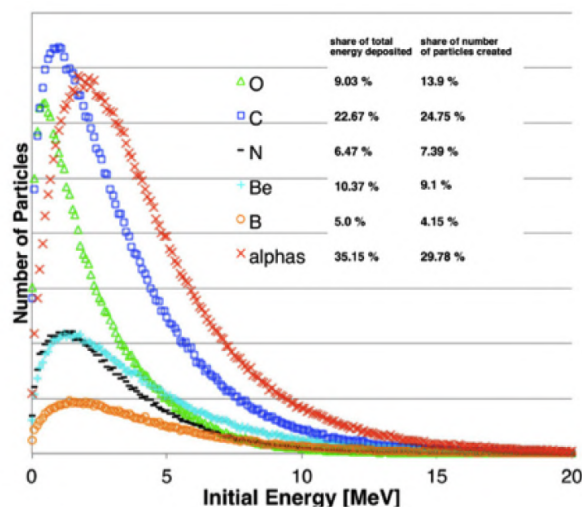


Figure 2.2: Full spectra of fragments from target media in the case of a prostate irradiation with protons of 160 MeV, integrated in the complete range of beam propagation [63].

The measurement of single differential cross sections ($d\sigma/dE$) for such reaction channels will then open for the first time the possibility to investigate the target fragmentation effects on a biological level.

Projectile fragmentation in ion beam irradiation

For what concern heavy ion therapy, FOOT aims to measure the production yield and energy of fragments generated by ^{12}C beams in the therapeutic energy range, in order to provide a wider set of experimental data to benchmark nuclear models and improve the treatments quality. Nuclear fragmentation channels will also be explored for ^{16}O and ^4He beams, in which interest is growing as promising alternatives to protons and carbon ions in particle therapy. Oxygen beams are increasingly considered as a fundamental tool against hypoxic tumours [64], while helium is regarded as an alternative to protons thanks to its lower impact on multiple Coulomb scattering, allowing an higher resolution in close lateral proximity of organs at risk [65]. Helium also has a cost/benefit ratio of implementation more affordable than higher LET ions and, compared to carbon, helium is convenient because of its reduced nuclear fragmentation effect, especially in

Fragment	E (MeV)	LET (keV/ μm)	Range (μm)
^{15}O	1.0	983	2.3
^{15}N	1.0	925	2.5
^{14}N	2.0	1137	3.6
^{13}C	3.0	951	5.4
^{12}C	3.8	912	6.2
^{11}C	4.6	878	7.0
^{10}B	5.4	643	9.9
^8Be	6.4	400	15.7
^6Li	6.8	215	26.7
^4He	6.0	77	48.5
^3He	4.7	89	38.8
^2H	2.5	14	68.9

Tabella 2.1: Average data for target fragments from a 180 MeV proton beam in water, estimated according to a semi-empirical formula.

the tail after the Bragg peak. This is an important constraint, particularly in case of tumor treatments where the dose coverage should necessarily stop right after the target. Recent measurements have started feeding data for helium ions [66, 67, 68], and FOOT will allow to extend also this database with unprecedented accuracy.

Once the nuclear cross sections database will be sufficiently populated, it will be possible to improve the MC nuclear models by matching them to the experimental data. This will give birth to new data-tuned MC simulations, that will allow the extrapolation of further cross sections at beam energy not explored by the experiments.

Radioprotection in space

Knowing fragments spectra is of great importance to determine the astronauts dose exposure in far from Earth missions and to design proper shielding systems. An additional purpose of the FOOT experiment is to measure fragmentation cross sections for beams at higher energies. Helium, carbon and oxygen beams fragmentation processes will be explored at energy around 700 MeV/u, since these high energy nuclei are com-

Physics	Beam	Target	Energy (MeV/u)	Kinematic approach	Facilities
Hadrontherapy, target frag.	^{12}C	C, C ₂ H ₄	200	Inverse	CNAO, HIT, GSI
Hadrontherapy, target frag.	^{16}O	C, C ₂ H ₄	200	Inverse	HIT, GSI
Hadrontherapy, beam frag.	^4He	C, C ₂ H ₄ , PMMA	250	Direct	HIT, GSI
Hadrontherapy, beam frag.	^{12}C	C, C ₂ H ₄ , PMMA	350	Direct	CNAO, HIT, GSI
Hadrontherapy, beam frag.	^{16}O	C, C ₂ H ₄ , PMMA	400	Direct	HIT, GSI
Space radioprotection	^4He	C, C ₂ H ₄ , PMMA	700	Direct	GSI
Space radioprotection	^{12}C	C, C ₂ H ₄ , PMMA	700	Direct	GSI
Space radioprotection	^{16}O	C, C ₂ H ₄ , PMMA	700	Direct	GSI

Tabella 2.2: Overview of the FOOT research program. PMMA refers to Poly(methyl methacrylate) whose chemical formula is C₅O₂H₈.

monly present in the *Galactic Cosmic Radiation* (GCR) spectrum⁷.

An overview of the FOOT research program, including beams, targets and energies that will be investigated, is listed in table 2.2.

2.2 Experimental setup

2.2.1 Design Criteria

The detector has been mainly designed to satisfy the radiobiology outcome request, as the need to detect very short range (order of tens of μm) and very low energy (few MeV) fragments produced by the target fragmentation of proton beams. The inverse kinematic approach requires momentum and energy measurements with a few percent level accuracy and resolution on the measurement of the emission angle of the order of few mrad (see section 2.3).

FOOT has been designed to be a fixed target experiment: the beams of interest, in the energy range previously reported, impinge on a material representative of the human tissue and the produced fragments are detected and measured. The targets composition

⁷The GCR consists of protons and heavier nuclei emitted from supernovae within our galaxy. The energy spectrum is peaked in the MeV-GeV region, however the energy can reach values up to 10^{21} eV.

has been set according to the human body composition, that is mostly hydrogen, carbon and oxygen, thus materials such as C_2H_4 and PMMA have been selected as the main targets of interest.

The experimental setup is intended to be relatively small (about 1 – 2 m) and completely transportable (*table top setup*). This choice has been made for two reasons:

- not all the beam type needed are available in the same research facility, so it is important to be able to move the experiment from place to place easily;
- the experimental and treatment rooms where ion beams of therapeutic energies are available are of limited size.

Another main constraint in the design of the experimental setup is the redundancy of the fragment features measurement: contemporary detection of momentum, velocity, energy loss and kinetic energy are needed to study with limited systematics the produced fragments in the energy range of interest.

An important issue to consider is that lower mass fragments (such as protons, deuterons, etc.) can be emitted within a wider opening angle with respect to heavier nuclei, and this makes it difficult to achieve the desired acceptance for all secondary fragments with an apparatus of limited size. In order to not increase the size of the apparatus, which would compromise its portability, a solution that involves the use of two different setups has been adopted:

1. a *magnetic spectrometer* based on electronic detectors, aiming to the identification and measurement of fragments heavier than helium ($Z \geq 3$), covering an angular acceptance of ± 10 degrees with respect to the beam axis;
2. an *emulsion spectrometer* to measure the production in target fragmentation of light charged fragments as protons, deuterons, tritons, helium and lithium nuclei, extending the angular acceptance up to about ± 70 degrees.

The analysis that will be presented in the following chapters has been performed with the magnetic spectrometer, but, for completeness, both the setups will be described.

2.2.2 Electronic setup for heavy fragment detection

The FOOT electronic setup aims to experimentally measure the production cross section of $Z \geq 3$ fragments. The fragment mass identification (mass ID or isotopic ID) is performed combining the measurements of the particle momentum, kinetic energy and time of flight. The charge ID, instead, is derived from the Bethe-Bloch formula (eq. 1.1) after the evaluation of the energy loss (dE/dx) and the time of flight (from which it is possible to obtain β).

This setup is composed of several detectors which can be grouped into three regions.

1. *Pre-target region*: designed to monitor the primary beam, this region is located upstream with respect to the target and it is made up of the Start Counter and the Beam Monitor.
2. *Magnetic spectrometer*: it is designed to measure the fragment momentum and trajectory, and it includes two Halbach magnets, the Vertex detector (positioned upstream with respect to the magnets), the Inner Tracker (located between the magnets) and the Microstrip Silicon Detector (downstream with respect to the magnets).
3. *Downstream region*: a plastic scintillator system and a calorimeter are the last detectors composing the FOOT electronic setup;

The detectors can be placed at different distances from the target, depending on the beam energy. At 200 MeV/u the magnet and Inner Tracker system is placed at ~ 30 cm from the target, the Microstrip Silicon Detector is placed at ~ 60 cm, while the scintillator and calorimeter system is ~ 1 m away from the target. At higher beam energy (700 MeV/u) the system will be shifted forward (~ 30 cm for the magnets and the Inner Tracker, ~ 60 cm for the Microstrip Silicon Detector and ~ 2 m for the scintillator and calorimeter), in order to increase the magnetic region length and improve the momentum resolution. The expansion of the longitudinal dimension of the apparatus leads to a decrease in the angular aperture but, this does not reduce the geometrical acceptance, thanks to the smaller emission angle of the more energetic nuclear fragments.

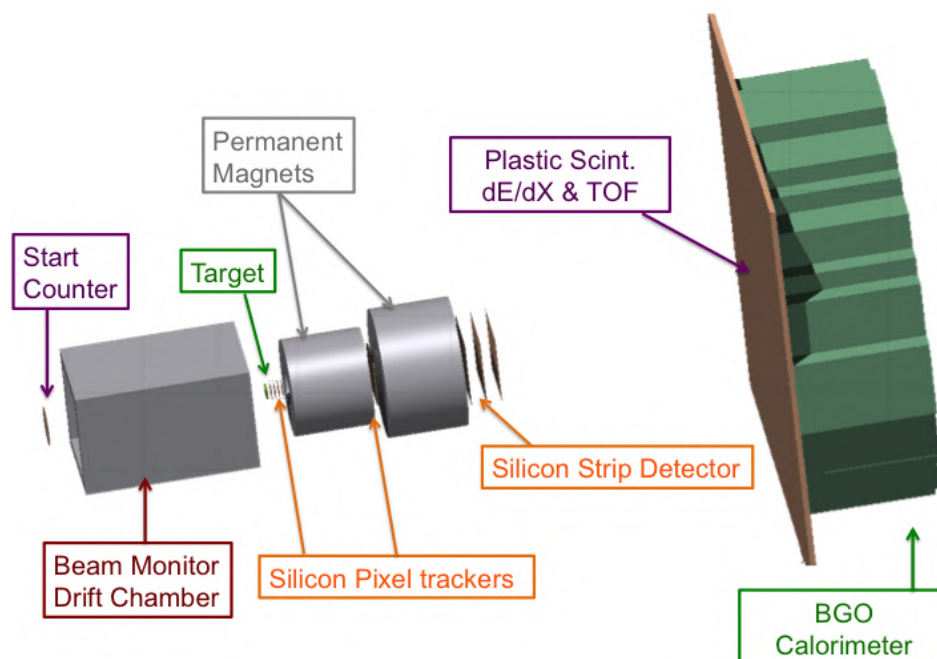


Figura 2.3: Schematic view of the FOOT electronic setup [69].

The reference frame of the apparatus forecast the z -axis along the beam direction, while the x -axis and the y -axis respectively represent the horizontal and the vertical axis of the transverse plane. Below we will discuss each detector in more details. A schematic picture of the whole apparatus is shown in figure 2.3.

Start Counter

The *Start Counter* (STC) is a plastic scintillator foil, placed 30 cm before the target, that monitors the primary particles rate, gives the trigger signal for event acquisition, counts the number of primary particles and provides the event initial time. This last information, together with the time reported by the scintillator in the downstream region, provides the time of flight (ToF) measurement.

The STC is composed of a layer of EJ-204 plastic (fig. 2.4), characterized by a rise time of 700 ps and a light yield of 10000 ph/MeV. The transversal dimensions are about 5 cm \times 5 cm. Four read-out channels are located one for each side of the square consisting

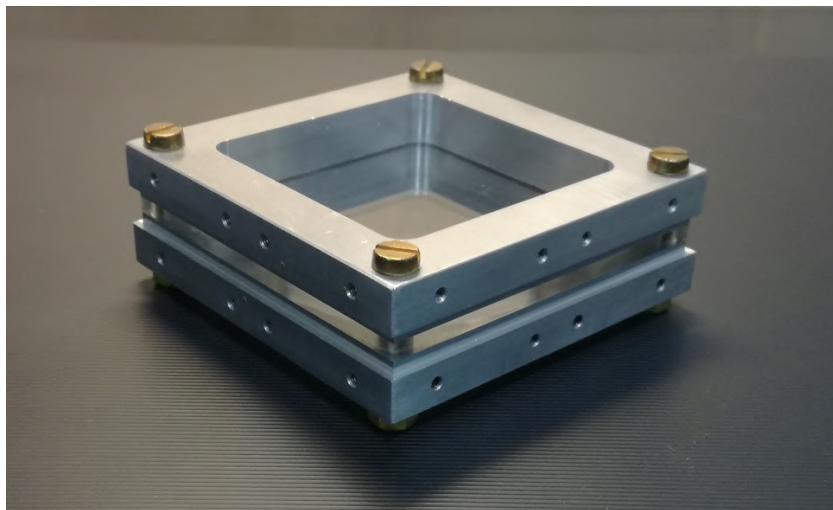


Figura 2.4: Picture of the Start Counter mechanical frame.

of the STC, each one composed of 12 Silicon Photomultipliers (SiPMs).

The thickness of the plastic layer is the result of a compromise between the maximization of the light output and the minimization of the probability of fragmentation within the detector. A reasonable thickness value ranges between $250\ \mu\text{m}$ and $1\ \text{mm}$, depending on the beam energy.

Since the ToF measurement is crucial to achieve the desired mass ID resolution, the STC time resolution has to match the time resolution of the other scintillator detector. Therefore, STC aims for a time resolution of about $30\text{-}40\ \text{ps}$ for the incoming beam particles (C and O). A $250\ \mu\text{m}$ prototype has been tested at GSI in April 2019 with $400\ \text{MeV/u}$ oxygen beams.

Beam Monitor

The *Beam Monitor* (BMN) is a $11\ \text{cm} \times 11\ \text{cm} \times 21\ \text{cm}$ drift chamber filled with Ar/CO_2 $80/20\ \%$ gas placed between the STC and the target. This detector has already been used in the FIRST experiment [70] and it is composed by 12 planes of alternated horizontal and vertical wires. Thanks to its low density material, the drift chamber represent the ideal detector, since it minimize the MCS and the production of fragments within the detector. In figure 2.5 a technical draw of the BMN is shown, while figure 2.6 shows a picture of the inside of the drift chamber.

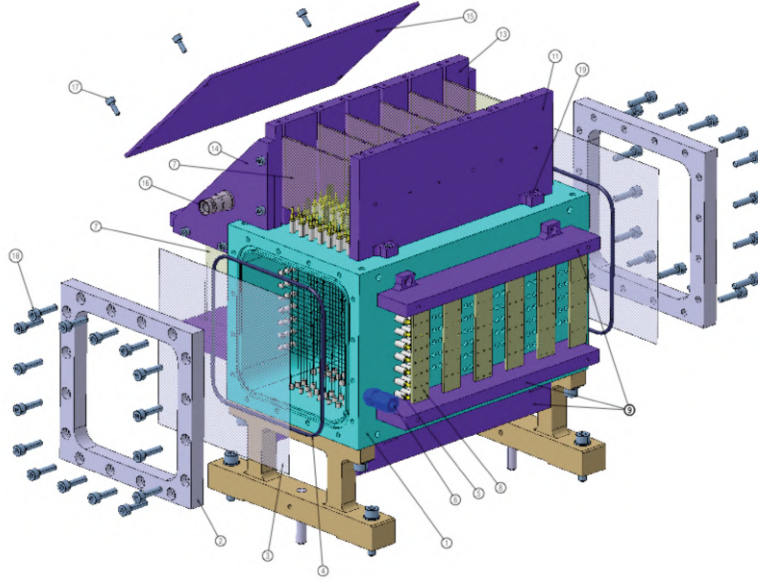


Figura 2.5: Technical draw of the beam monitor [69].

The function of the BMN is to measure the direction and impinging point of the ion beam on the target, that is necessary to address the pile-up ambiguity in the vertex detector, whose read-out time is equal to $187 \mu\text{s}$. A shorter read-out time of $1 \mu\text{s}$ or less makes the BMN fast enough to ensure that tracks belonging to different events cannot be mixed. In pile-up events, the vertices reconstructed in the pixel vertex detector are randomly distributed with a shape dictated by the transverse size of the beam, that is a gaussian shape with FWHM (Full Width at Half Maximum) of the order of a few mm. The positions of the vertices reconstructed by the vertex detector for each event can be compared with the position of the BMN track extrapolated to the target, and only the closest is selected as matched vertex. For this reason, a precision of few hundred μm in the impact point provided by the BMN and a good alignment between BMN and vertex detector are needed to discriminate the right vertex in pile-up events. Moreover, an accurate measurement of the direction of primary particles is required to obtain the primary 4-momentum, that is necessary to perform the Lorentz boost in the inverse kinematic approach (section 2.3). The achievable resolution of the BMN is about $150 - 200 \mu\text{m}$ for position measurements and $\sim\text{mrad}$ for angular measurements.

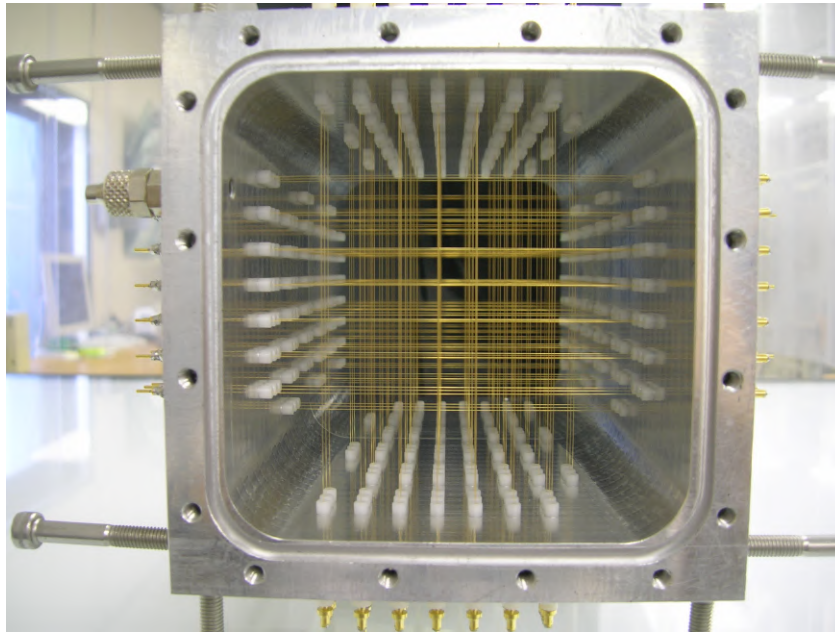


Figura 2.6: Photo of the inside of the Beam Monitor.

The BMN is equipped with a front-end electronics which pre-amplifies the signals that are then digitized by a *Time to Digital Converter* (TDC). Thanks to a dedicated electronics, the BMN is also able to detect multi-track events, allowing the rejection of the events in which the primary ion has fragmented in the STC. The tracks inside the cells will be reconstructed via dedicated Kalman filter algorithm.

The first experimental test ran on December 2018 at Trento protontherapy center, in order to calibrate the space-time relations between the wires, assess the single cells efficiency and the spatial resolution.

Magnet system

The magnetic field will be provided by two permanent magnets in Halbach configuration, each composed of twelve blocks of magnetic material arranged in a ring shape (figure 2.7) and inserted in an aluminum case.

The magnetic blocks are made of $\text{Sm}_2\text{Co}_{17}$, a material particularly suitable for resisting the radiation emitted by the beam interactions (mainly neutron, protons and He ions). In fact, recent studies [71] about the demagnetization of different permanently

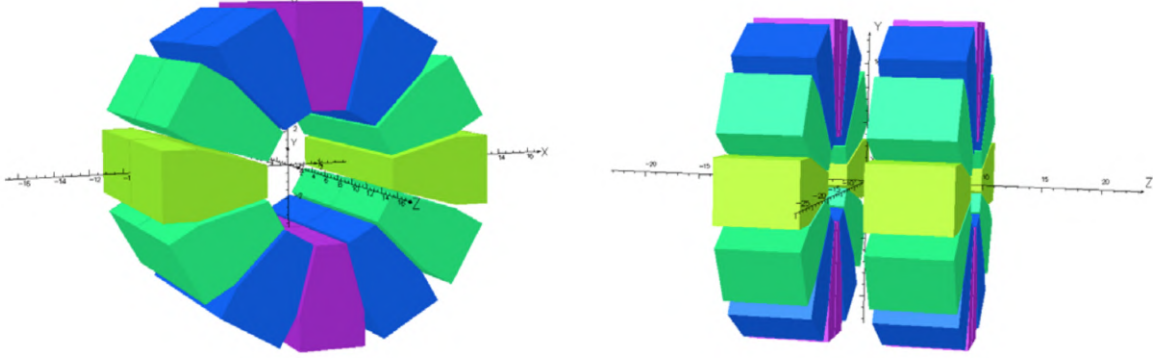


Figure 2.7: 3D model of the two magnets in Halbach configuration designed for the magnetic spectrometer [69].

magnetic materials proved that $\text{Sm}_2\text{Co}_{17}$ is particularly insensitive to radiation exposure compared to other permanent magnets. Otherwise, radiation exposure would degrade and damage the magnets, thus altering the produced field.

The Halbach configuration ensures an approximately uniform field in the internal hole, along the y direction (B_y), while the x and the z components are negligible. The solution with two magnets has been preferred to a single magnet in order to place an intermediate detector for momentum measurement (the Inner Tracker). This implies that the magnetic field as a function of z assumes a double gaussian trend, as can be seen in figure 2.8.

The momentum measurement resolution can be enhanced by maximizing the particle deflection, or the gained transverse momentum Δp_T .

$$\Delta p_T = q \int_0^L B dl \quad (2.1)$$

where q is the particle charge, B the intensity of the magnetic field and L is it is the length of the region in which the magnetic field is applied. The field intensity B in the Halbach configuration is proportional to the ratio between the external and internal radii, R_{out} and R_{in} :

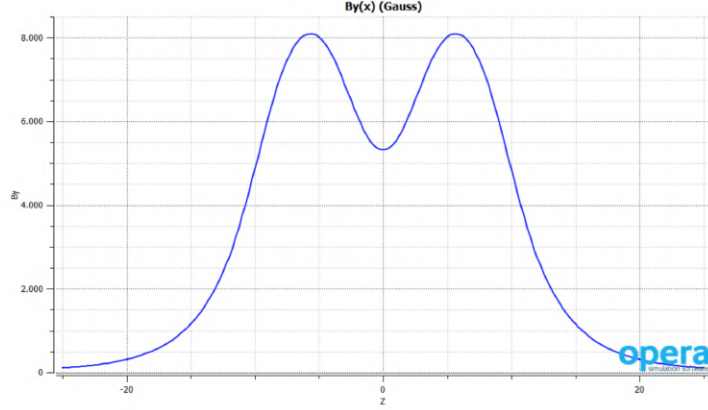


Figura 2.8: Magnetic field intensity B as a function of z along the beam central axis ($x = y = 0$). The plot shows the double gaussian trend produced by two separated Halbach magnets (simulation performed with the OPERA code version 16R1) [69].

$$B \propto \ln \left(\frac{R_{\text{out}}}{R_{\text{in}}} \right) \quad (2.2)$$

The value of R_{in} is assessed by the angular aperture of fragments and the distance between the magnet system and the target, while R_{out} value must be chosen as a compromise between the desired B field intensity and the cost. A B field with a maximum value of 0.8–0.9 T is a reasonable choice, and higher value may be difficult to obtain due to saturation effects arising around 1.19 T. Also the length of the magnets has to be chosen considering both the desired particle deflection and costs. At present, the magnets are chosen to be about 10 cm long and 10 cm thick; the magnet closest to the target has an internal radius $R_{\text{in}} = 2.5$ cm, while for the other one $R_{\text{in}} = 5.3$ cm.

Vertex detector

The Vertex detector (VTX) is a stack of four MIMOSA28 (M28) silicon chips [72] belonging to the family of the CMOS Monolithic Active Pixel Sensors (MAPS), which are commonly used for experiments in particle and heavy ion physics. The architecture of the MIMOSA28 integrates a fast binary read-out and a zero suppression logic to reduce the amount of data produced. Inside the read-out board there is the sensor, which is

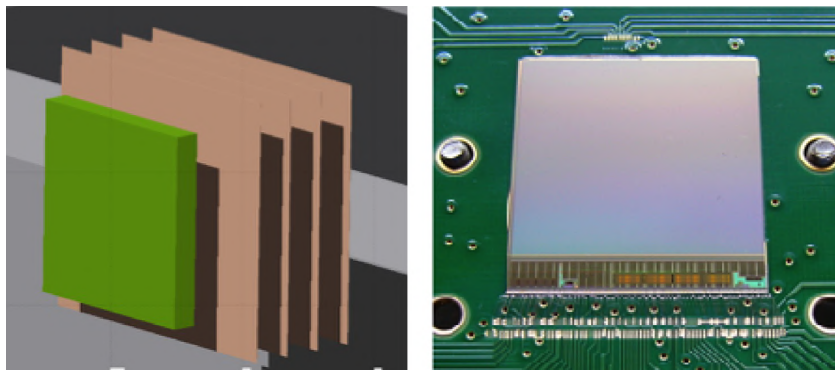


Figura 2.9: Target and vertex tracker geometrical scheme (left) and a M28 pixel sensor picture (right) [69].

composed of a 928×960 matrix of pixels, $20.7 \mu\text{m}$ pitch, for a total sensitive area of $20.22 \text{ mm} \times 22.71 \text{ mm}$. Each sensor is $50 \mu\text{m}$ thick. The VTX stack will consist of two substations with two sensors each: within the same sub-station the sensors will be placed at a relative distance of 2 mm to each other, while the two sub-stations will be separated by about 10 mm due to the size of the board electronic components. Figure 2.9 shows a geometrical scheme of the VTX and a picture of a M28 sensor.

The VTX detector is placed right after the target ($\sim 0.5 \text{ cm}$) as the first tracking station of the magnetic spectrometer, it contributes to reconstruct the particle track in the magnetic field in order to measure the particle momenta and it evaluate the vertex position for each event, i.e. the position inside the target where the beam interacted, originating the fragments. When a charged particle crosses the sensor, it produces a signal in a number of pixels which is proportional to the energy loss. Figure 2.10 shows the results obtained with two M28 sensors at the BTF (Beam Test Facility) at INFN Frascati laboratory: in the first two plots the beam profile can be seen. By means of dedicated reconstruction clusterization algorithms an accuracy of few μm on the particle position can be achieved.

Inner tracker

The *Inner Tracker* (ITR) is the second detector of the tracking system located between the two magnets. Like the VTX, the ITR is made of M28 chips, but, accordingly to the

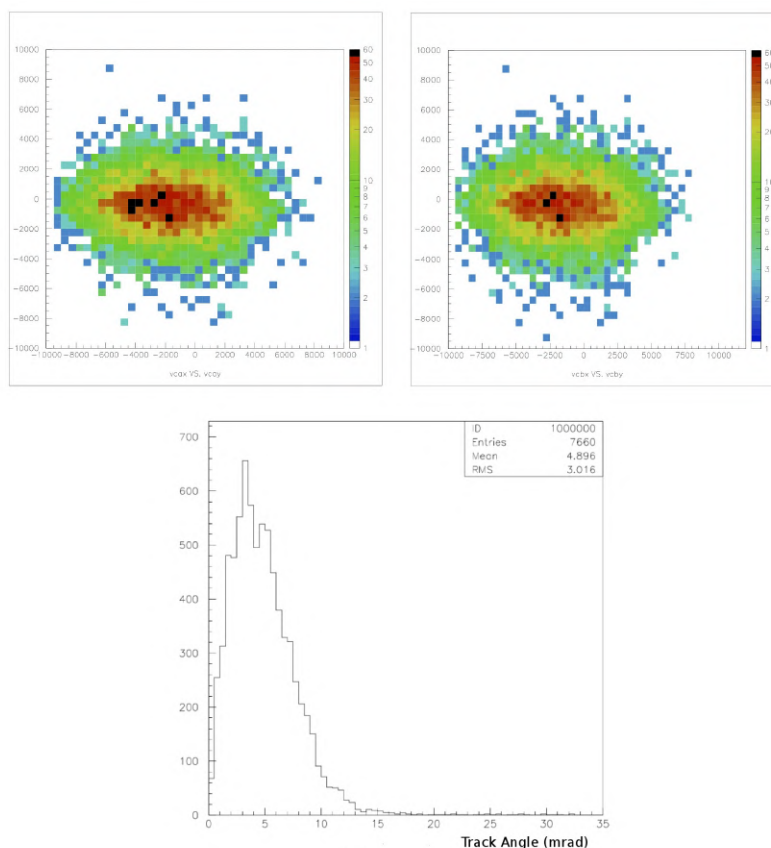


Figure 2.10: Upper left and right panel: beam profile in the two M28 sensors (units on both axes are in μm). Bottom panel: reconstructed angular divergence of the beam in mrad [69].

emission angle, the fragment spatial distribution is broader at at this point, since the inner tracker is farther from the target (at a distance of about 16 cm) than the Vertex. For this reason, the area to be covered is larger and a different spatial configuration is needed. The structure employed is composed of ladders similarly to the ones implemented in the PLUME project [73]: in the FOOT setup, each ladder is composed by two modules housing four M28 pixel sensors each. Four of these ladders will be disposed as sketched in figure 2.11, implementing a double plane tracker that covers a total area of about $8\text{ cm} \times 8\text{ cm}$. In each module the four sensors are glued and bonded on a kapton Flexible Printed Cable (FPC), having two or three conductive planes and an overall thickness

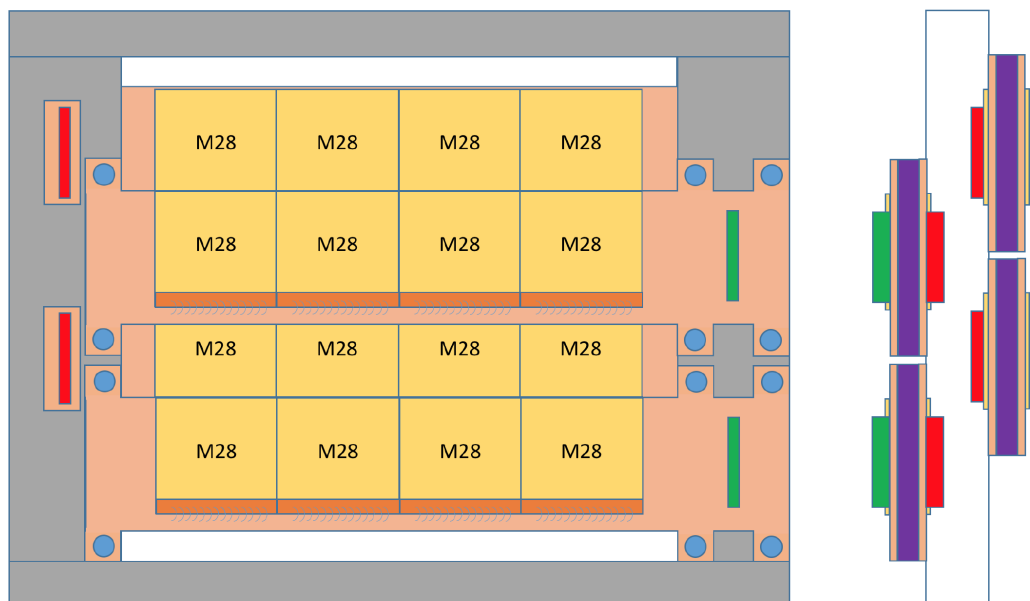


Figura 2.11: Inner tracker scheme. On the right we see how the four modules are located in the global structure. Each module has two connectors, in red and green color, respectively on the front and back side of the ladder [69].

of about $100\ \mu\text{m}$. The two modules of the same ladder are glued on a 2 mm layer of silicon carbide low-density foam, which determines the distance between the modules. To minimize the horizontal dead area the distance between two consecutive sensors in the same module is about $30\ \mu\text{m}$, as in the PLUME project.

As can be seen in figure 2.8, the inner tracker, sitting in-between the two magnets ($z = 0$ in the plot), experience a magnetic field of about $0.5 - 0.6\ \text{T}$, depending on the distance from the magnets. Even though the residual magnetic field is not negligible in this position, sensor performances are not significantly affected, as reported in [74]

Microstrip Silicon Detector

The Microstrip Silicon Detector (MSD) consists of a telescope of three microstrip layers placed downstream with respect to the magnets and about 30 cm away from the target. As the final station of the magnetic spectrometer, the purpose of the MSD is to give information about the track position to contribute to the momentum reconstruction



Figura 2.12: Picture of a MSD layer prototype.

but, due to its analogue electronics, it also provide a measurement of the fragments energy loss ΔE . The latter constitutes a redundant measure with the one provided by the scintillator, in order to have two separated and independent estimation of the ΔE .

The sensor employed in each MSD layer is of the SSSD type (*Single-Sided Strip Detector*): it is composed of two $150\ \mu\text{m}$ thick planes of micro strips (orthogonally oriented with respect to each other), glued together by means of biadhesive kapton (fig. 2.12), and it covers a total area of about $9\ \text{cm} \times 9\ \text{cm}$, accordingly to the $\pm 10^\circ$ opening angle needed to include ions with $Z > 2$. Each sensor is $2\ \text{cm}$ separated from the one in the following layer. The total thickness of each layer of the MSD ($300\ \mu\text{m}$) can provide a good ΔE measurement, however it can also represent a problem in terms of MCS and re-fragmentation. A strip pitch of $125\ \mu\text{m}$ has been chosen as a good compromise between the resolution requirements and a reasonable number of readout channels; a spatial resolution $< 35\ \mu\text{m}$ can be achieved with an analogue readout.

The read-out chip has been tested in Trento and Laboratori Nazionali del Sud (LNS), anyway, in that occasion, another type of sensor was used ($300\ \mu\text{m}$ thick *Double-Sided*

Strip Detector). It has been verified that no saturation occurs, even using low energy ions.



Figura 2.13: Picture of a SCN bar prototype (left) and the entire scintillator (right).

Scintillator detector

The *Scintillator detector* (SCN) is composed of two layers of 20 orthogonally oriented plastic scintillator bars (EJ200), each one 40 cm long, 2 cm large and 3 mm thick, coupled at both ends to up to four silicon photomultipliers (SiPMs) by means of an optical glue (fig. 2.13). The SCN is placed 1 m away from the target and it covers a square area of 40 cm \times 40 cm, according to the fragments aperture at that distance.

The SCN has the purpose of both measuring fragments energy loss ΔE and crossing time, in order to stop the time of flight measurement. The detector granularity has been chosen according to the fragments expected separation at 1 m. The bars thickness, instead, is a compromise between the accuracy of ΔE measurements and the effort to reduce the secondary fragmentation probability. In fact, a thicker bar would provide a higher light output and therefore an improved ΔE resolution but, due to the longer thickness to be traversed, it would also enhance the probability of re-fragmentation, thus spoiling the ΔE measurement.

In order to study the detector energy and time resolutions, expected light attenuation inside the bars and position reconstruction capability, an experimental campaign have been carried out at Trento Proton Therapy Center and at CNAO [75]. Two prototype bars have been exposed to proton and carbon ion beams at different energies (ranging from 60 to 230 MeV for protons and from 115 to 400 MeV/u for carbon ions). The

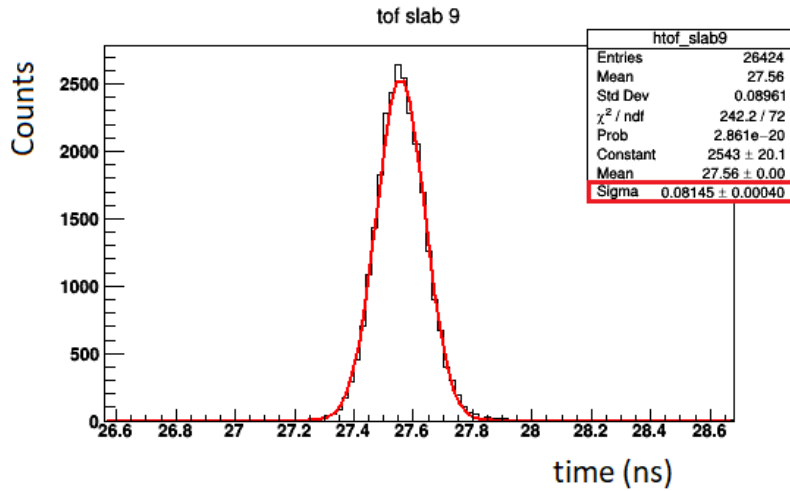


Figura 2.14: STC-SCN measurement of the time of flight performed at the GSI test beam (April 2019) with the electronic setup. The standard deviation of the fitted distribution (boxed in red) represents the time resolution.

energy resolution obtained ranges between 6% for heavier ions and 13% for the lighter ones. The resolution obtained on time measurement is about 50 ps for carbon ions and about 100 ps for protons. The test also proved that the energy collected at the two ends of the bar is a function of the beam impinging position, as a result of the attenuation effect of the scintillator material, therefore, this dependence can be exploited to retrieve the interaction position.

The convolution of the time resolution of the STC and the SCN gives, at the moment, a precision of about 80 ps in the ToF measurement, as observed at the GSI test beam (fig 2.14). In the next future, a set of improvements is planned to reach a ToF precision of about 50 – 60 ps.

Another study has been performed at CNAO in 2019 in order to calibrate all the scintillator bars: each bar has been systematically irradiated in different points along its length with the carbon beam provided by the CNAO facility at different energy.

Calorimeter

The *calorimeter* (CAL) is the most downstream detector. It will be composed of 288

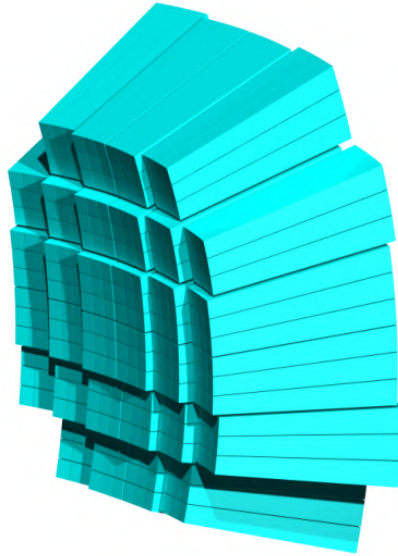


Figura 2.15: Schematic view of the CAL crystals setup.

crystal of *bismuth germanate* (BGO) arranged in a pointing geometry (fig. 2.15). Each crystal is 24 cm long, with a front face area of about $2 \times 2 \text{ cm}^2$ and an outer face area of $3 \times 3 \text{ cm}^2$ and it will be read-out by $8 \times 8 \text{ mm}^2$ SiPMs. The CAL is designed to measure the kinetic energy of the fragments that stop inside it.

Recent tests to study the energy resolution have been performed with proton, ^4He and ^{12}C at HIT, it has been demonstrated that a relative energy resolution ranging between 1 – 3 % can be achieved. Other tests have been performed at GSI, using 400 MeV oxygen beams, and at CNAO with proton and carbon beams of different energy; energy resolutions less than 1 % has been obtained for heavy ions (fig. 2.16).

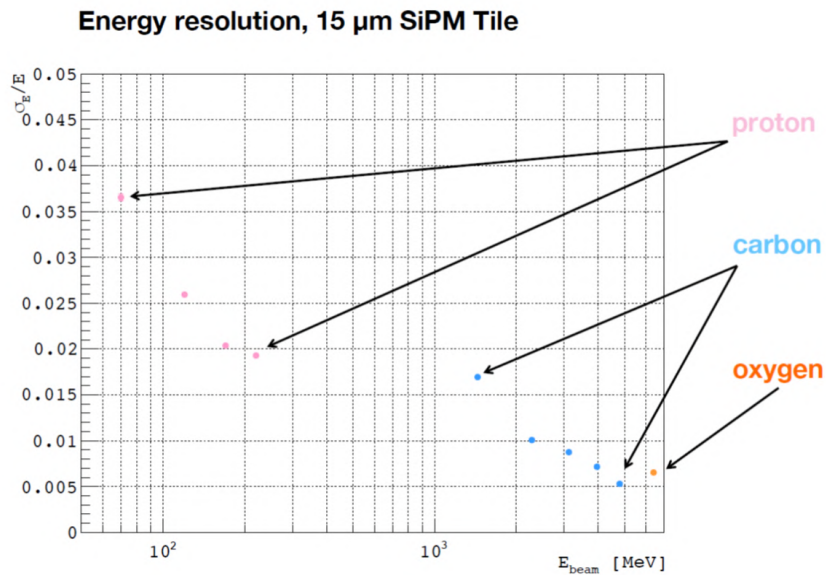


Figura 2.16: Energy resolution of the BGO crystals as a function of energy for different particle beams obtained at GSI and CNAO.

A non negligible issue associated with this kind of detector is the production of neutrons: when a particle undergoes nuclear interaction inside a crystal, one or more neutrons can be produced. Neutrons can escape the calorimeter, carrying away part of the energy and thus spoiling the measure of kinetic energy, which would be lower than it should be.

The resolutions, at the present state of art, of all the detectors shown so far are listed in table 2.3.

Detector (measurement)	Resolution
BMN (position)	100 – 200 μm
BMN (position)	~ 1 mrad
VTX (position)	6 μm
ITR (position)	6 μm
MSD (position)	< 35 μm
MSD (energy loss)	$\sim 18 - 30$ %
SCN (energy loss)	6 – 12 %
SCN (time)	50 – 100 ps
STC+SCN (ToF)	~ 80 ps
CAL (kinetic energy)	0.5 – 3 %

Tabella 2.3: Current resolution of the detectors of the FOOT electronic setup.

2.2.3 Emulsion setup for light fragments detection

The setup designed to measure light fragments ($Z \leq 3$), which are distributed with a wider angular aperture than the heavier ones, shares the pre-target region with the electronic setup, while the target and all the remaining part of the setup are replaced by an *Emulsion Spectrometer* (ES) based on the *Emulsion Cloud Chamber* (ECC) concept [76], that allows the detection of fragments produced with an emission angle up to 70° with respect to the axis of the incident beam (fig. 2.17). The choice to use this kind of detector is due to the fact that a calorimeter (and, in general, all the other detectors), to reach the same angular coverage, should have a transversal size of several meters. Therefore, the realization of such a detector would be extremely disadvantageous for economic reasons and would compromise the portability of the apparatus.

The fragments that enter the emulsion chamber pass through several layers of material, including emulsion films which record their passage, and gradually lose energy until they stop. The emulsion films employed for FOOT are similar to the ones used in the OPERA experiment [77] and they are composed of 70 μm thick sensitive layers made of AgBr crystals of 0.2 μm diameter scattered in a gelatine binder and placed on the two sides of a 180 μm plastic base (fig. 2.18), with a total thickness of 320 μm and a

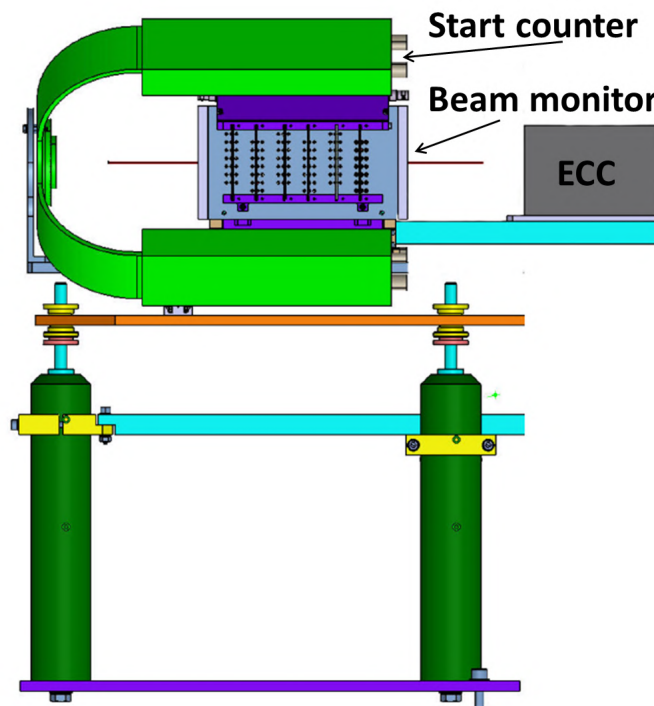


Figura 2.17: Emulsion spectrometer setup inside the FOOT detector [69].

transversal area of $12 \text{ cm} \times 10 \text{ cm}$.

The silver bromide is excited by the passage of light or charged particles and this makes the crystals more sensitive to the action of the developer, so that the transformation of silver bromide into metallic silver occurs more rapidly than those crystals that have not absorbed energy. In other words, the absorption of energy in a silver bromide crystal leads to a concentration of some silver atoms in small clusters (or grains), with diameter of $\sim 0.6 \mu\text{m}$, that can be observed at optical microscope [78]. The sequence of clusters determines the particle track, whose position and direction can be measured with high accuracy ($\sim 0.06 \mu\text{m}$ and 0.4 mrad respectively), while the energy loss, and thus the charge (see eq. 1.1), can be obtained from the cluster density (about 30 grains/ $100 \mu\text{m}$ for a minimum ionizing particle).

The grain density is proportional to the energy loss only over a certain energy range, above which a saturation effect takes place. To measure the energy loss of highly ionizing particles, such as carbon ions, emulsion films must be treated through a specific procedure

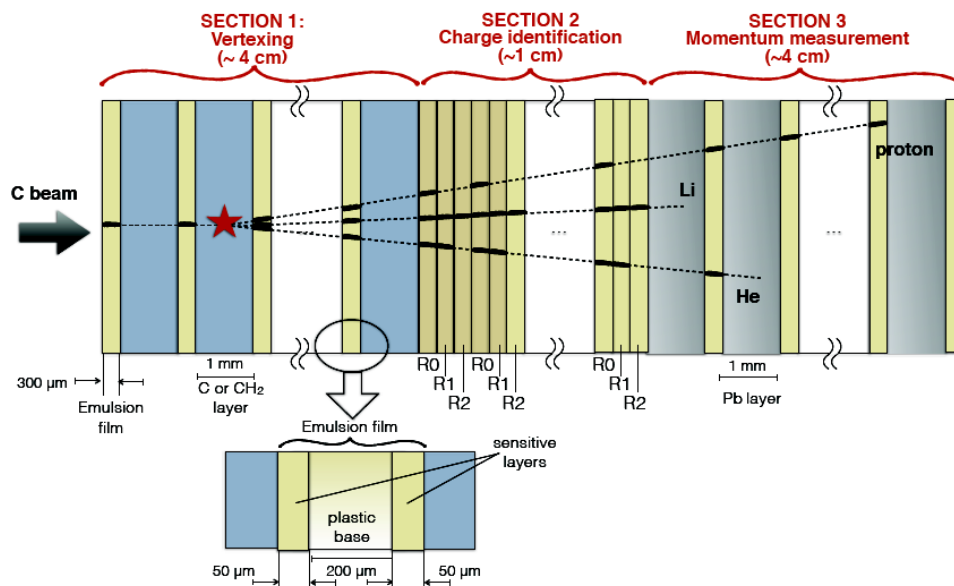


Figura 2.18: Schematic overview of the ECC layout (not to scale) [69] (è quello di OPERA?).

named *refreshing*, in order to partially or totally erase the tracks of particles and overcome the saturation effect. The refreshing procedure has to be done after the exposure and before the development of the emulsion film. The disentanglement of particles with different ionization powers, and thus with different charge can be achieved by combining several films having undergone different refreshing treatments.

The emulsion spectrometer is composed of three sections (fig. 2.18), in which there are different materials interspersing the emulsion film layers, each with a different role.

Target, Vertex and tracking detector

The first section consists of several elementary cells made of emulsion films ($300\ \mu\text{m}$) interleaved with 1 mm thick carbon or C_2H_4 layers (fig. 2.19). These passive layers act as targets, while the emulsions reconstruct the interaction vertex position with a micrometric resolution. The number of elementary cells has been optimized to achieve a statistically significant number of interactions: assuming that 20 % of all ^{12}C ions (400 MeV/u) interact within 30 mm of Carbon [79], the total length of this section should be 39 mm, corresponding to 30 elementary cells.

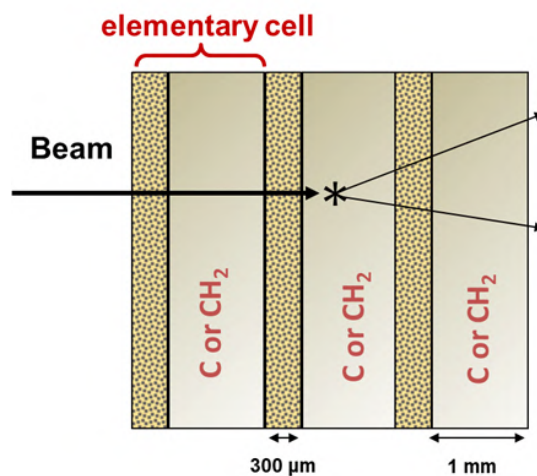


Figura 2.19: Scheme of the ES Section 1: vertex and tracking detector [69].

Charge measurement section

The second section is entirely composed of emulsion films with the aim of reconstruct the charge of light fragments. The elementary cell is made of three emulsion films, each of which is treated with a different refreshing procedure (fig. 2.20), in order to enlarge the dynamical range of the detector and identify particles with very different energy release.

By keeping the emulsions for an appropriate time at a relatively high temperature and relative humidity, the tracks can be partially or totally erased. In the FOOT experiment, the same method described in [78, 79] is adopted: the emulsion films, denoted as R_0 , R_1 and R_2 (fig. 2.20), are treated at different temperatures during the refreshing process. R_0 is not refreshed and it is developed soon after the exposure at room temperature (20°). R_1 and R_2 underwent a three days refreshing at 98% relative humidity and 30°C and 38°C , respectively. As the specific ionization along the particle track is proportional to the grain density, the sum of the grain pixels belonging to the same track normalized to a given track length is a variable sensitive to the specific ionization, hence to the particle charge, called *track volume*. For each refreshing condition, a track is characterized by three volume variables, referred to as VR_0 , VR_1 and VR_2 . The R_2 refreshing process results in a complete erase of all tracks caused by particles with charge equal to 1 and, therefore, only VR_0 and VR_1 are used for hydrogen identification. Helium and heavier nuclei are identified only by VR_1 and VR_2 , since VR_0 shows saturation.

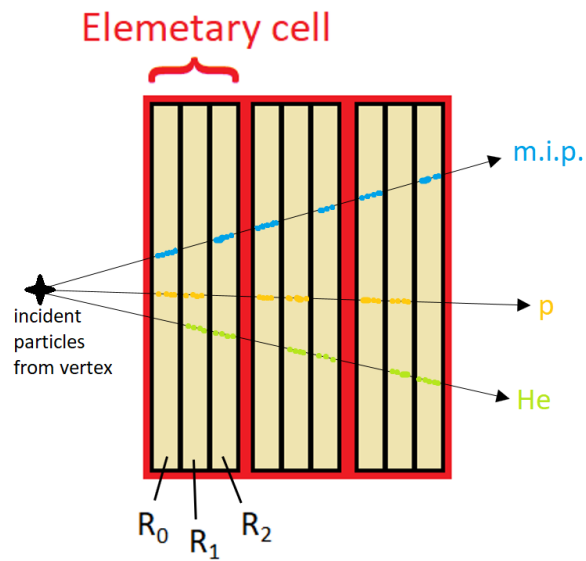


Figura 2.20: Scheme of ES section 2: charge identification detector.

In [78] it is shown that, in order to achieve an appropriately accurate separation between distributions of track volume variables, this section must be composed of 9 elementary cells, corresponding to a total length of at least 8.1 mm.

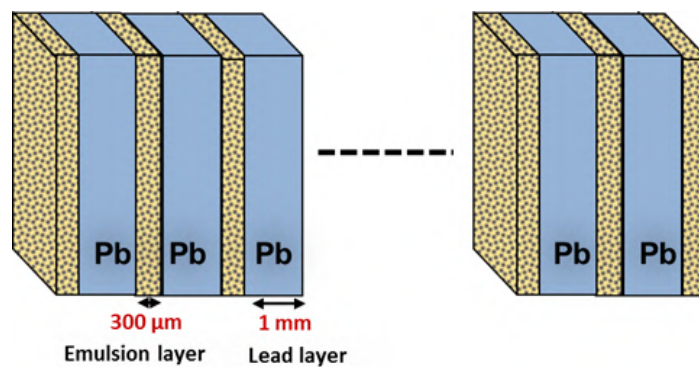


Figura 2.21: Scheme of ES section 3 dedicated to the momentum measurement [69].

Energy and mass measurements section

In the last section the emulsion films are interleaved with layers of high-Z material, in order to make the particles stop in the detector. The number of elementary cells, the

passive material composition and its thickness have to be optimized accordingly to the primary particle type and energy: reasonable choices are lead and tungsten, 1 – 2 mm thick, and a number of cells increasing with the energy of the primaries and ranging between 10 and 50 (fig. 2.21).

The purpose of this section is to evaluate the kinetic energy and the momentum by measuring the entire particle track length and obtain the mass measurement exploiting the correlation between them. The particles momentum can be estimated through the multiple Coulomb scattering method: by measuring the x - y spatial coordinates and the slope, the particle momentum p can be evaluated according to the formula

$$p = \frac{13.6 \text{ MeV}}{\beta \cdot \delta\theta} \sqrt{\frac{\Delta x}{X_0}} \quad (2.3)$$

where $\delta\theta$ is the deviation of the track slope along its path, Δx is the crossed thickness and X_0 is the characteristic interaction length of the traversed material. The kinetic energy of the particle can be obtained from the range of the particle, as described in section 1.1.2. Thus, energy and momentum are found with two independent procedures, allowing the isotopic determination of the fragments.

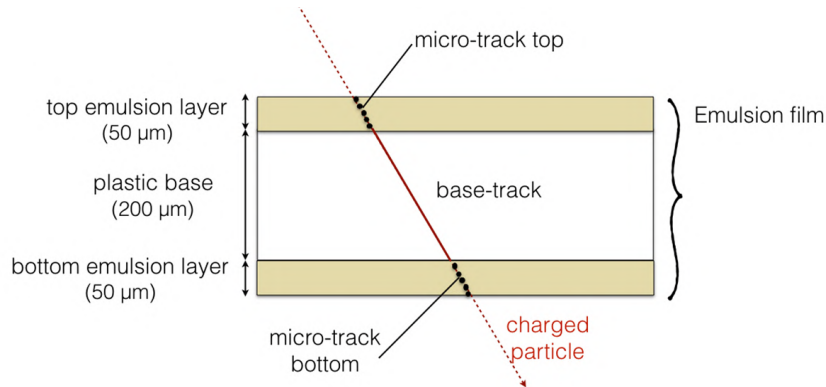


Figura 2.22: Scheme of the tracks reconstruction: a micro-track consists of a sequence of aligned clusters in one of the two layers (top or bottom), while a base-track is constituted by geometrically aligned top and bottom micro-tracks. [69].

Automatic emulsion readout

To be able to observe the tracks impressed on the nuclear emulsion films, an automatic scanning system is used: after the exposure to about 10^6 tracks, the films are developed and then scanned by an optical microscope equipped with an automatic system, which provide the set of measurements of the produced fragments in a short time. The automatic scanning technique was also adopted by the FIRST [70] and OPERA [80, 81] experiments.

Dedicated softwares are designated to recognize aligned dark pixels clusters corresponding to particle tracks. A straight sequence of pixels in one emulsion layer defines a micro-track, while two aligned micro-tracks belonging to the top and bottom layers of an emulsion film constitutes a base-track (fig. 2.22). Base-tracks aligned along different films are connected to form volume-tracks. Propagation and fit of the track segments from an emulsion layer to the next allows the particle track reconstruction.

In April 2019, at the GSI test beam, the emulsion spectrometer has been tested with 200 and 400 MeV/u oxygen beams both on C and C₂H₄ targets. The experimental setup used in this case, has included also a STC⁸ and the BMN. Since emulsions can be affected by a saturation phenomenon, due to a too high density of tracks (local pile-up occurs at a particle density of about 1000 tracks/cm²), the beam rate has been monitored by the STC, while the BMN was checking its transversal profile for absolute flux normalization. The ECC was placed on a remotely controlled table that allowed to move the detector in the transversal plane to the incoming beam direction, in order to uniformly distribute the beam on the chamber surface and keep the particle density below the saturation threshold.

The nuclear emulsion still remains the three-dimensional detection technique with the best spatial resolution, typically less than 1 μm , and with a dead time close to zero. The capability of this kind of detector to separate and measure different fragments produced by ion beams at therapeutic energy has already been proved [78].

⁸The Start Counter used in the emulsion setup is not the same used in the electronic setup, but a previous version with PMTs instead of SiPMTs

2.3 Inverse kinematic approach

In the context of target fragmentation, inverse kinematics consists in a role reversal between projectile particle and target particle, operating in a reference frame in which the fragments emitted from the target (which has become the projectile) receive a boost in the forward direction. This approach is particularly useful when the momentum of the projectile particle is not sufficient to produce target fragments with enough energy to allow their detection. This is the case of processes where proton beams at therapeutic energy are involved: a carbon or oxygen target would produce very short range (order of tens of microns) and very low energy (few MeV) fragments, which would not even be able to leave the target itself (few mm thick).

The inverse kinematic approach can be pursued, studying the fragmentation of different ions beams (C, O, Ca, etc.) onto a target made of an hydrogen enriched compound, such as polyethylene (C_2H_4). The choice of a pure gaseous hydrogen target have been discarded, since it would imply many technical difficulties, from the low interaction rate due to the low density, to the impossibility, due to safety reasons (because of hydrogen flammable characteristic), of handling such a target in the therapy centers where the experiment is intended. The cross sections σ onto H can be extracted by subtraction from the data obtained using a C_2H_4 target in combination with a pure C one [82]:

$$\sigma(H) = \frac{1}{4} \left(\sigma(C_2H_4) - 2\sigma(C) \right) \quad (2.4)$$

and in the same way for the differential cross sections

$$\frac{d\sigma}{dE}(H) = \frac{1}{4} \left(\frac{d\sigma}{dE}(C_2H_4) - 2\frac{d\sigma}{dE}(C) \right) \quad (2.5)$$

$$\frac{d\sigma}{d\Omega}(H) = \frac{1}{4} \left(\frac{d\sigma}{d\Omega}(C_2H_4) - 2\frac{d\sigma}{d\Omega}(C) \right) \quad (2.6)$$

where $\frac{d\sigma}{dE}$ and $\frac{d\sigma}{d\Omega}$ are the differential cross sections with respect to emission energy and angle respectively. The same method can be adopted to study the cross sections on

oxygen, using a PMMA target, since it is composed of carbon, hydrogen and oxygen. However, the disadvantage of this strategy is that the resulting cross section uncertainties are the quadratic sum of the uncertainties of the two single targets, therefore the cross sections on hydrogen have a larger error.

In order to apply the inverse kinematic approach, a Lorentz transformations is needed, which converts the coordinates between two different and inertial reference frames. Supposing the beam direction along the z -axis, in the laboratory frame S the target proton is at rest and the beam ion has a constant velocity β towards the target; on the contrary, in the patient frame S' the ion is at rest and the proton is moving along z with the same velocity β but in the opposite direction (the same velocity implies the same energy per nucleon). Being $\mathbf{P} = (E/c, \mathbf{p})$ and $\mathbf{P}' = (E'/c, \mathbf{p}')$ the 4-momenta of the ion in S and the proton in S' respectively, the proton 4-momentum components in the S' frame are given by

$$\frac{E'}{c} = \gamma \left(\frac{E}{c} - \beta p_z \right) \quad (2.7)$$

$$p'_x = p_x \quad (2.8)$$

$$p'_y = p_y \quad (2.9)$$

$$p'_z = \gamma \left(p_z - \beta \frac{E}{c} \right) \quad (2.10)$$

Using the matrix notation, eq. 2.7 – 2.10 become

$$\mathbf{P}' = \Lambda \mathbf{P} \quad (2.11)$$

which corresponds to

$$\begin{pmatrix} \frac{E'}{c} \\ p'_x \\ p'_y \\ p'_z \end{pmatrix} = \begin{pmatrix} \gamma & 0 & 0 & -\beta\gamma \\ 0 & 1 & 0 & 0 \\ 0 & 0 & 1 & 0 \\ -\beta\gamma & 0 & 0 & \gamma \end{pmatrix} \begin{pmatrix} \frac{E}{c} \\ p_x \\ p_y \\ p_z \end{pmatrix} \quad (2.12)$$

What has just been described is a *Lorentz boost* along the z -axis. The inverse Lorentz

transformation is

$$\mathbf{P} = \mathbf{\Lambda}^{-1}\mathbf{P}' \quad (2.13)$$

where $\mathbf{\Lambda}^{-1}$ is the $\mathbf{\Lambda}$ inverse matrix:

$$\mathbf{\Lambda}^{-1} = \begin{pmatrix} \gamma & 0 & 0 & \beta\gamma \\ 0 & 1 & 0 & 0 \\ 0 & 0 & 1 & 0 \\ \beta\gamma & 0 & 0 & \gamma \end{pmatrix} \quad (2.14)$$

showing that it is simply equal to $\mathbf{\Lambda}$ with a change of the sign of β .

The precision needed for the application of the inverse kinematics method, requires FOOT to measure the fragment production cross sections with maximum uncertainty of 5 %, which means that the detector aims to perform charge identification with an accuracy of 2-3 %, isotopic identification with an accuracy better than 5 % and measurements of the fragments energy spectra with an energy resolution of about 1-2 MeV/u (in the inverse kinematics frame). The required precision on the measurement of the emission angle, in order to apply the Lorentz boost, is a few mrad, which means that the MCS angle of the beam and the fragments inside the target must be kept below 1 mrad. For this reason, the target thickness is limited to 2 – 4 mm and its areal density must be of the order of 1 g cm⁻² or less. An even thinner target, of the order of μm , implies other kind of issues: mechanical problems due to the difficulty in handling such a fragile target and, most of all, an extremely reduced interaction rate, which imposes an excessively long beam time in order to collect a sufficient amount of data.

2.4 DAQ and trigger

The *Trigger Data Acquisition* (TDAQ) system of FOOT is designed to acquire the largest amount of data with high accuracy in a controlled and online-monitored environment. The maximum acquisition rate is set according to the beam characteristics and/or on the slowest detector in the experiment, in order to avoid bottlenecks along the TDAQ chain that would limit the rate itself. Since, due to the high number of read-out channels, the VTX of the magnetic spectrometer is the slowest detectors in the

Detector	Board	DAQ channels	Max event rate (kHz)	Event size (bytes)
Trigger	V2495	1	10	40 B
Start Counter	DreamWave	4	1	8.2 kB
Beam Monitor	TDC	36	5	0.1 kB
Vertex detector	SoC on DEx	$4 \cdot 10^6$	2	0.9 kB
Inner Tracker	SoC on DEx	$28 \cdot 10^6$	2	2.1 kB
Microstrip Detector	Custom	$6 \cdot 10^3$	2	0.5 kB
Scintillator system	DreamWave	80	1	8.4 kB
Calorimeter	QDC	400	2	1.7 kB
Total DAQ	Storage PC		1	22 kB

Tabella 2.4: DAQ components, rates and bandwidths

FOOT electronic setup, the maximum rate is dictated by its read-out time ($\sim 180 \mu\text{s}$), which fixes the overall maximum read-out rate at about 5 kHz. The system is designed to handle such a maximum DAQ rate but, in order to reduce pile-up effects in the M28 chips of the VTX, the actual trigger rate is kept at about 1 kHz.

Sources of systematics, due to the trigger selection, can be avoided by adopting a very simple request: the only signal from STC is enough to start the acquisition (minimum bias trigger). The trigger signal will be obtained asking for at least a time coincidence between a certain number of SiPMs signals in the STC within a small time gate. Both the number of SiPMs and the time gate value are still matter of study. The internal trigger is broadcasted to all detectors only if each of them is not in the BUSY status and enough time has passed, since the previous trigger, to allow the readout cycle to be completed. However, other trigger solutions will be explored: in fact, to avoid possible pile-up in the detectors, a more sophisticated trigger able to exclude the events in which the primary has not interacted with the target will be investigated.

The implemented TDAQ system is a flexible hierarchical distributed system based on linux PCs, VME crates and boards and standard communication links such as ethernet, USB and optical fibers, as already done in several experiments [83, 84]. Table 2.4 shows the TDAQ components employed for each detector in the electronic setup. The control of the system is hosted on a PC (Head PC), which is used to run the DAQ GUI interface to start/stop a single run, to control and to configure other nodes in the system. Another PC (Storage PC) collects the information coming from the different detectors, to perform

an event building and to store on disk the acquired data, the configuration data and other global DAQ information. The ethernet link is required by the TDAQ system for providing commands (and receiving feedback), while the data to be collected can use ethernet, USB or optical fibers to reach the Storage PC.

The DAQ system is equipped with several sets of online monitoring information. Simple pieces of information on the running TDAQ can be collected from each VME board or data provider at a monitoring rate (typically each 10 s) and provided to a network of PCs connected to the experiment. A second information comes in the form of histograms filled on each PC in the system using local data. Typical histograms show detector occupancies, particle arrival times, particle energies, collected charges and so on. A third and more powerful online information consists of a fast online event reconstruction performed on the fly on a fraction of events. With a complete reconstruction it is possible to have, on part of the data, track momentum spectra, times-of-flight, A and Z reconstructed for charged tracks.

Capitolo 3

Monte Carlo Data Analysis

The FOOT Monte Carlo (MC) simulation has been built with the FLUKA package [85], which is a general purpose MC tool developed by the INFN and CERN adopted in a wide range of applications, such as calorimetry, dosimetry, detector design, cosmic rays, neutrino physics, radiotherapy and many others. FLUKA is a theory driven MC code capable of simulating the transport and the interactions of particles in complex geometries, magnetic fields and in a wide range of materials. To this aim, FLUKA includes several theoretical models, such as electromagnetic interactions, Bethe-Block formalism, hadron-nucleon, hadron-nucleus and nucleus-nucleus interactions [86]. A more detailed description of the FOOT simulation can be found in [87].

The analysis discussed in the following sections has been carried out on data sets obtained with 2.5×10^8 simulated events of ^{16}O of 200 MeV/u of kinetic energy impinging on a C_2H_4 target. As a first selection, only the events in which the primaries fragmented into the target have been considered, for a total of about 2.8×10^6 fragmentation events (1.1% of the total primaries). Due to the lack of real data, in order to perform the entire analysis chain for the final differential cross section evaluation, we have divided these events into two halves: the events in the first group have been treated as if they were real data, therefore taking from them only the information that the apparatus could provide (track, momentum, ToF, energy loss, kinetic energy); the events of the second group have been treated as MC events, allowing us to extract all the true quantities and particle characteristic generated in the simulation, which are important to evaluate

Fragment	Symbol	Charge
Hydrogen	H	1
Helium	He	2
Lithium	Li	3
Beryllium	Be	4
Boron	B	5
Carbon	C	6
Nitrogen	N	7
Oxygen	C	8

Tabella 3.1: List of fragments produced in a fragmentation reaction induced by an oxygen-16 beam impinging on a C₂H₄ target.

background and efficiency.

To evaluate the differential cross sections, it is necessary, first of all, a unique identification of each produced fragment by determining its charge (number of protons) and its mass number (number of nucleons). This requires a measurement by each instrument of the apparatus, in order to obtain momentum, velocity, energy loss and kinetic energy of the fragments, necessary for their identification. For this reason, in each event, only those fragments whose track passed through each detector have been considered for the analysis.

3.1 Charge identification

In a fragmentation reaction induced by the collision of a ¹⁶O beam on a C₂H₄ target, the eight fragments listed in tab 3.1 are produced; these have been selected for charge identification.

According to the Bethe-Bloch formula (eq. 1.1), the charge of the fragments that pass through the detector can be reconstructed from the measurements of its velocity β and energy loss inside the scintillator. In the Bethe-Block formula the charge of the fragment is indicated by z , while in this chapter we will indicate it with Z so as not to confuse it with the z -axis of the FOOT reference frame. The other quantities in the eq. 1.1 are

Scintillator constant	Value
Thickness (d_{SCN})	0.6 cm
Density (ρ_{SCN})	1.023 g/cm ³
Ionization potential (I_{SCN})	64.684×10^{-6} MeV
$Z_{\text{SCN}}/A_{\text{SCN}}$ ratio	0.54157

Tabella 3.2: Scintillator characteristics included in the Bethe-Block formula for the fragment charge determination.

known, since they refer to characteristics of the detector, such as the density and the mass number of the scintillator material (tab. 3.2), or they are physical constants.

The dE/dx of the fragment can be obtained by dividing the measured energy deposition in the scintillator (ΔE) for the total thickness of this detector (0.6 cm):

$$\frac{dE}{dx} \approx \frac{\Delta E (GeV)}{0.6 (cm)} \quad (3.1)$$

In the real experiment the measure of ΔE is affected by fluctuations due to the detector resolution. For this reason a Gaussian smearing has been applied to the deposited energy values obtained with the MC simulation. The resolution of the deposited energy has been derived from several tests performed on beams using different particles at different energy; at the end, the best approximation resulted in a Gaussian smearing with a standard deviation $\sigma_{\Delta E}$ parameterised as follow:

$$\sigma_{\Delta E} = \left(Const + \frac{Slope}{\Delta E} \right) \Delta E \quad (3.2)$$

where *Const* and *Slope* are respectively equal to 0.0465 and 0.04 MeV (fig. 3.1). In addition, the resolution $\sigma_{\Delta E}/\Delta E$ has been limited in a range between 5% and 15%, as obtained at the already cited tests.

The velocity is derived from the time of flight (ToF) measurement, by the relation

$$\beta = \frac{L}{c \cdot ToF} \quad (3.3)$$

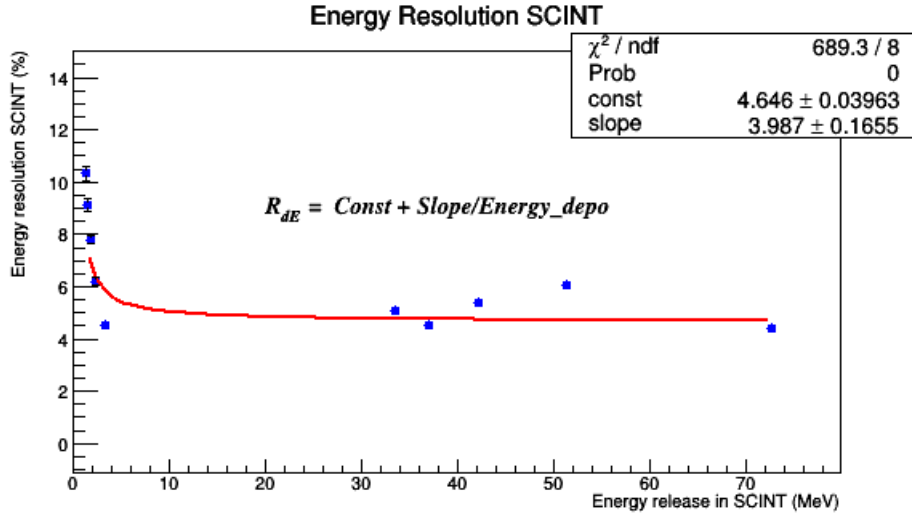


Figura 3.1: Energy resolution in the scintillator as a function of the energy deposition of the fragment.

where L is the distance traveled by the fragment since it was generated in the target up to the scintillator and the ToF corresponds to the time that the fragment takes to cover this distance. Since the time measurement is performed by the STC and the SCN, we have to subtract the time offset (t_{off}) from it, that is the time that a beam particle takes to travel from the Start Counter to the target (see the scheme of the apparatus in fig. 2.3). Considering a 200 MeV ^{16}O ion beam, like the one used in the simulation, and a distance of 30 cm between the STC and the VTX, the time t_{off} is ~ 1.8 ns. Furthermore, since the trajectory of the fragments is a curve (due to the force induced by the magnetic field), the L distance is greater than the linear distance between the target and the scintillator. A good approximation of the track length L can be obtained summing the segments l_i that connect subsequent hits left by the fragment in the detector layers, starting from the VTX up to the SCN. In this way, the eq. 3.3 becomes

$$\beta = \frac{\sum_i l_i}{c \cdot (t_{\text{STC-SCN}} - t_{\text{off}})} \quad (3.4)$$

where $t_{\text{STC-SCN}}$ is the time measurement provided by the FOOT apparatus as the diffe-

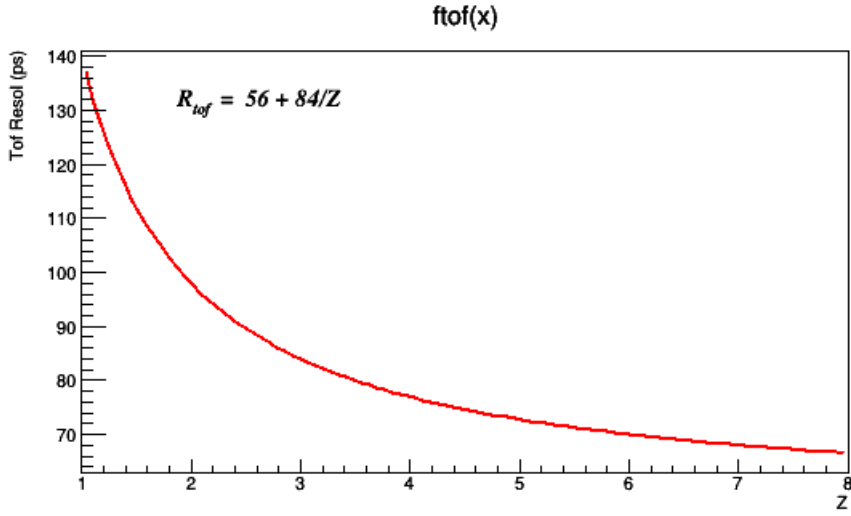


Figure 3.2: Time resolution as a function of the fragment charge.

rence between the time signal of the SCN and the time signal of the STC.

As the energy deposition, the resolution of the ToF has been evaluated at different test beams with several tipe of particle at various energy. The best approximation has been obtained by applying a Gaussian smearing with standard deviation σ_{ToF} parameterised as a function of the fragment charge Z :

$$\sigma_{\text{ToF}} = \text{Const} + \frac{\text{Slope}}{Z} \quad (3.5)$$

where $\text{Const} = 56$ ps and $\text{Slope} = 84$ ps (fig. 3.2). These values allow a time precision of about 70 ps for the heavier fragments and 140 ps for the lighter once.

Fig. 3.3 shows the charge values reconstructed in this analysis. We can clearly distinguish the peaks corresponding to the charges of the various fragments that can be generated in a reaction of ^{16}O on a C_2H_4 target. Table 3.3 shows the mean values and the resolutions obtained with a Gaussian fit of this charge distributions. The Z resolution improves with increasing fragment charge, passing from 5.7% for hydrogen to 2.7% for oxygen. A slight shift with respect the expected position is present. Actually this shift is under investigation, a possible explanation is the lack of energy due to neutron emission.

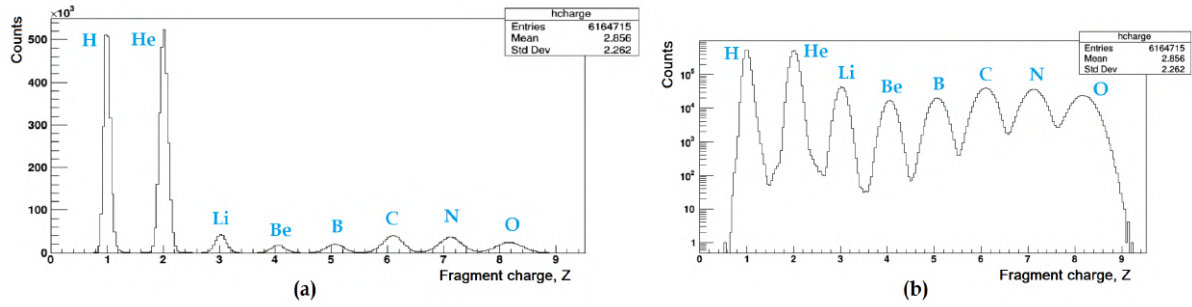


Figure 3.3: Charge number Z of fragments produced in the fragmentation in linear scale (a) and in logarithmic y scale (b). The element relating to the charge peak is indicated in blue.

Element	Charge	Mean	Standard deviation	Resolution (%)
H	1	1.01	0.06	5.7
He	2	2.01	0.07	3.7
Li	3	3.0	0.1	3.2
Be	4	4.1	0.1	3.0
B	5	5.1	0.1	2.9
C	6	6.1	0.2	2.9
N	7	7.1	0.2	2.8
O	8	8.2	0.2	2.7

Tabella 3.3: Mean values, standard deviations and resolutions of the charge distributions showed in fig. 3.3

Isotope	¹ H	⁴ He	⁷ Li	⁹ Be	¹¹ B	¹² C	¹⁴ N	¹⁶ O
Charge	1	2	3	4	5	6	7	8
Mass number	1	4	7	9	11	12	14	16

Tabella 3.4: List of the mainly produced isotopes for each charge in a fragmentation reaction induced by an oxygen-16 beam impinging on a C₂H₄ target. These isotopes have been selected to study the mass identification performance of the apparatus.

This result proves that the FOOT apparatus is perfectly able to perform the charge identification: the overlap between the Gaussian distributions in fig. 3.3 increases with the charge of the fragments but, even at high Z, the number of misidentified fragments is limited to 1-2%.

3.2 Mass identification

In order to study the mass reconstruction, the eight mainly produced isotopes, one of each charge, have been considered (tab. 3.4). An event selection has been made based on the true charge and mass (i.e. Z and A generated in the simulation), so as to be able to analyse the mass distributions of these eight types of fragments individually and evaluate the FOOT performance in the mass identification of each of them.

3.2.1 Mass reconstruction methods

The redundancy of sub-detectors in FOOT is crucial because it allows to determine the mass number A in different ways. Exploiting the relativistic momentum equation

$$p = m\beta c\gamma \quad (3.6)$$

where $\gamma = 1/\sqrt{1 - \beta^2}$, we can obtain the mass number A ($A = m/U$, where m is the mass of the fragment and $U \approx 931.5$ MeV is the Unified Atomic Mass) through the determination of the velocity ($\beta = v/c$) and the momentum p , respectively from the ToF and the tracking system, as

$$A_1 = \frac{p}{U\beta c\gamma} \quad (3.7)$$

Through the simultaneous determination of β and the kinetic energy E_k , respectively from the ToF system and the calorimeter measurements, and using the relativistic kinetic energy equation

$$E_k = mc^2(\gamma - 1) \quad (3.8)$$

we have a second method for the mass number reconstruction:

$$A_2 = \frac{E_k}{Uc^2(\gamma - 1)} \quad (3.9)$$

Through the simultaneous determination of p and E_k , respectively from the tracking system and the calorimeter, and exploiting the relativistic energy–momentum relation

$$E^2 = p^2c^2 + m^2c^4 \quad (3.10)$$

a third method is achieved:

$$A_3 = \frac{p^2c^2 - E_k^2}{2Uc^2E_k} \quad (3.11)$$

In order to obtain a slightly more precise value of the kinetic energy, the energy released by the fragment in the scintillator (ΔE) has been added to the calorimeter measurement.

The resolution of the detectors has been reproduced by applying a Gaussian smearing to all measured quantities. The same smearing described in the previous section has been applied to the ToF and ΔE , while on p and E_k a fixed resolution respectively of 4% and 1.5% has been applied. In figure 2.16 it can be seen that resolutions better than 1.5%

Quantity	Resolution
Momentum (p)	4 %
ToF	$56 ps + \frac{84 ps}{Z}$
Energy loss (ΔE)	$(4.65 + \frac{4 MeV}{\Delta E}) \%$
Kinetic energy (E_k)	1.5 %

Tabella 3.5: Resolution of the quantity measured with the simulated FOOT apparatus.

have been obtained in some tests performed on single BGO crystal bars, however, we have decided to keep this upper resolution limit, while waiting for more precise tests that will be carried out on the whole calorimeter. Tab 3.5 summarizes the resolutions applied to the measurements of momentum, energy and time.

Figures 3.4-3.6 show the mass distribution of the selected fragments obtained with the three reconstruction methods. These distributions are peaked in the expected values in the range of mass numbers between 1 and 16. Table 3.6 summarises the mean values and the resolutions obtained for each selected fragment with each reconstruction method; the precision obtained on the mass numbers obviously depends on the resolution set on ToF, p and E_k quantities.

This study aims to determine the performance of FOOT in the mass identification for each type of fragment and for each of the three reconstruction methods: the method A_1 provides the best resolution, while it is clear that the method A_3 has a significantly worse resolution than the other two. This is due to the fact that the methods A_1 and A_2 are based on the measurement of ToF, which is very precise with respect to the momentum and energy measurements on which the third method is based. Furthermore, the calculation to find the mass number, indicated by the equation 3.11, is not particularly advantageous for the propagation of error, because the quadratic terms of momentum and kinetic energy increase the associated uncertainty by a factor 2.

Another issue to consider is the fact that the resolution on the mass identification is strongly dependent both on the energy loss by fragments due to ionization processes before reaching the calorimeter and the leakage inside it, which is mostly due to neutron emission. In fig 3.7 one can see, for each selected fragment, the distribution of the ratio between the measured kinetic energy (energy deposition in the scintillator and in the

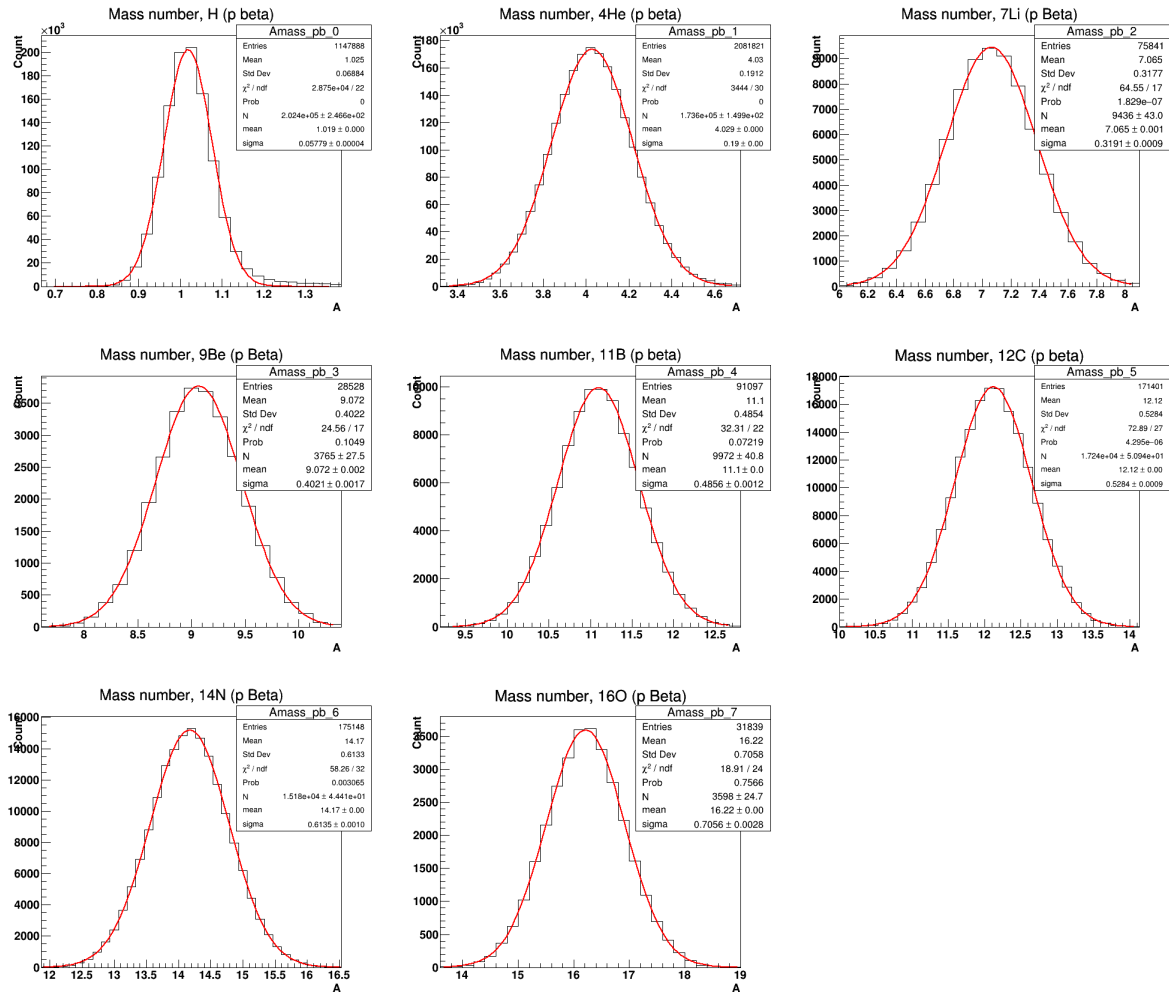


Figure 3.4: Mass numbers A_1 from 1 to 16 reconstructed with the ToF and momentum measurement.

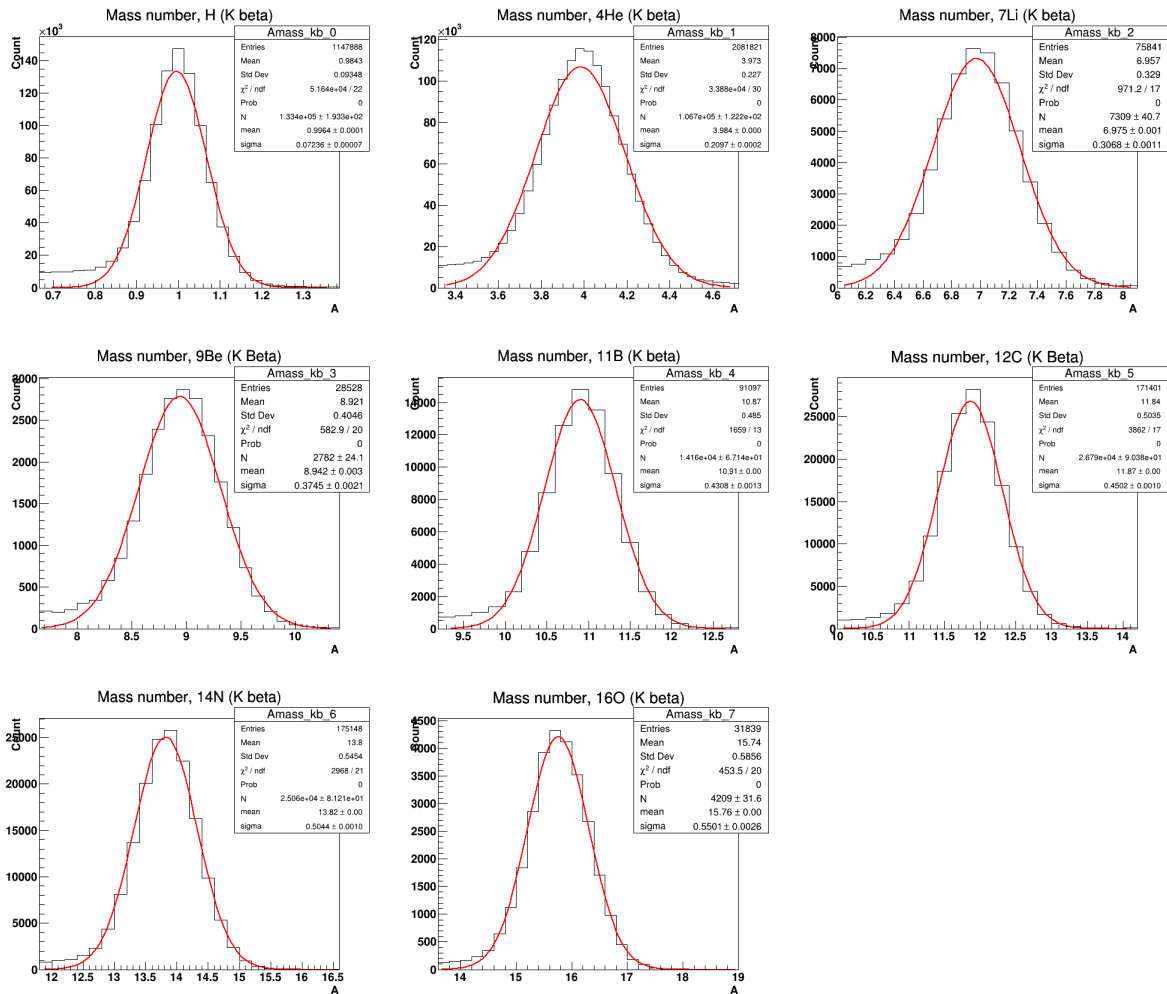


Figure 3.5: Mass numbers A_2 from 1 to 16 reconstructed with the kinetic energy and momentum measurement.

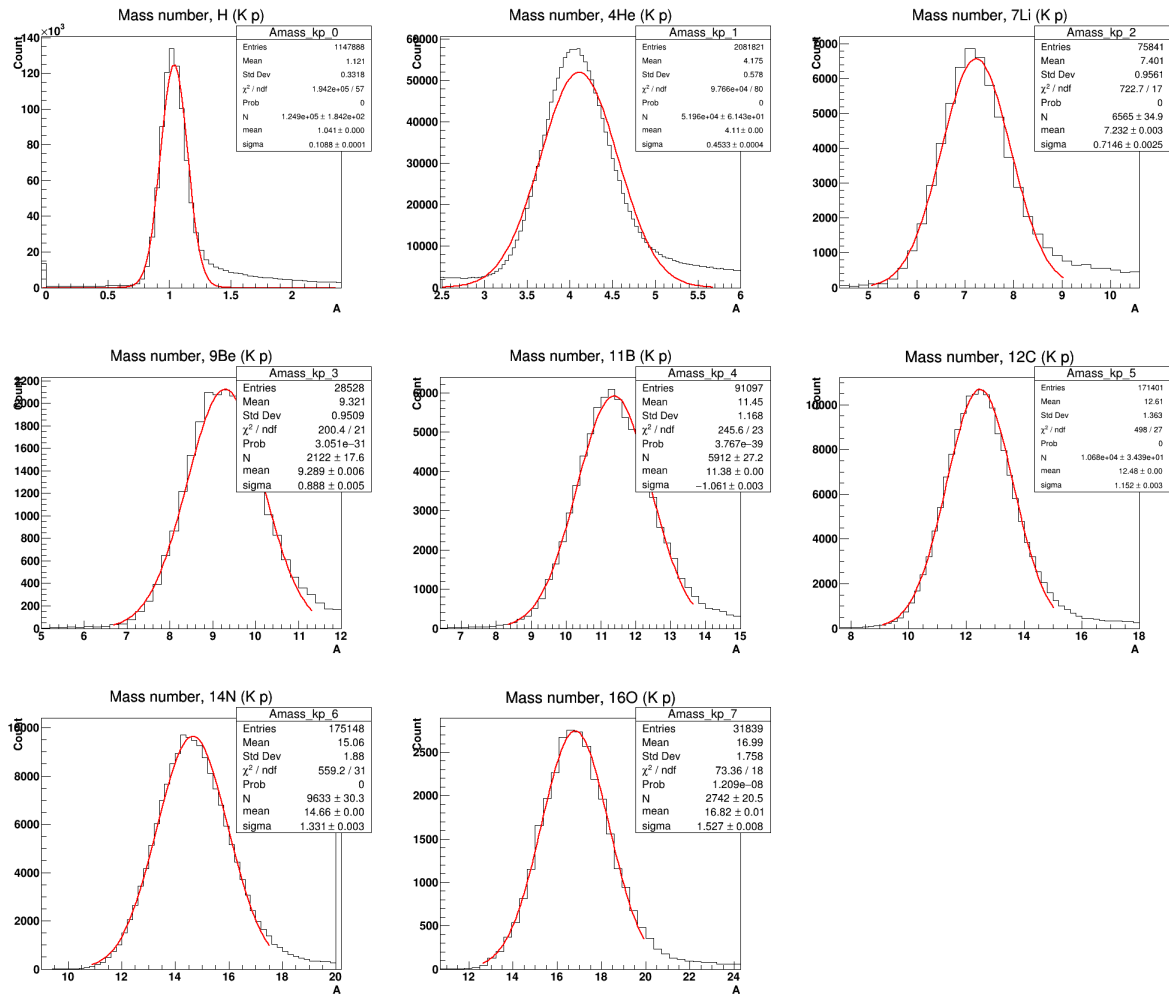


Figure 3.6: Mass numbers A_3 from 1 to 16 reconstructed with the ToF and kinetic energy.

Isotope	A₁ Mean	A₁ Standard deviation	A₁ Resolution (%)
¹ H	1.02	0.06	5.74
⁴ He	4.03	0.19	4.72
⁷ Li	7.07	0.32	4.52
⁹ Be	9.07	0.40	4.43
¹¹ B	11.10	0.49	4.37
¹² C	12.12	0.53	4.36
¹⁴ N	14.17	0.61	4.33
¹⁶ O	16.22	0.71	4.35
isotope	A₂ Mean	A₂ Standard deviation	A₁ Resolution (%)
¹ H	1.00	0.07	7.26
⁴ He	3.98	0.21	5.26
⁷ Li	6.98	0.31	4.40
⁹ Be	8.94	0.37	4.19
¹¹ B	10.91	0.43	3.95
¹² C	11.87	0.45	3.79
¹⁴ N	13.82	0.50	3.65
¹⁶ O	15.76	0.55	3.49
isotope	A₃ Mean	A₃ Standard deviation	A₁ Resolution (%)
¹ H	1.04	0.11	10.45
⁴ He	4.11	0.45	11.03
⁷ Li	7.23	0.71	9.88
⁹ Be	9.29	0.89	9.56
¹¹ B	11.38	1.06	9.32
¹² C	12.48	1.15	9.23
¹⁴ N	14.66	1.33	9.08
¹⁶ O	16.82	1.53	9.10

Tabella 3.6: Mean values, standard deviations and resolutions of the mass number distributions obtained with the three methods (A₁, A₂, A₃) discussed in section 3.2.1

calorimeter) and the generated kinetic energy: a not negligible amount of events belongs to the tail in which the deposited energy is less than 90 % of the generated kinetic energy. These tails have consequence on the mass number reconstructed with the two methods that involves the kinetic energy measurement, in fact, in the plots in fig. 3.5 and 3.6, tails of events with much lower (in the case of A_2) and much higher (in the case of A_3) mass are visible. The final resolution on the A determination is also affected by the shift of the peak position also shown fig. 3.7. This shift is due to the overall energy loss in the detector materials and it is fragment dependent. In the final configuration, the problem will be fixed with an appropriate energy calibration of both the plastic scintillator and the calorimeter, at the moment not yet applied.

3.2.2 χ^2 and ALM fit

The strategy used for the best determination of A consists of a fit procedure that combines all the three measured quantities at the same time. The standard approach uses a minimization method of the χ^2 -function:

$$\chi^2 = \left(\frac{ToF - T}{\sigma_{ToF}} \right)^2 + \left(\frac{p - P}{\sigma_p} \right)^2 + \left(\frac{E_k - K}{\sigma_{E_k}} \right)^2 + \quad (3.12)$$

$$(A_1 - A, \quad A_2 - A, \quad A_3 - A) \begin{pmatrix} B_{00} & B_{01} & B_{02} \\ B_{00} & B_{01} & B_{02} \\ B_{00} & B_{01} & B_{02} \end{pmatrix} \begin{pmatrix} A_1 - A \\ A_1 - A \\ A_1 - A \end{pmatrix}$$

where ToF , p , E_k , A_1 , A_2 and A_3 are the reconstructed quantities, σ_{ToF} , σ_p , σ_{E_k} are the uncertainties derived from the resolutions applied with the smearing procedure and T , P , K and A are the output parameters of the fit.

The uncertainties associated to A_1 , A_2 and A_3 has been evaluated taking into account their correlation generically expressed by the matrix B , which is related to the correlation matrix C by the relation $B = (C \cdot C^T)^{-1}$, where C is expressed as

$$C = \begin{pmatrix} \frac{\partial A_1}{\partial T} dT & \frac{\partial A_1}{\partial P} dP & 0 \\ \frac{\partial A_2}{\partial T} dT & 0 & \frac{\partial A_2}{\partial K} dK \\ 0 & \frac{\partial A_3}{\partial P} dP & \frac{\partial A_3}{\partial K} dK \end{pmatrix} \quad (3.13)$$

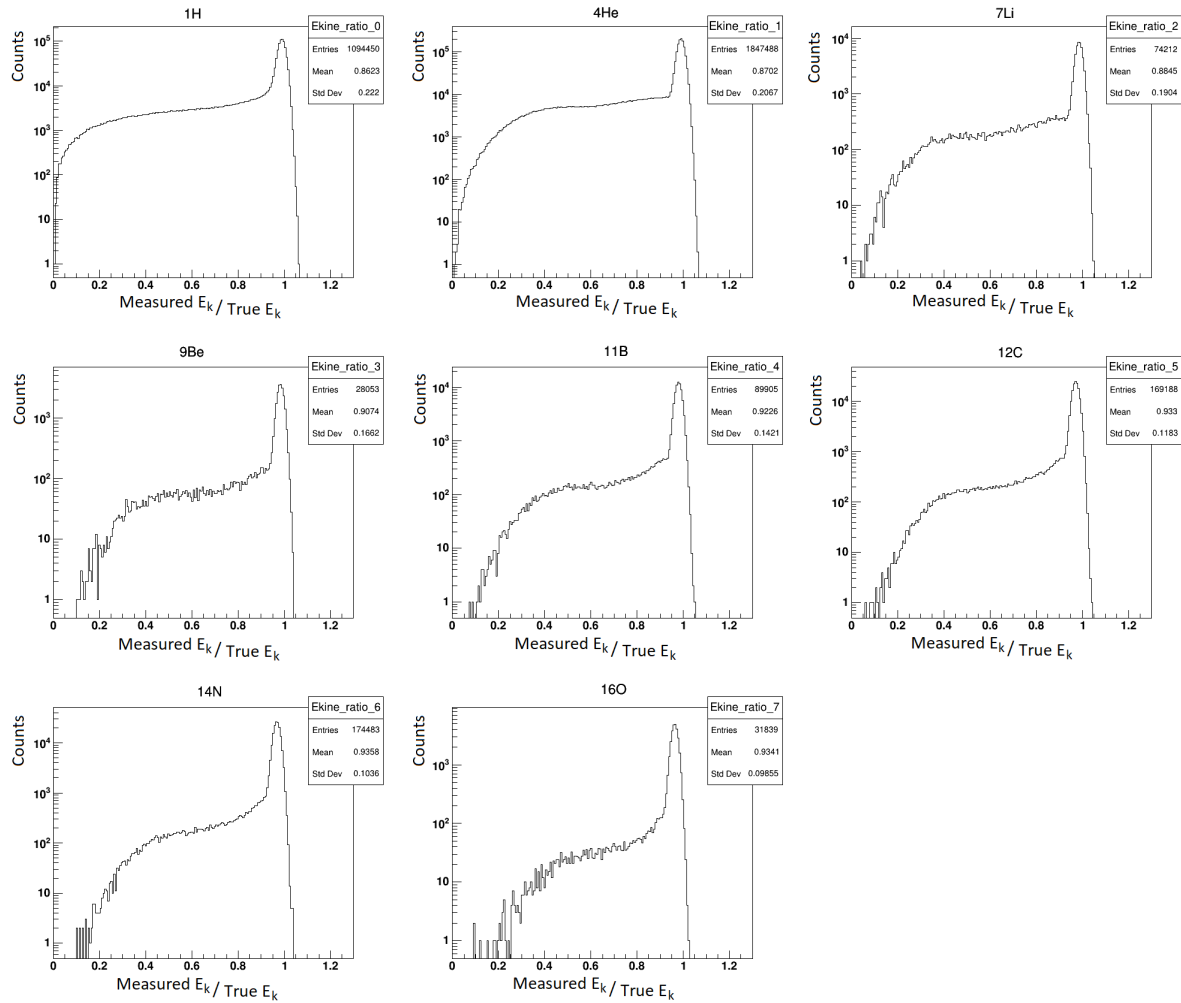


Figure 3.7: Distribution of the ratio between the measured kinetic energy (energy deposition in the scintillator plus energy deposition in the calorimeter) and the true kinetic energy (generated in the simulation) of the fragments produced in the fragmentation reaction $^{16}\text{O} + \text{C}_2\text{H}_4$.

The mass number A distributions obtained with the standard χ^2 method for all the selected fragments are presented in fig. 3.8. Further distributions have been obtained with the χ^2 -fit method by applying a cut on the χ^2 value: only the events reconstructed with $\chi^2 < 5$ have been selected; the resulting plots are shown in fig. 3.9. This cut does not significantly improve the resolution, but it allows to exclude those events that are badly reconstructed, which belong to the tails of the distributions visible in fig. 3.8. Cutting these tails is important for the mass identification in real data analysis, as they affect the mass distributions of the isotopes in the neighboring mass values. Table 3.7 shows the mean values and resolutions of the distributions obtained with the χ^2 -fit method (with and without cut).

The resolutions obtained with the various methods of mass reconstruction are compared in fig. 3.10. It can be seen that the best resolution on the mass number can be achieved by combining all the three methods in the χ^2 -fit and applying the $\chi^2 < 5$ selection. We conclude that it is possible to obtain a mass resolution between 3 and 4 % for heavy fragments.

Another minimization approach has been performed, consisting of an Augmented Lagrangian Method (ALM) as described in details in [88]. The procedure minimizes a Lagrangian function L expressed by

$$L(\vec{x}, \lambda, \mu) = f(\vec{x}) - \sum_a \lambda_a c_a(\vec{x}) + \frac{1}{2\mu} \sum_a c_a^2(\vec{x}) \quad (3.14)$$

where f , in analogy with the standard χ^2 method, is defined as:

$$f(\vec{x}) = \left(\frac{ToF - T}{\sigma_{ToF}} \right)^2 + \left(\frac{p - P}{\sigma_p} \right)^2 + \left(\frac{E_k - K}{\sigma_{E_k}} \right)^2 \quad (3.15)$$

The summations on the number of constraints a (3 in this case) can be expressed as

$$\sum_a \lambda_a c_a(\vec{x}) = \lambda_1(A_1 - A) + \lambda_2(A_2 - A) + \lambda_3(A_3 - A) \quad (3.16)$$

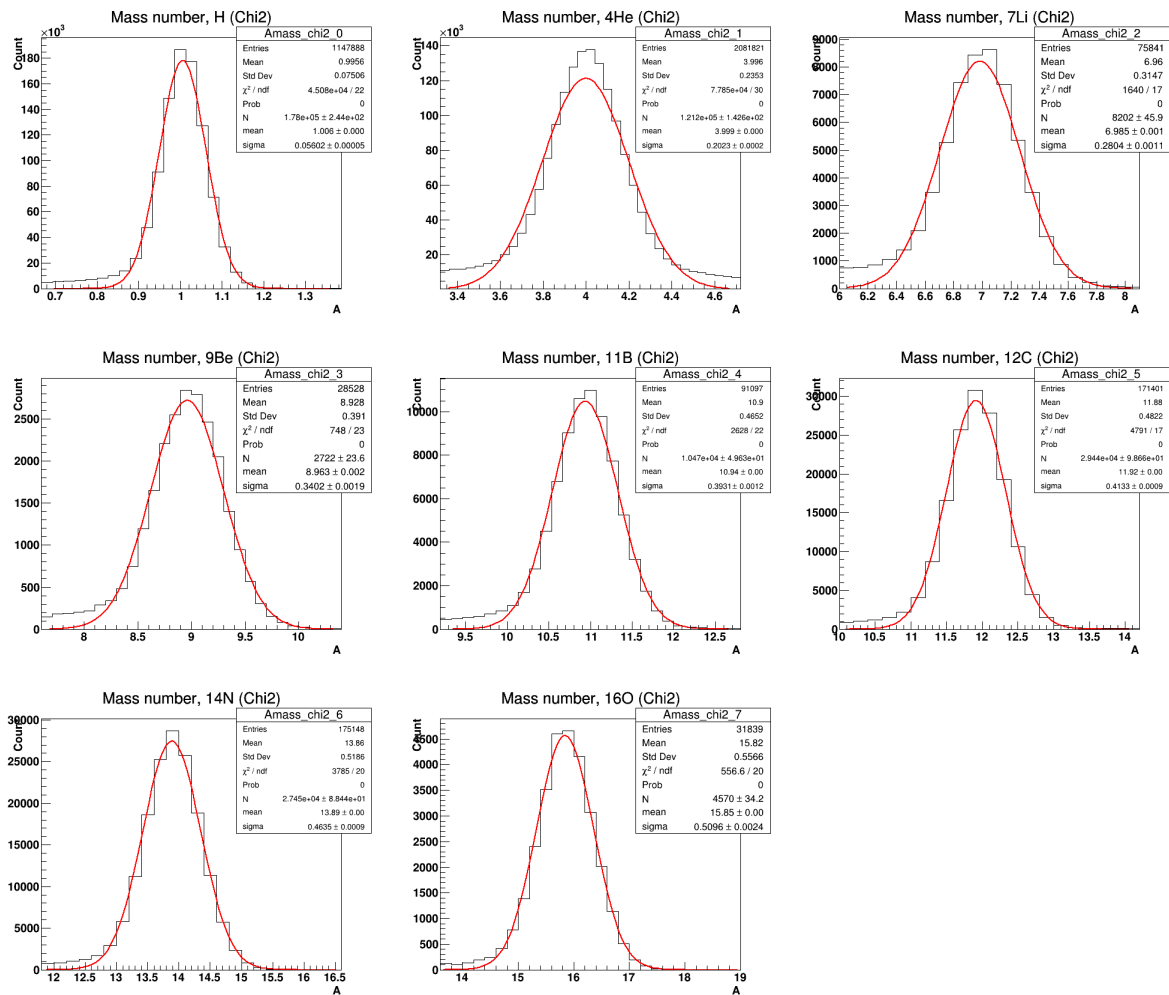


Figure 3.8: Mass numbers distributions obtained with the standard χ^2 minimization method.

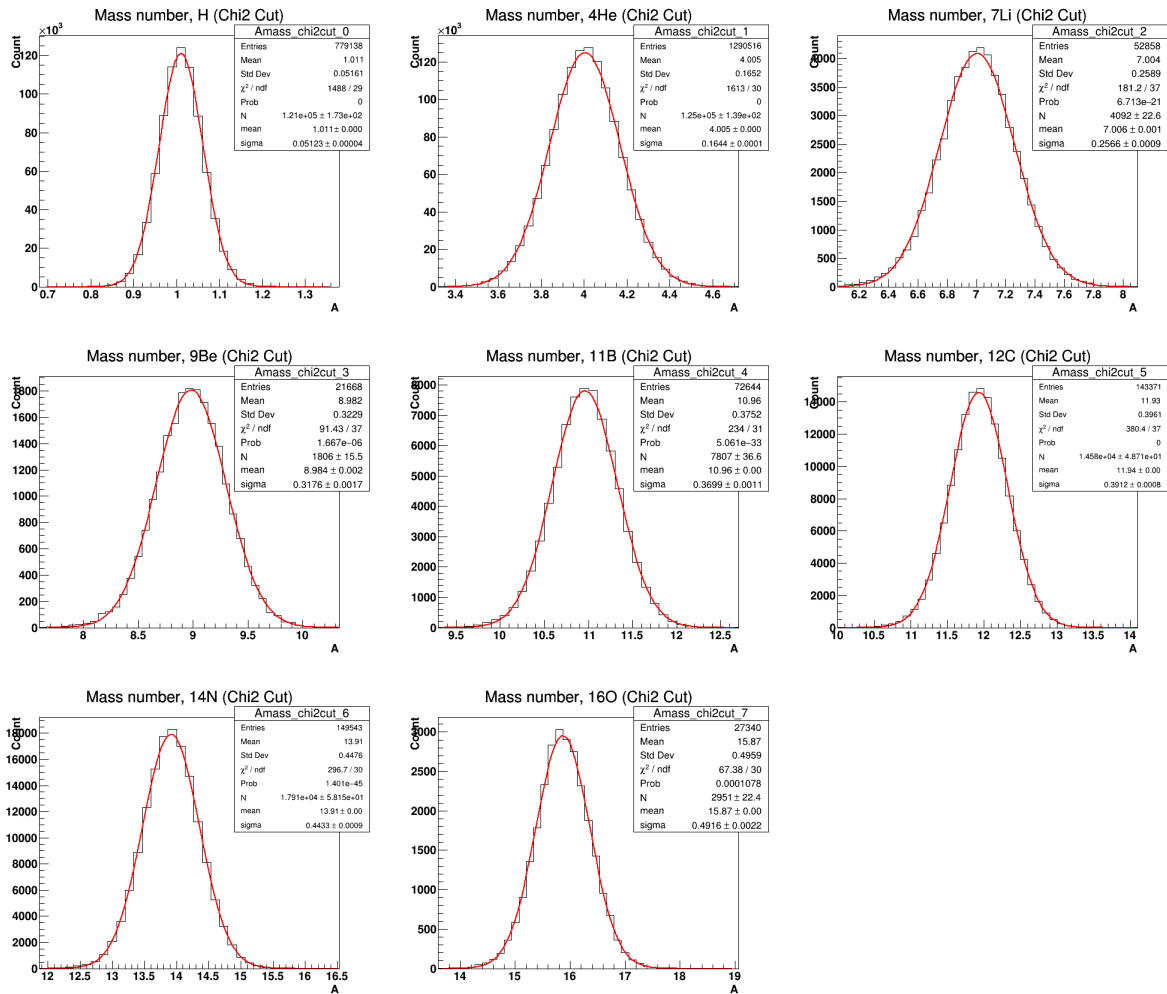


Figure 3.9: Cutted distributions ($\chi^2 < 5$ events only) of the mass number obtained with the standard χ^2 minimization method.

Fragment	A_{χ^2} Mean	A_{χ^2} Standard deviation	A_{χ^2} Resolution (%)
^1H	1.01	0.06	5.57
^4He	4.00	0.20	5.06
^7Li	6.99	0.28	4.01
^9Be	8.96	0.34	3.80
^{11}B	10.94	0.39	3.59
^{12}C	11.92	0.41	3.47
^{14}N	13.89	0.46	3.34
^{16}O	15.85	0.51	3.22
Fragment	A_{χ^2} (cut) Mean	A_{χ^2} (cut) Standard deviation	A_{χ^2} (cut) Resolution (%)
^1H	1.01	0.05	5.07
^4He	4.01	0.16	4.10
^7Li	7.01	0.26	3.66
^9Be	8.98	0.32	3.54
^{11}B	10.96	0.37	3.38
^{12}C	11.94	0.39	3.28
^{14}N	13.91	0.44	3.19
^{16}O	15.87	0.49	3.10

Tabella 3.7: Mean values, standard deviations and resolutions of the mass number distributions obtained with the standard χ^2 -fit method (top table) and with the application of the $\chi^2 < 5$ selection (bottom table).

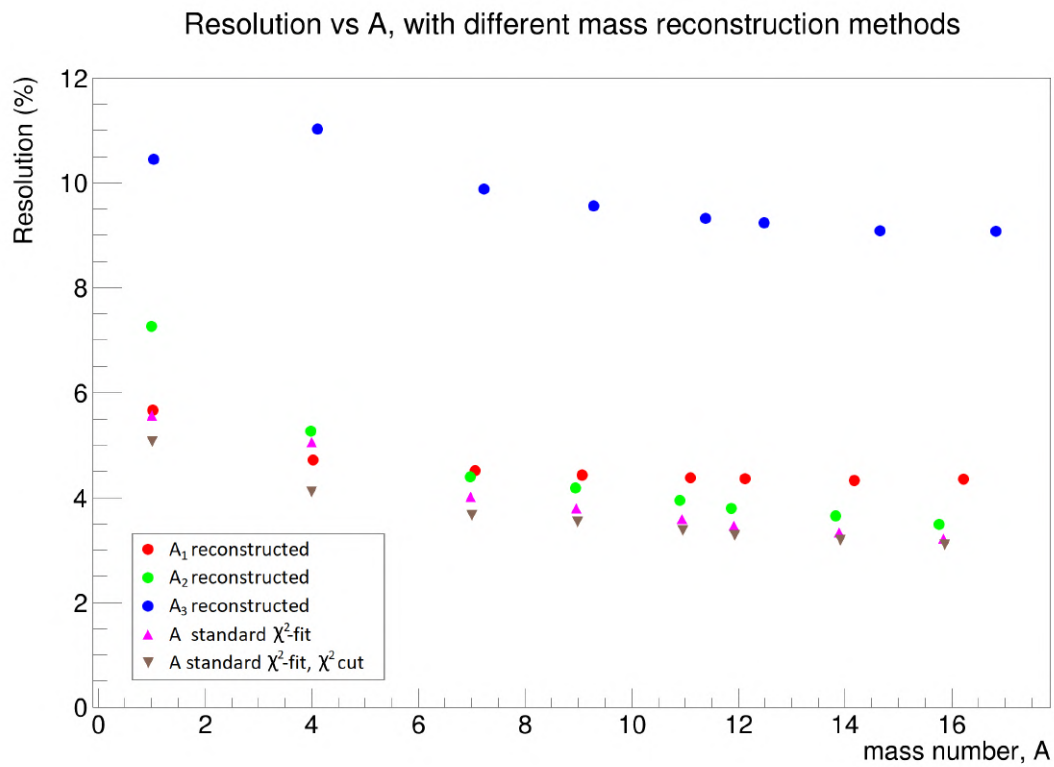


Figure 3.10: Mass resolution as a function of the mass number obtained with different mass reconstruction methods.

$$\frac{1}{2\mu} \sum_a c_a^2(\vec{x}) = \frac{1}{2\mu} \left((A_1 - A)^2 + (A_2 - A)^2 + (A_3 - A)^2 \right) \quad (3.17)$$

where λ are Lagrange multiplier parameters and μ is the penalty term fixed to 0.1. The use of a penalty term forces the fit to give more strength to the constraints: the lower is μ the greater is the effect of the constraints.

The results obtained with this method show a comparable resolution with respect to the χ^2 -fit, for this reason the previous method has been chosen for the cross section analysis.

3.3 Cross section calculation

After the charge and mass identification has been carried out, it has been possible to calculate the differential cross section with respect the kinetic energy for the production of a type of fragment F by determining its yield $Y_F(E)$, i.e. the number of detected fragments F with kinetic energy per nucleon E (appendix A). More precisely, the energy differential cross section can be calculated as follows:

$$\frac{d\sigma_F}{dE} = \frac{(Y_F(E) - B_F(E))^u}{N_{\text{prim}} \cdot N_t \cdot \Omega_E \cdot \epsilon_F(E)} \quad (3.18)$$

where F indicates the F -th fragment characterized by the reconstructed Z and A values, $B_F(E)$ is the background component due to fragment mis-identification, N_{prim} is the number of primary particles of the beam crossing the target, N_t is the number of particles per unit surface of the target, Ω_E is the energy phase space, ϵ is the reconstruction efficiency and u indicates that the quantities inside the brackets have to be "unfolded", as discussed in section 3.3.2, in order to eliminate the distortions included by the detector.

The value of N_t is given by

$$N_t = \frac{\rho N_A d}{A} \quad (3.19)$$

where ρ is the target density, N_A is the Avogadro's number, d is the target thickness

Energy range, i	E_i^{\min} (MeV)	E_i^{\max} (MeV)
1	120	173
2	173	179
3	179	184
4	184	188
5	188	192
6	192	198
7	198	225

Tabella 3.8: Energy ranges within which the energy differential cross section has been calculated.

(depth along the z -axis) and A is the mass number of the target. In the case of a non-single element target, the mass number is given by the sum of the mass numbers of the atoms that compose the molecule of the compound. Considering a C_2H_4 target, the mass number is

$$A_{C_2H_4} = 2A_C + 4A_H = 28.052 \quad (3.20)$$

Y_F , B_F and ϵ are continuous functions of energy, however, for obvious reasons, the differential cross section has to be calculated in discrete energy steps. In the presented analysis, the quantities needed in eq. 3.18 have been evaluated in seven contiguous kinetic energy ranges (tab 3.8). Below we will indicate with a subscript " i " the quantities that refers to the i -th energy range. For example, we will indicate with $Y_{F,i}$ the yield of the type F fragment in the energy range i .

The phase space is defined as

$$\Omega_i = E_i^{\max} - E_i^{\min} \quad (3.21)$$

where E_i^{\max} and E_i^{\min} are the limits of the production energy of the fragments within which the yield is evaluated, i.e. the extremes of the i -th energy range.

In this thesis only the differential cross sections of carbon fragments have been evaluated. This choice is due to the fact that carbon produces the highest number of isotopes

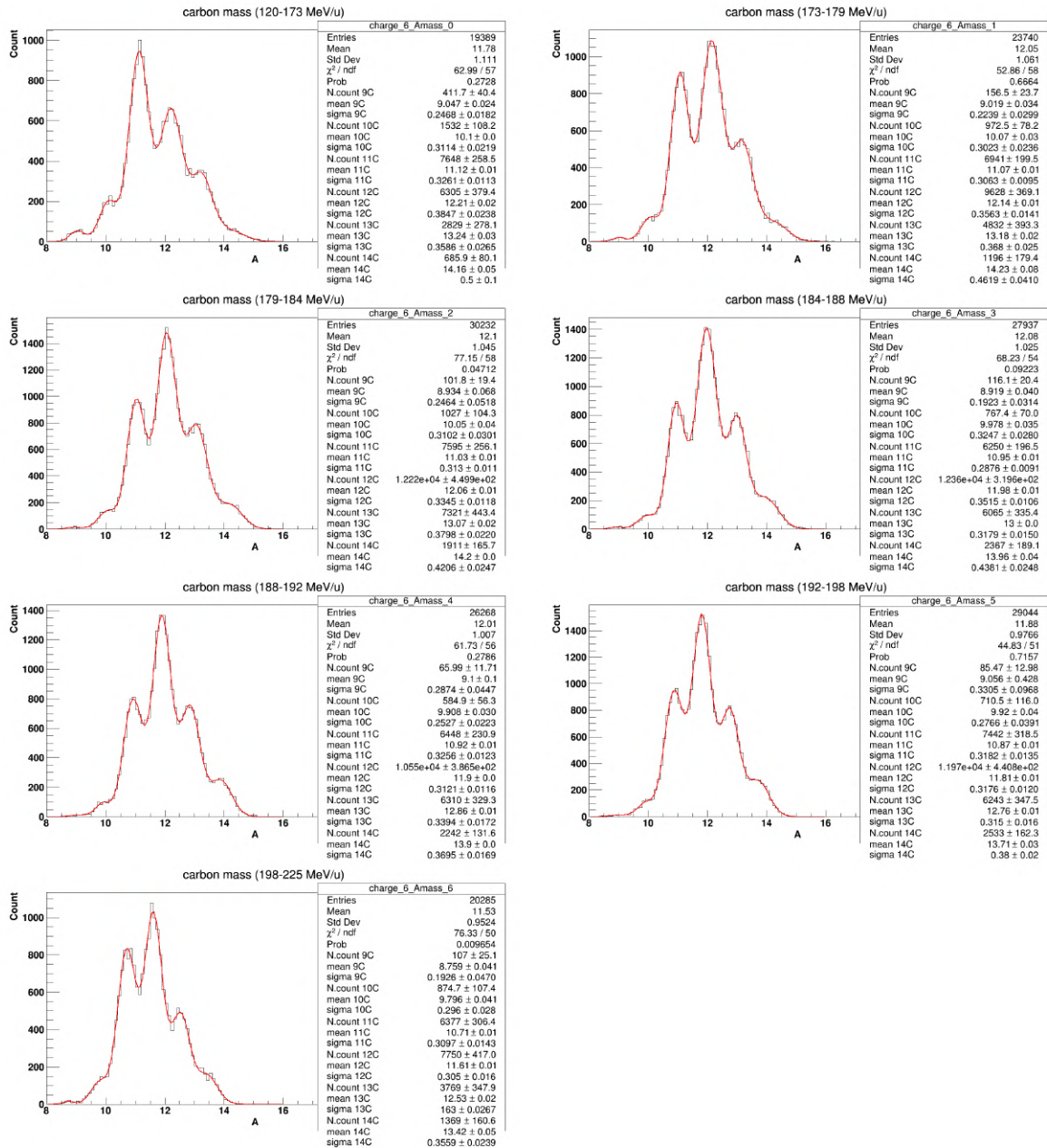


Figura 3.11: Mass number of carbon fragments in different kinetic energy range.

(six isotopes, whose mass number ranges between 9 and 14) and, consequently, it is the most difficult to analyse.

First of all, the fragments have been selected based on the reconstructed charge: since the values of the various charges are at a distance 1 from each other, a fragment has been included in the analysis if its reconstructed charge was in the range $[\mu_Z - 0.5, \mu_Z + 0.5]$, where μ_Z is the mean of the charge distribution of that fragment (fig. 3.3). Therefore, in order to select only carbon fragments, the reconstructed charge has been requested to be between 5.6 and 6.6.

Then, the selected fragments of charge 6 have been divided according to their reconstructed kinetic energy and distributions of their mass number (obtained with the χ^2 -fit and the same cut as described in section 3.2.2) have been built. Figure 3.11 shows the carbon fragments in each considered energy range: the observable peaks represent the various carbon isotopes that can be generated in the fragmentation. To obtain the number of each produced isotope ($Y_{F,i}$), a fit consisting of the sum of six Gaussian functions (one for each isotope) has been applied to each distribution. The counts underlying the peaks, i.e. the number of produced fragments of the corresponding isotopes ($Y_{F,i}$), has been extrapolated from the output parameters of this fit.

3.3.1 Background evaluation

Once the number of each carbon isotope has been counted in each energy range, it is necessary to determine the background component. It has been evaluated that the highest background contribution derives from wrong mass number identification. In this case the simulation is an excellent tool, since it allows us to know the true characteristics of the particle (such as charge, mass and energy), allowing us to make an easy comparison with the reconstructed quantities.

In order to evaluate this background contribution, 2D Migration histograms has been created, with on the x axis the reconstructed mass number and on the y axis the true mass number generated in the simulation (Fig. 3.12). The entries in the bins standing on the bisector represent the number of fragment well reconstructed, while the entries in the bins standing above or under this line represent the number of bad identified fragments. Calling T_A the sum of the entries of all the bins on the vertical line $x = A$

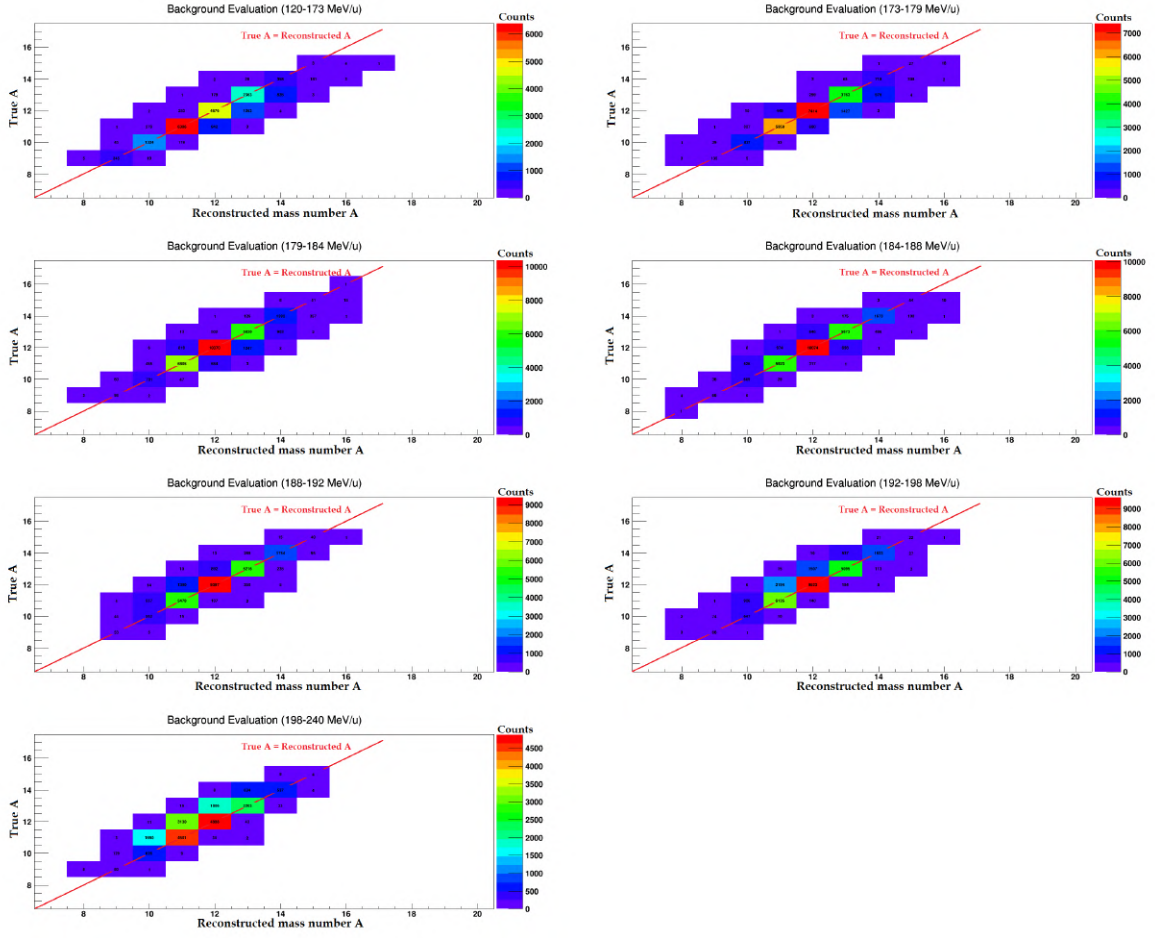


Figure 3.12: Migration histograms for the background evaluation of carbon fragments in different kinetic energy ranges.

(total fragments with reconstructed mass number A) and W_A the number of entries in the bin $x = y = A$ (number of well reconstructed fragments with mass number A), the background fraction R_A for the fragment with reconstructed mass number A can be calculated in the following way:

$$R_A = 1 - \frac{W_A}{T_A} \quad (3.22)$$

Thus, the number of background events $B_{F,i}$ can be obtained by multiplying the yield $Y_{F,i}$ by the background fraction obtained for the fragment F in the energy range i .

Figure 3.13 shows the production yields and their background components, while figure 3.14 shows the production yields with background subtraction as a function of kinetic energy.

3.3.2 Unfolding

The quantities $(Y_{F,i} - B_{F,i})$ found at this points, suffer from another factor of uncertainty: because of the finite resolution of the apparatus, the measured kinetic energy can differ from the true one, thus falling, in some cases, in an incorrect bin of the measured energy spectrum. This effect brings to a distortion in the reconstructed distributions, which depends on the specific detector employed in the experiment.

In order to make these distortions independent of the detector, an *unfolding* procedure has to be applied to the measured distribution Y . In this way, we can obtain the true distribution X that we would have in the case of a detector with infinite precision. The unfolding procedure involves the construction of a correction matrix A , which correlates the true and the measured distributions (reconstructed yields background subtracted as a function of the kinetic energy):

$$AX = Y \quad (3.23)$$

In the MC data analysis, the correction matrix can be obtained in a similar way to the evaluation of the background: for each carbon isotope, a migration plot has been made, with on the x axis the measured kinetic energy of the produced fragment and on the y axis the true kinetic energy, generated in the simulation (fig. 3.15). These plots represent the matrix A , in which the element A_{jk} is given by the counts inside the bin of the j -th row and k -th column.

The relation 3.23 must be inverted, in order to obtain the true distribution from the measured one:

$$X = A^{-1}Y \quad (3.24)$$

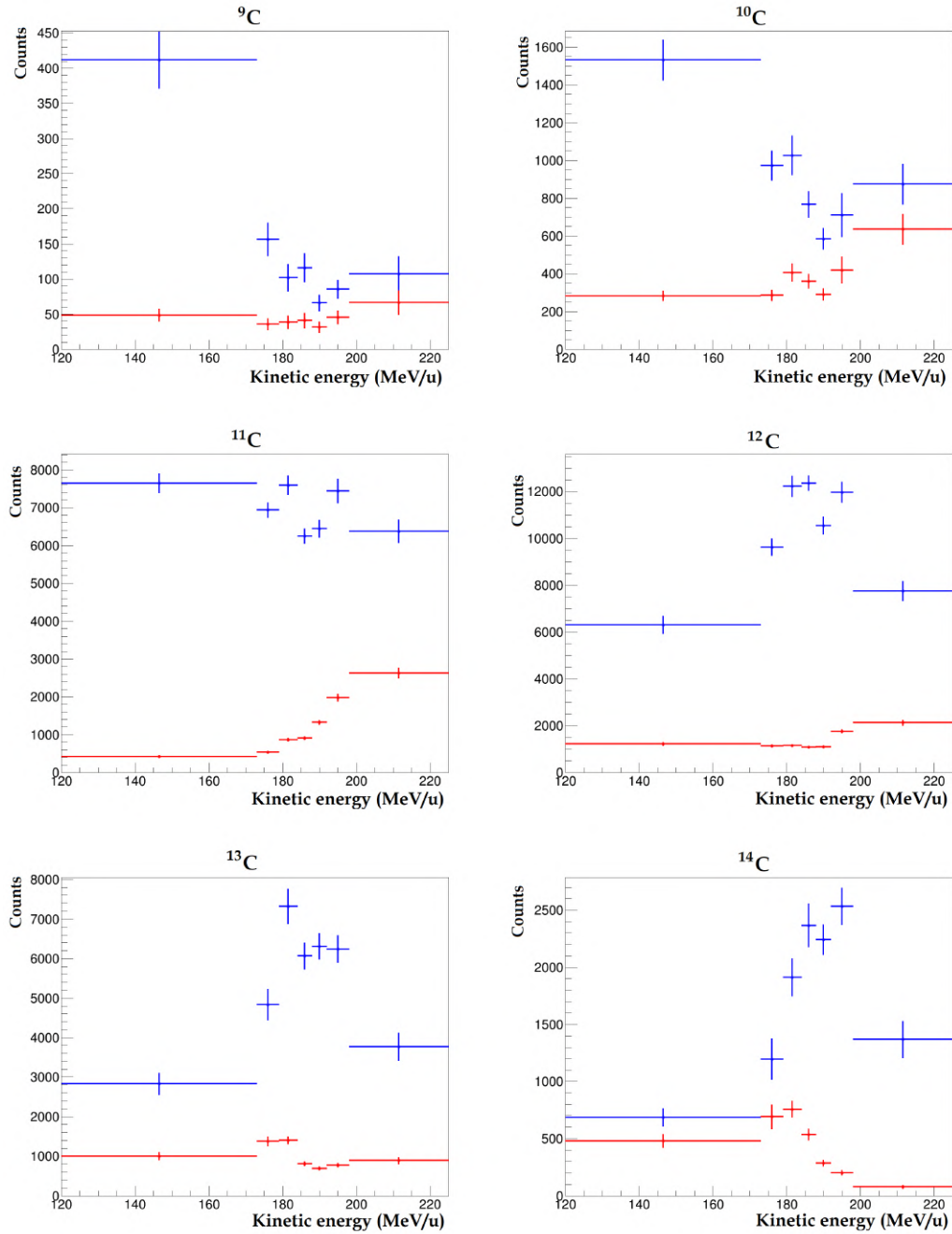


Figure 3.13: Production yields (blue lines) and background events (red lines) as a function of kinetic energy of carbon isotopes.

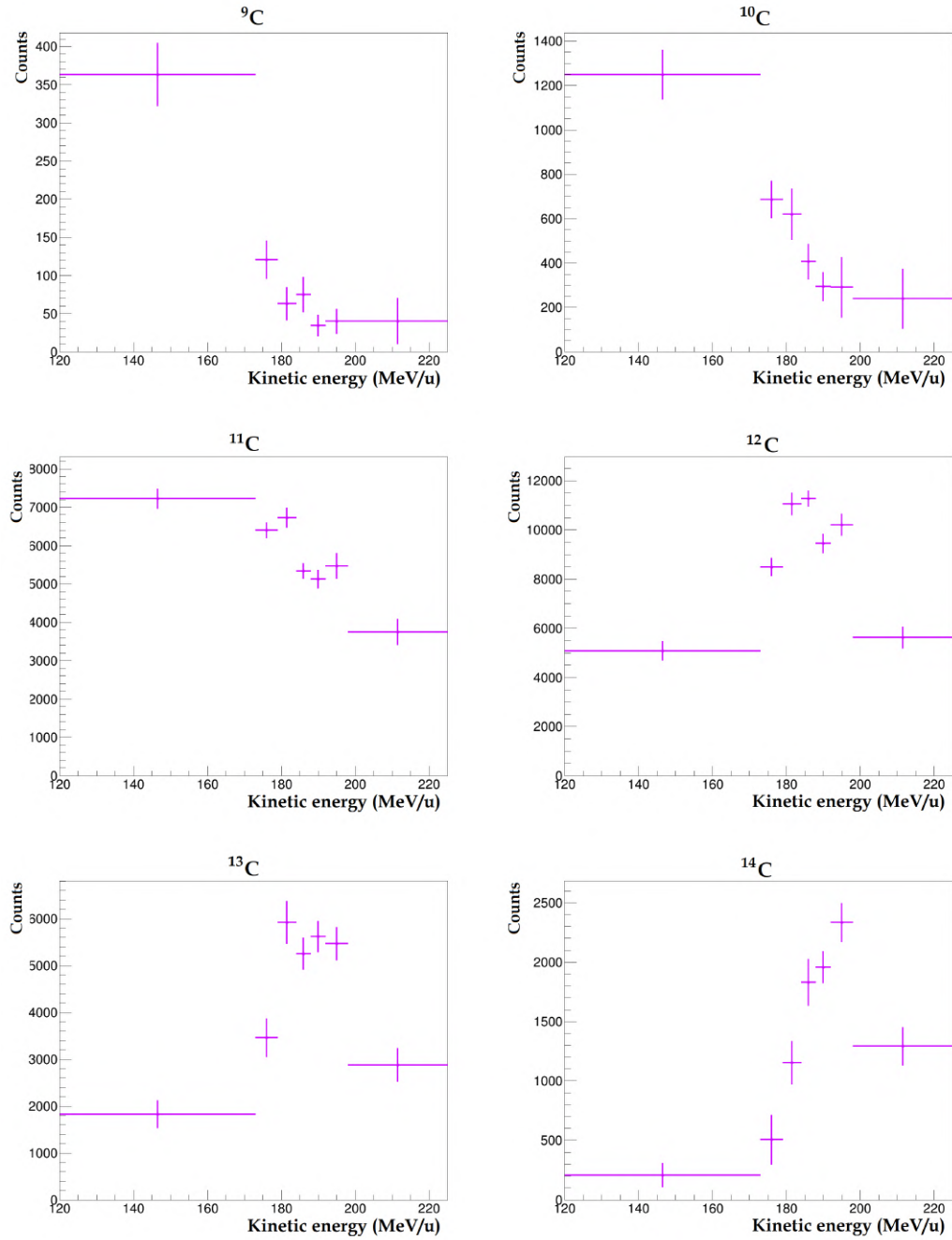


Figure 3.14: Production yields background subtracted as a function of kinetic energy of carbon isotopes.

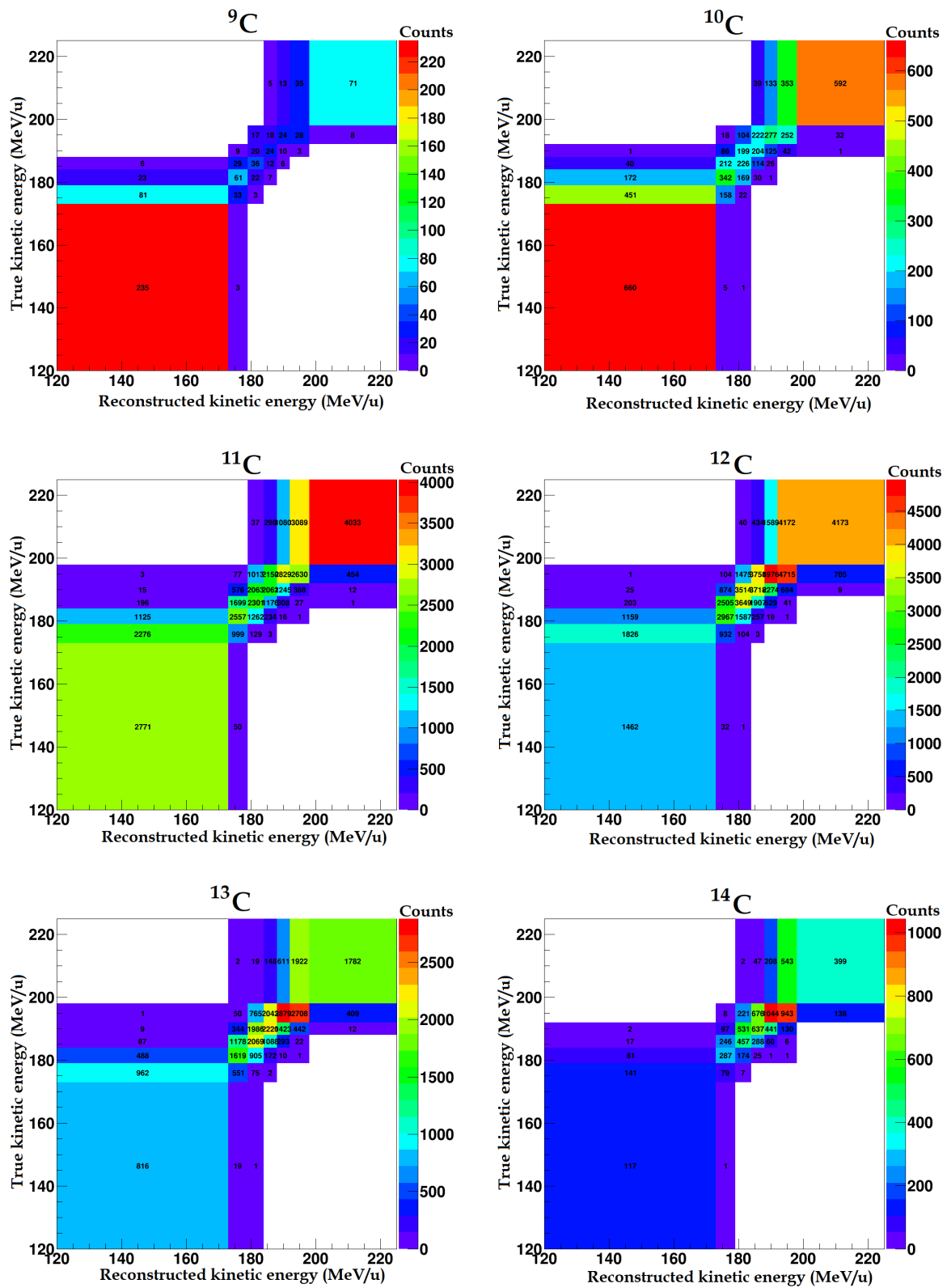


Figure 3.15: Migration histograms of kinetic energy used in the unfolding procedure.

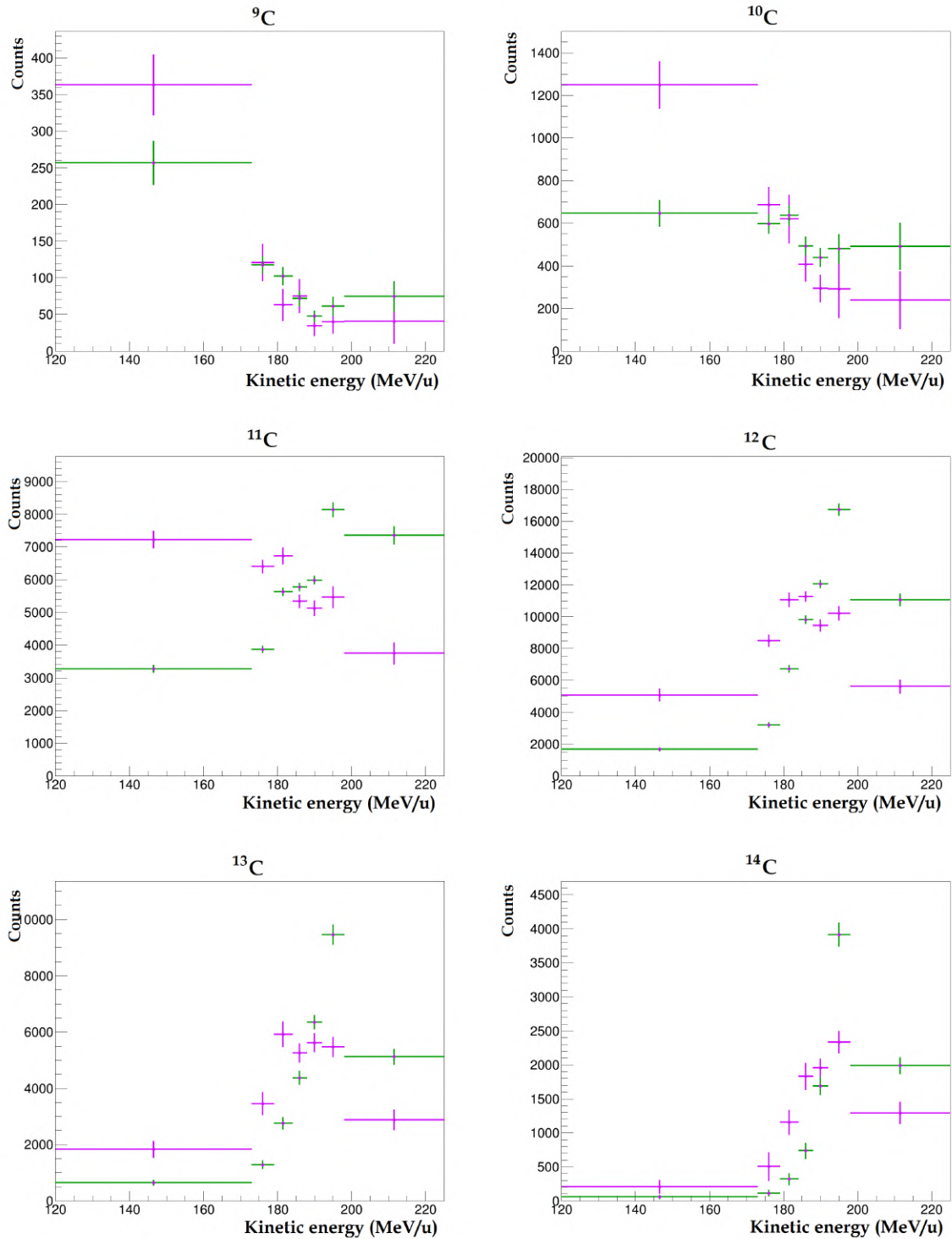


Figure 3.16: Distributions of yields background subtracted (violet) and unfolded distributions (green) with respect to kinetic energy of carbon isotopes.

The procedure to invert the matrix A requires the use of advanced and robust statistics methods; the approach used in this case is the *Singular Value Decomposition* (SVD) [89, 90]. Fig. 3.16 shows a comparison between the yields (background subtracted) obtained before and after the unfolding procedure.

3.3.3 Efficiency

For each fragment type F and each kinetic energy range i , an evaluation of the overall efficiency ($\epsilon_{F,i}$) has been made by comparing the true number of fragments generated in the MC simulation ($N_{F,i}^{\text{gen}}$) with the number of fragments reconstructed and selected with the analysis software ($N_{F,i}^{\text{sel}}$):

$$\epsilon_F = \frac{N_{F,i}^{\text{sel}}}{N_{F,i}^{\text{gen}}} \quad (3.25)$$

Both $N_{F,i}^{\text{sel}}$ and $N_{F,i}^{\text{gen}}$ have been evaluated on the second group of events (those that have been actually treated as MC events): $N_{F,i}^{\text{sel}}$ has been determined by applying to the reconstructed fragments the same selections used to obtain the yields from the first group of events; $N_{F,i}^{\text{gen}}$ has been determined by selecting all the fragments F produced within the target in the i -th kinetic energy range. The obtained efficiencies as a function of kinetic energy are shown in figure 3.17.

3.3.4 Fragmentation cross sections and FLUKA cross sections comparison

Having obtained all the terms of the equation 3.18, it has been possible to calculate the differential cross with respect to kinetic energy relating to a 200 MeV/u ^{16}O beam impinging on a C_2H_4 target. Table 3.9 and figure 3.18 show the results obtained for the six carbon isotopes produced in the simulated fragmentation processes.

Another analysis has been performed using a second MC simulation running 5×10^7 events of ^{16}O (200 MeV/u) impinging on a C target. The procedure is the same as the one described so far in this chapter and the results on the energy differential cross sections

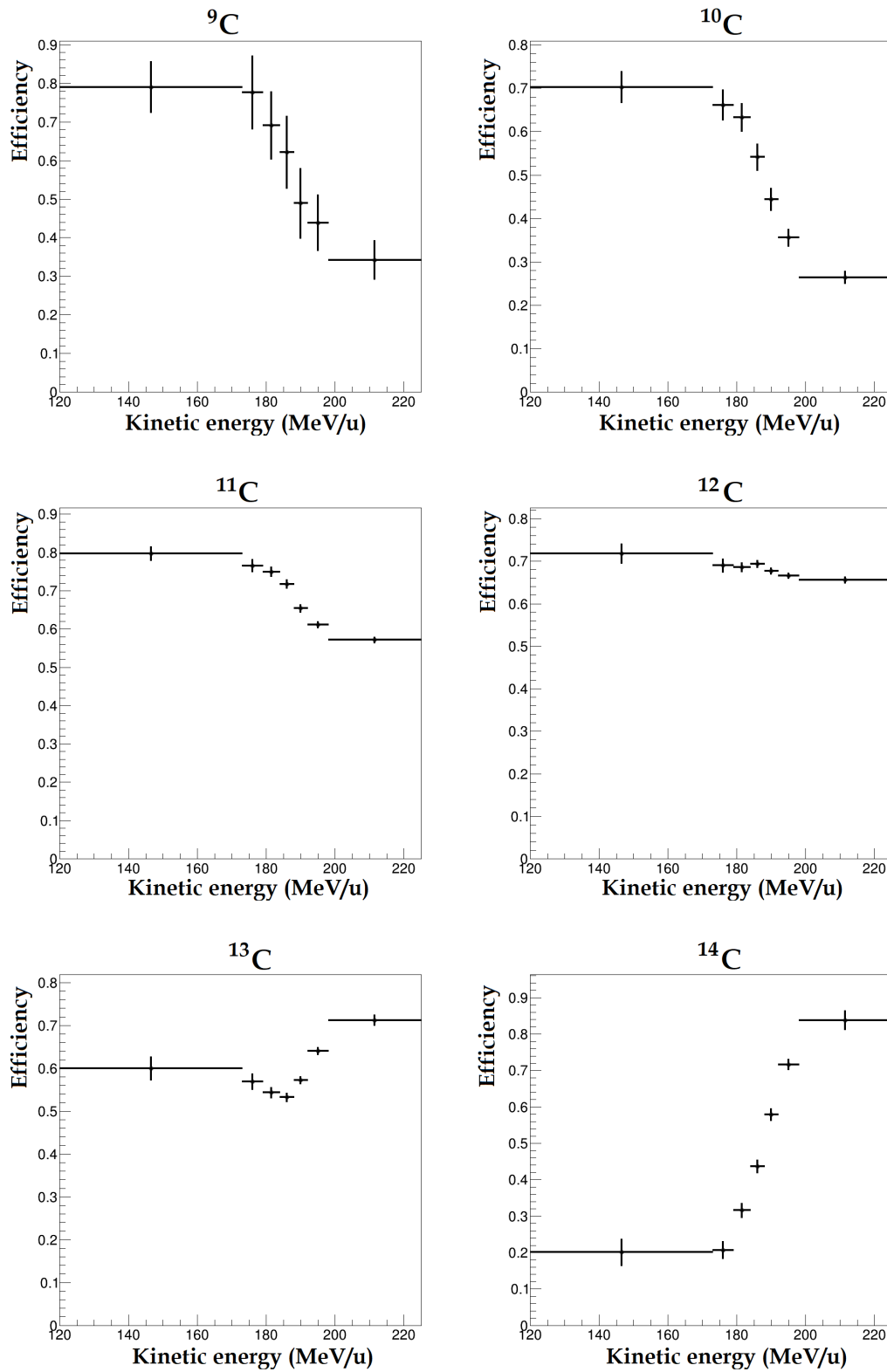


Figure 3.17: Reconstruction efficiency as a function of kinetic energy of each carbon isotope.

Energy range (MeV/u)	^9C	^{10}C	^{11}C
120-173	0.012 ± 0.002	0.034 ± 0.004	0.154 ± 0.007
173-179	0.05 ± 0.008	0.30 ± 0.03	1.67 ± 0.06
179-184	0.06 ± 0.01	0.40 ± 0.04	2.98 ± 0.08
184-188	0.06 ± 0.01	0.45 ± 0.05	4.0 ± 0.1
188-192	0.05 ± 0.01	0.49 ± 0.06	4.5 ± 0.1
192-198	0.05 ± 0.01	0.45 ± 0.07	4.4 ± 0.1
198-225	0.016 ± 0.005	0.14 ± 0.03	0.94 ± 0.04
Energy range (MeV/u)	^{12}C	^{13}C	^{14}C
120-173	0.087 ± 0.006	0.040 ± 0.006	0.011 ± 0.006
173-179	1.54 ± 0.09	0.75 ± 0.09	0.18 ± 0.08
179-184	3.9 ± 0.2	2.0 ± 0.2	0.4 ± 0.1
184-188	7.0 ± 0.2	4.1 ± 0.2	0.8 ± 0.1
188-192	8.8 ± 0.2	5.5 ± 0.2	1.4 ± 0.1
192-198	8.3 ± 0.2	4.9 ± 0.2	1.81 ± 0.09
198-225	1.24 ± 0.05	0.53 ± 0.03	0.17 ± 0.01

Tabella 3.9: Differential cross sections (mbarn/MeV) in each considered kinetic energy range for carbon isotopes produced in the fragmentation reaction induced by ^{16}O beam on C_2H_4 target.

are shown in tab. 3.10 and fig. 3.19. All the plots referring to this analysis are reported in appendix B.

By subtracting the differential cross section obtained with the C target from the one obtained with the C_2H_4 target, as explained in section 2.3, it has been possible to extract the energy differential cross sections of a ^{16}O beam impinging on an hydrogen target. Table 3.11 and figure 3.20 show the differential cross sections found for each carbon isotope produced in a H target.

The differential cross sections here presented have been obtained using only MC data and supposing that half sample were real data. In the simulation the fragments are produced based on input cross sections, generally derived from nuclear models or extrapolated from experimental data at different energies. If the analysis works correctly, it

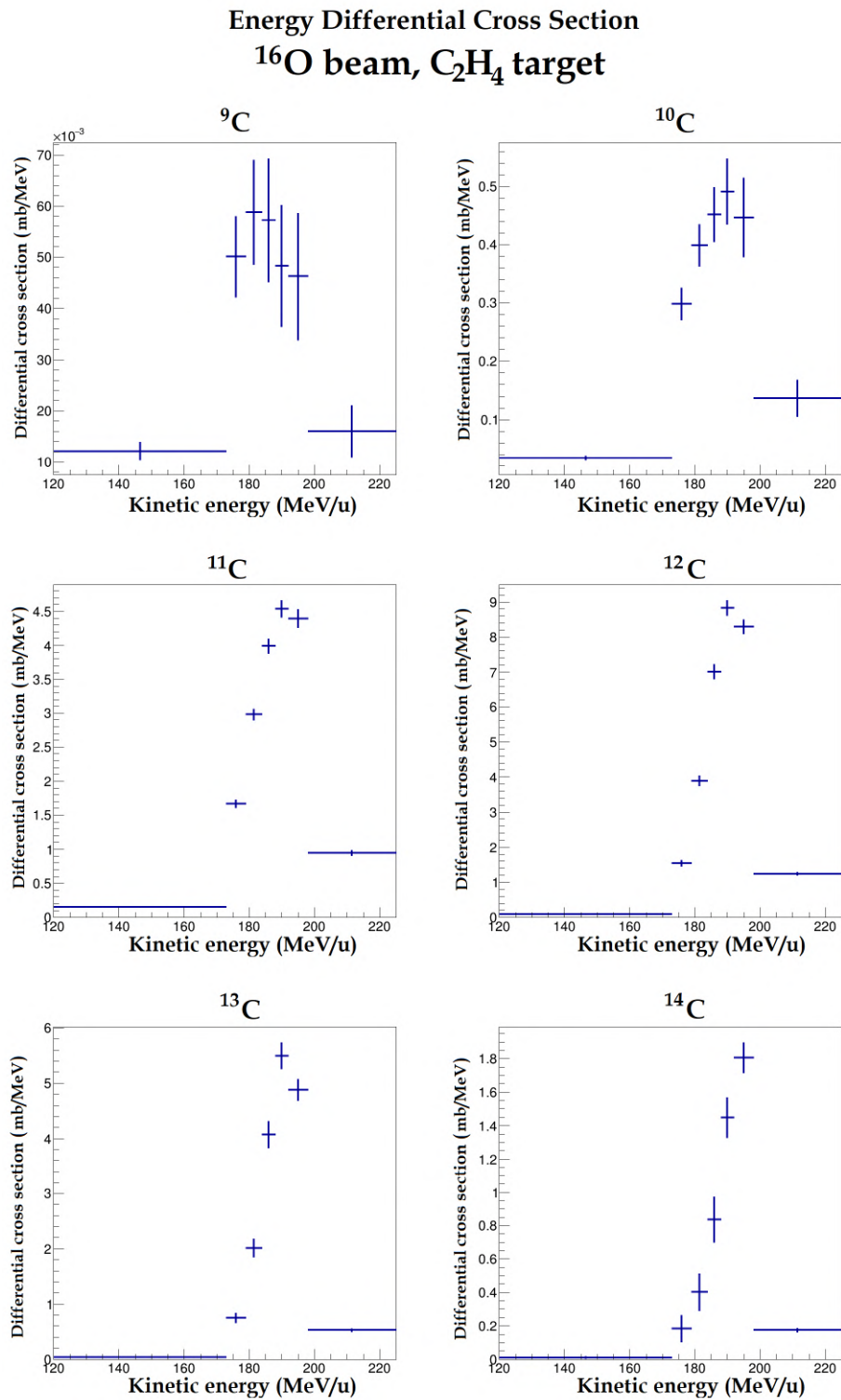


Figure 3.18: Energy differential cross section for the production of carbon isotopes in fragmentation reaction induced by a 200 MeV/u oxygen-16 beam impinging on a C_2H_4 target.

Energy range (MeV/u)	${}^9\text{C}$	${}^{10}\text{C}$	${}^{11}\text{C}$
120-173	0.006 ± 0.001	0.013 ± 0.002	0.058 ± 0.004
173-179	0.012 ± 0.003	0.08 ± 0.01	0.49 ± 0.03
179-184	0.014 ± 0.004	0.10 ± 0.02	0.72 ± 0.04
184-188	0.015 ± 0.006	0.09 ± 0.02	0.90 ± 0.05
188-192	0.013 ± 0.006	0.10 ± 0.02	0.88 ± 0.05
192-198	0.012 ± 0.006	0.7 ± 0.02	0.69 ± 0.05
198-225	0.003 ± 0.002	0.017 ± 0.006	0.09 ± 0.01
Energy range (MeV/u)	${}^{12}\text{C}$	${}^{13}\text{C}$	${}^{14}\text{C}$
120-173	0.040 ± 0.005	0.028 ± 0.005	0.008 ± 0.005
173-179	0.56 ± 0.05	0.37 ± 0.05	0.063 ± 0.03
179-184	1.30 ± 0.08	0.77 ± 0.07	0.14 ± 0.04
184-188	1.89 ± 0.09	1.26 ± 0.09	0.28 ± 0.04
188-192	1.87 ± 0.08	1.51 ± 0.09	0.48 ± 0.04
192-198	1.34 ± 0.07	1.07 ± 0.08	0.43 ± 0.03
198-225	0.108 ± 0.009	0.062 ± 0.007	0.020 ± 0.002

Tabella 3.10: Differential cross sections (mbarn/MeV) in each considered kinetic energy range for carbon isotopes produced in the fragmentation reaction induced by ${}^{16}\text{O}$ beam on C target.

Energy Differential Cross Section
 ^{16}O beam, C target

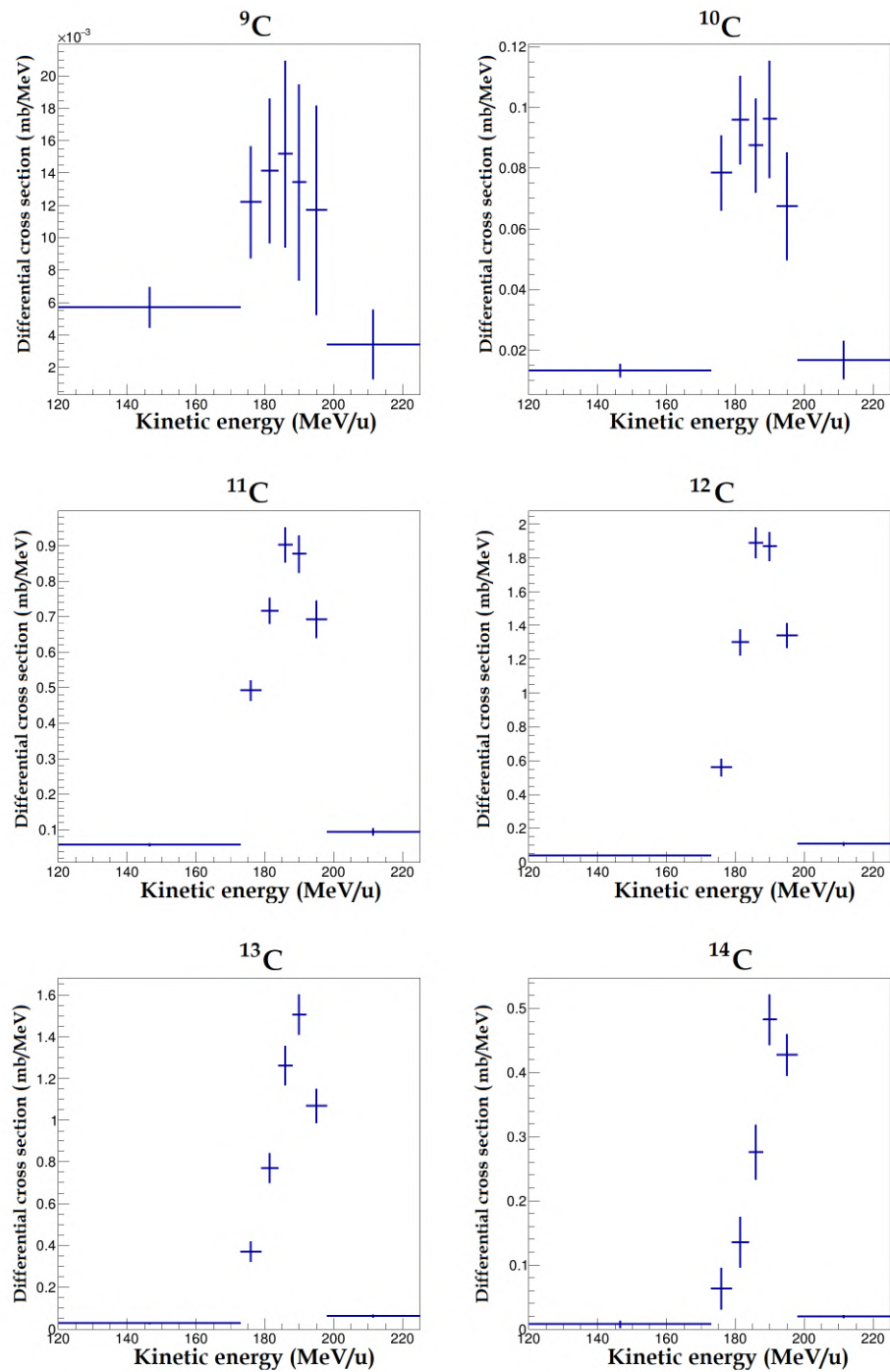


Figure 3.19: Energy differential cross section for the production of carbon isotopes in fragmentation reaction induced by a 200 MeV/u oxygen-16 beam impinging on a C target.

Energy range (MeV/u)	${}^9\text{C}$	${}^{10}\text{C}$	${}^{11}\text{C}$
120-173	0.000 ± 0.001	0.002 ± 0.002	0.009 ± 0.004
173-179	0.006 ± 0.004	0.4 ± 0.01	0.17 ± 0.03
179-184	0.008 ± 0.005	0.05 ± 0.02	0.39 ± 0.04
184-188	0.007 ± 0.006	0.07 ± 0.02	0.55 ± 0.05
188-192	0.005 ± 0.006	0.08 ± 0.02	0.70 ± 0.06
192-198	0.006 ± 0.006	0.08 ± 0.03	0.75 ± 0.06
198-225	0.002 ± 0.002	0.03 ± 0.01	0.19 ± 0.01
Energy range (MeV/u)	${}^{12}\text{C}$	${}^{13}\text{C}$	${}^{14}\text{C}$
120-173	0.002 ± 0.004	-0.004 ± 0.004	-0.001 ± 0.004
173-179	0.11 ± 0.05	0.00 ± 0.05	0.01 ± 0.04
179-184	0.32 ± 0.08	0.12 ± 0.08	0.03 ± 0.05
184-188	0.8 ± 0.1	0.4 ± 0.1	0.07 ± 0.06
188-192	1.3 ± 0.1	0.6 ± 0.1	0.12 ± 0.05
192-198	1.40 ± 0.09	0.69 ± 0.09	0.23 ± 0.04
198-225	0.26 ± 0.02	0.10 ± 0.01	0.034 ± 0.004

Tabella 3.11: Differential cross sections (mbarn/MeV) in each considered kinetic energy range for carbon isotopes produced in the fragmentation reaction induced by ${}^{16}\text{O}$ beam on H target.

Energy Differential Cross Section ^{16}O beam, H target

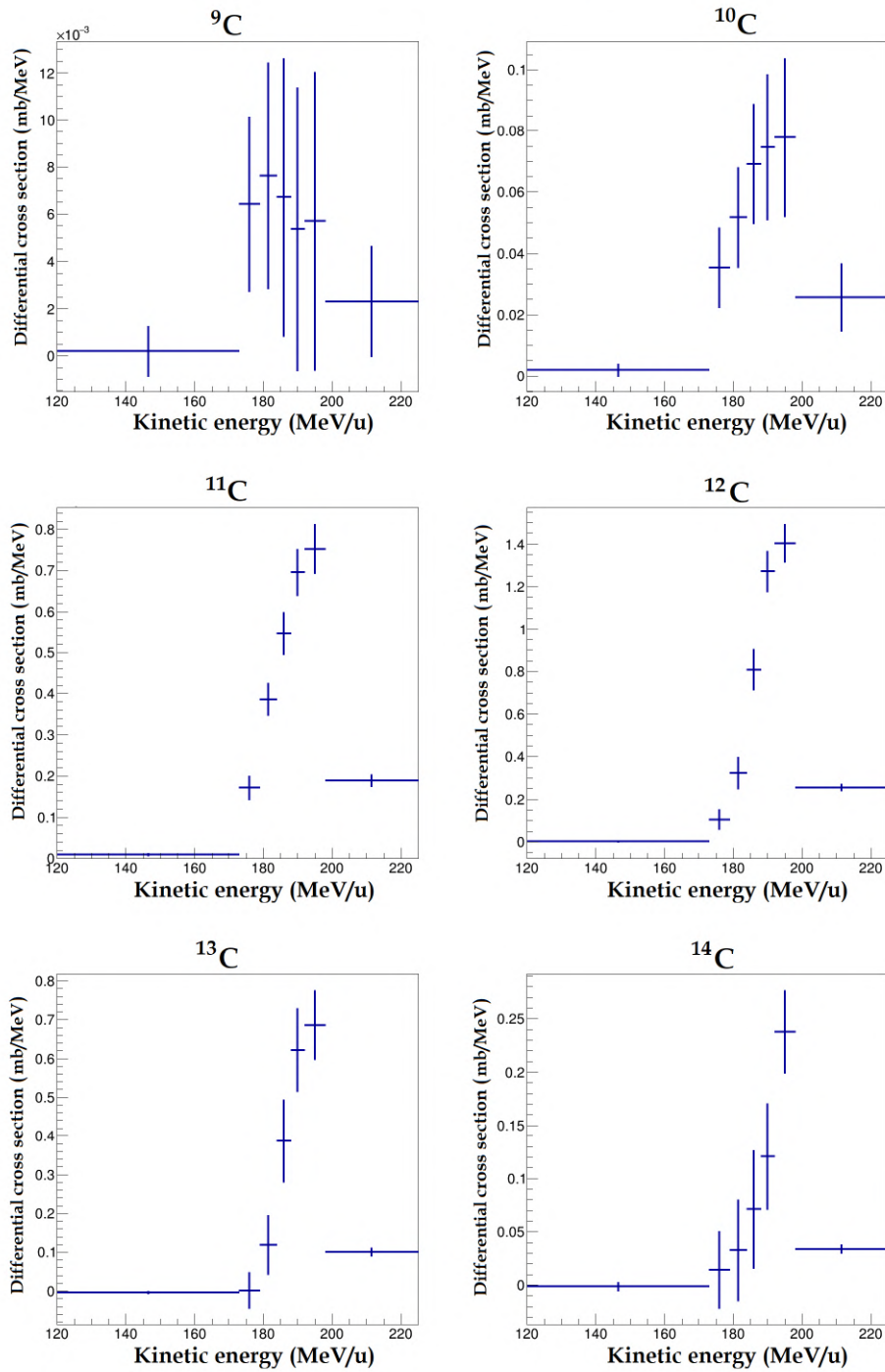


Figure 3.20: Energy differential cross section for the production of carbon isotopes in fragmentation reaction induced by a 200 MeV/u oxygen-16 beam impinging on a H target.

is obvious that the obtained cross sections must be compatible with the ones used in the MC software and, thus, the total number of fragments F produced in the simulation in the energy range i ($N_{F,i}^{\text{gen}}$) must be consistent with the number $N_{F,i} = \frac{(Y_{F,i} - B_{F,i})}{\epsilon_{F,i}}$ obtained in this analysis:

$$N_{F,i}^{\text{gen}} \approx N_{F,i} = \left(\frac{d\sigma_F}{dE} \right)_i \cdot N_{\text{prim}} \cdot N_t \cdot \Omega_i \quad (3.26)$$

where N_{prim} , N_t , Ω_i are the terms of eq. 3.18.

Figures 3.21 and 3.22 show the ratio between the reconstructed total number of fragments and the true total number $N_{F,i}^{\text{gen}}$. The ratios closest to 1 are those related to ^{11}C and ^{12}C ; this probably happens because these fragments are produced with a higher statistic than other C isotopes, allowing a better determination of the yield and the background component.

Figure 3.23 shows a comparison between the energy differential cross section obtained in the presented analysis (concerning a C_2H_4 , C and H target) for the production of ^{12}C and the FLUKA energy differential cross sections employed in the physical models of the simulation. The cross sections found in this analysis are in good agreement with those of the simulation, although those obtained on the C_2H_4 and C target are systematically shifted in energy of about 5 MeV. This effect is still under investigation. A complete comparison between the differential cross sections found in this analysis and the FLUKA cross section is given in appendix C.

By integrating the differential cross section in energy, it is possible to obtain the total production cross section of each fragment. In this case, since the differential cross section has been evaluated in discrete energy ranges, the total cross section σ_F of a fragment F can be derived by the relation

$$\sigma_F = \sum_i \left(\frac{d\sigma_F}{dE} \right)_i \Omega_i \quad (3.27)$$

where \sum_i represent the sum over all the considered energy ranges i . Another method has been also used in order to obtain a second value of the total cross section for each fragment: an analysis similar to the one described in this chapter has been made, but, this

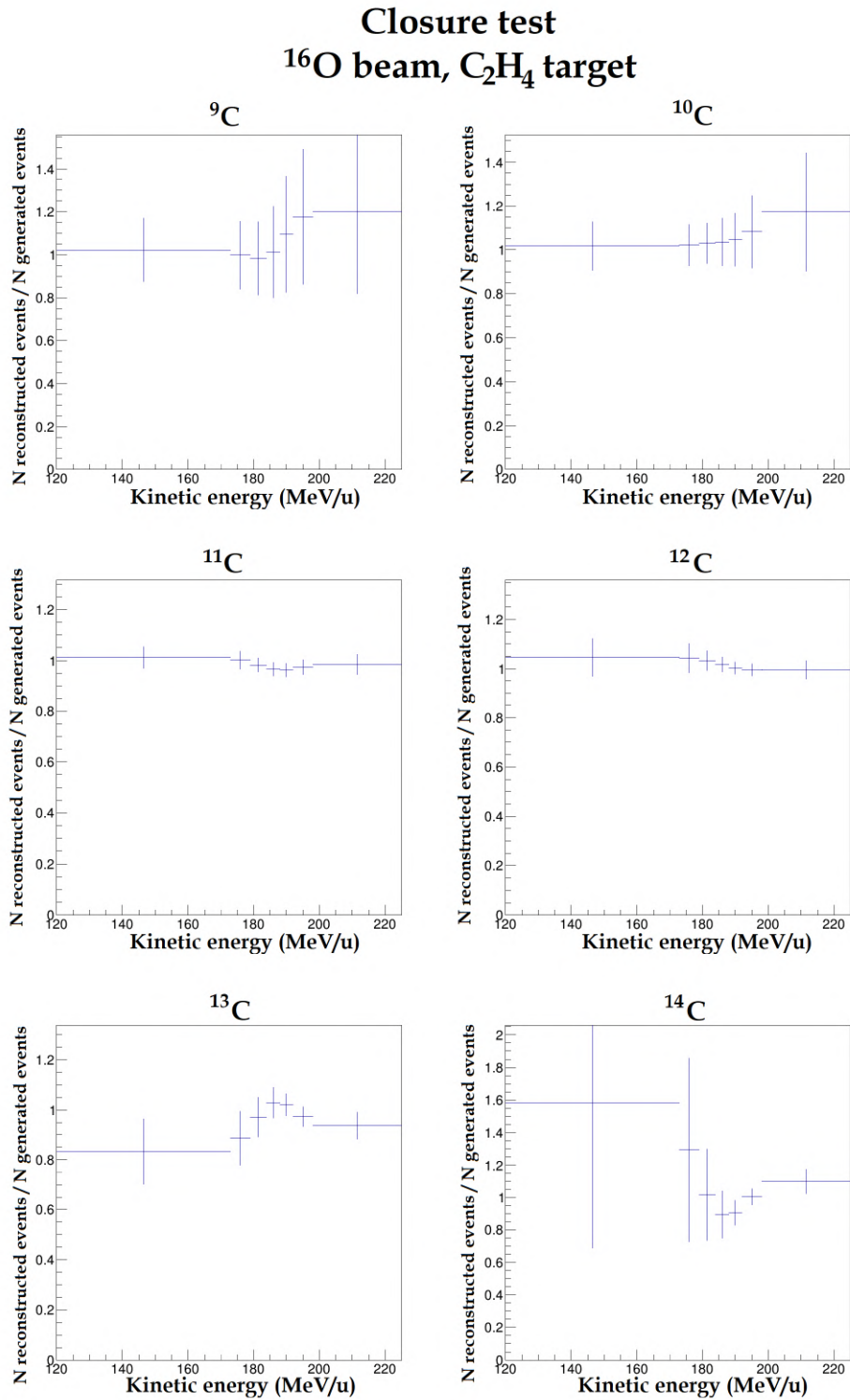


Figure 3.21: Ratio between the reconstructed total number of fragments for each carbon isotope and the total number of fragments generated in the simulation (^{16}O on C_2H_4).

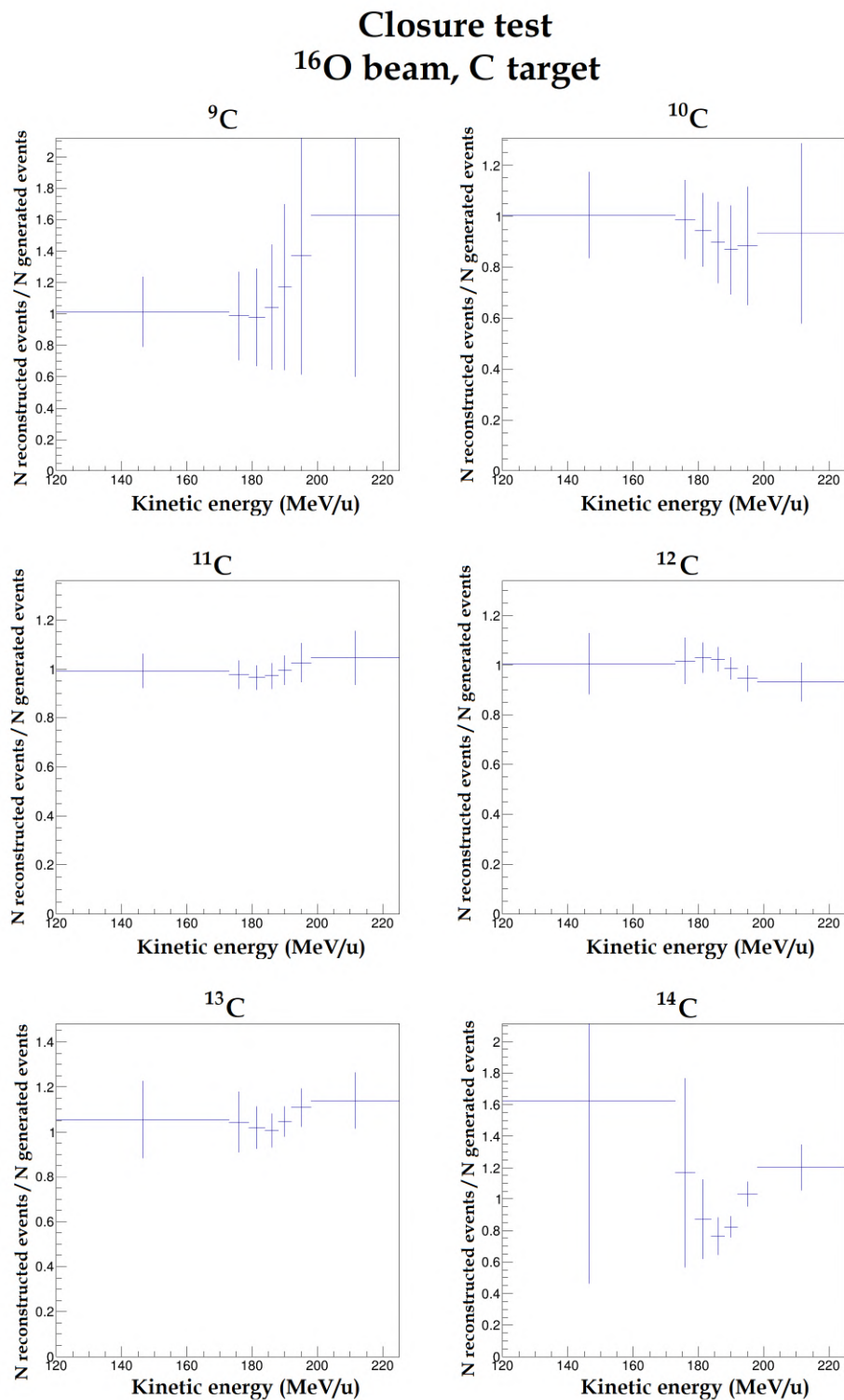


Figure 3.22: Ratio between the reconstructed total number of fragment for each carbon isotope and the total number of fragments generated in the simulation (^{16}O on C).

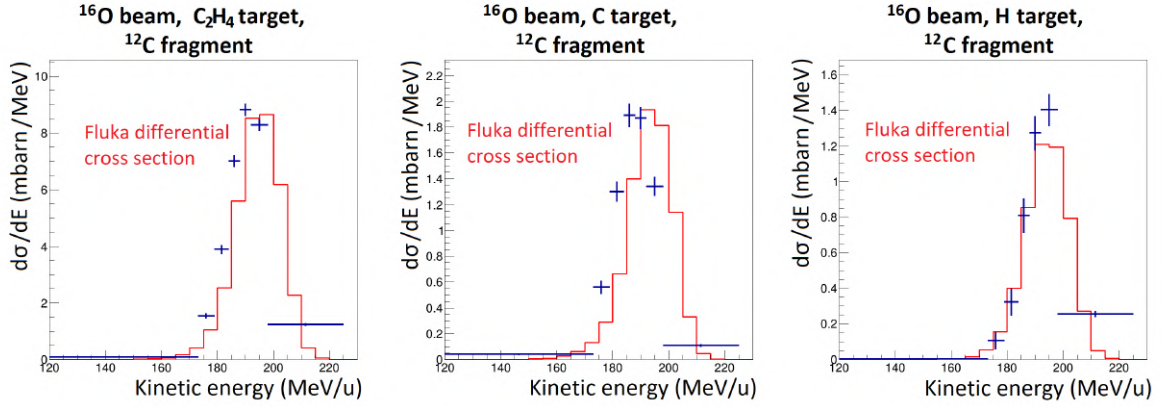


Figure 3.23: Comparison between the energy differential cross sections obtained in this analysis (blue) and the FLUKA cross sections used in the MC simulation (red), relating to the production of ^{12}C fragments in different targets (C_2H_4 , C and H).

time, a single wide kinetic energy range including all the production energies of carbon fragments has been considered and the total cross section has been obtained exploiting the relation

$$\sigma_{\text{F}} = \frac{Y_{\text{F}} - B_{\text{F}}}{N_{\text{prim}} \cdot N_{\text{t}} \cdot \epsilon_{\text{F}}} \quad (3.28)$$

The total cross sections thus found are listed in table 3.12, along with the total cross sections used in the FLUKA MC simulation as a comparison. We can see that these values are in good agreement: only in a few cases they can differ up to 10-15% from the FLUKA cross sections, and this happens with those fragments whose production is poor, leading to low statistics.

C₂H₄ target			
Fragment	σ_1^{tot} (mb)	σ_2^{tot} (mb)	$\sigma_{\text{FLUKA}}^{\text{tot}}$ (mb)
⁹ C	2.4 ± 0.2	2.1 ± 0.2	2.3 ± 1.6 %
¹⁰ C	16 ± 1	14 ± 2	15.4 ± 0.6 %
¹¹ C	119 ± 2	125 ± 5	122.6 ± 0.2 %
¹² C	180 ± 3	169 ± 9	179.9 ± 0.2 %
¹³ C	99 ± 2	108 ± 7	102.4 ± 0.2 %
¹⁴ C	28 ± 1	26 ± 2	28.5 ± 0.4 %
C target			
Fragment	σ_1^{tot} (mb)	σ_2^{tot} (mb)	$\sigma_{\text{FLUKA}}^{\text{tot}}$ (mb)
⁹ C	0.7 ± 0.1	0.7 ± 0.1	0.8 ± 1.7 %
¹⁰ C	3.2 ± 0.3	3.7 ± 0.8	3.6 ± 0.7 %
¹¹ C	23.4 ± 0.6	22 ± 2	24.3 ± 0.3 %
¹² C	38.0 ± 0.9	40 ± 4	39.3 ± 0.2 %
¹³ C	26.7 ± 0.9	27 ± 3	26.5 ± 0.3 %
¹⁴ C	7.6 ± 0.5	7.2 ± 0.6	8.4 ± 0.5 %
H target			
Fragment	σ_1^{tot} (mb)	σ_2^{tot} (mb)	$\sigma_{\text{FLUKA}}^{\text{tot}}$ (mb)
⁹ C	0.2 ± 0.1	0.2 ± 0.1	0.2 ± 0.9 %
¹⁰ C	2.3 ± 0.4	1.7 ± 0.9	2.0 ± 0.3 %
¹¹ C	18.0 ± 0.7	20 ± 2	18.3 ± 0.09 %
¹² C	26 ± 1	22 ± 4	25.1 ± 0.08 %
¹³ C	11 ± 1	14 ± 4	12.2 ± 0.1 %
¹⁴ C	3.3 ± 0.6	2.8 ± 0.8	2.9 ± 0.2 %

Tabella 3.12: Total production cross sections (mbarn) of carbon isotopes in fragmentation processes induced by ¹⁶O beam on different target. σ_1^{tot} refers to the total cross section obtained by integrating the differential cross sections given in fig. 3.18-3.20 ; σ_2^{tot} has been obtained with the same analysis as described in chapter 3, but performed in a single wide energy range including all the kinetic energy of the produced fragments; σ_2^{tot} is the cross section used in the FLUKA MC simulation.

Capitolo 4

GSI data analysis

A first data taking was performed at the GSI facility in April 2019 in order to verify the capability of the FOOT electronic apparatus by using a ^{16}O beam at 400 MeV/u of energy. The first run has been performed without a target, acquiring about 70 thousand events to equalize and calibrate the various detectors. Another run of about 60 thousand events has been performed with a carbon target, in order to acquire physical data of fragmentation processes.

Four different data takings have been performed with the emulsion setup, with oxygen beams with energy of 200 and 400 MeV/u both with a graphite (C) and polyethylene (C_2H_4) target. However, the measure and the results concerning the emulsion setup are beyond the content of this thesis.

The electronic setup used in this circumstance was composed of the Start Counter

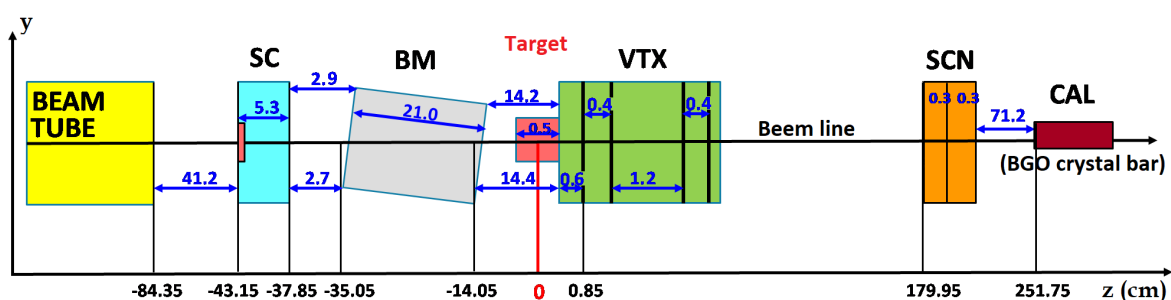


Figura 4.1: Schematic view of the electronic setup used at the GSI test beam.

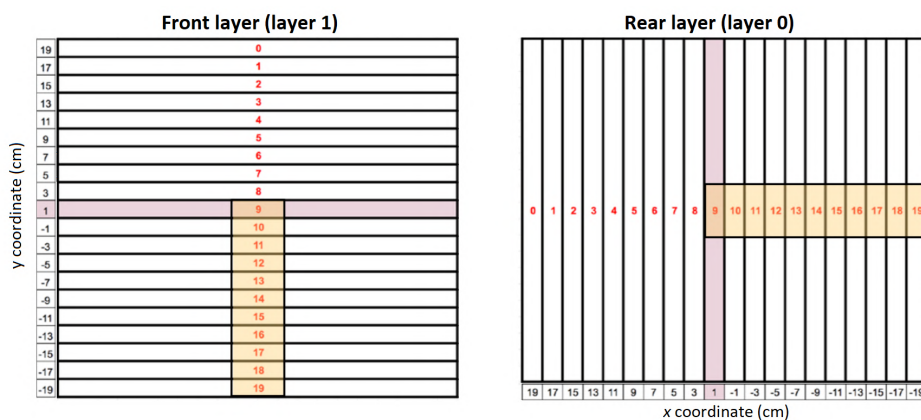


Figura 4.2: Schematic view of the scintillator used at the GSI test beam. The highlighted bars are those that have been calibrated at GSI with a 400 MeV 16-oxygen beam.

(SC), the Beam Monitor (BMN), the Vertex detector (VTX) , the Scintillator (SCN) and one BGO crystal bar. Figure 4.1 shows a scheme of the setup along with the relative distances between the detectors.

The results obtained from the data acquired at GSI, although preliminary, follow those obtained with the analysis of the MC data; in particular, the apparatus proved to be able to reconstruct the charge of the fragments with excellent resolution.

4.1 Scintillator calibration and performance

Currently, the analysis of data has been focused on the scintillator in order to provide the energy loss and, together with the STC, the ToF of the fragments, through which it is possible to obtain the charge Z exploiting the Bethe-Bloch formula (see section 3.1). The SCN consists of two layers of 20 bars each: the most upstream layer (front layer) is made of horizontal bars while the rear layer is made of vertical bars; the numbering of the bars and their disposition is given in fig. 4.2. By observing which bar in each layer has produced signal, it is therefore possible to identify the x and y coordinates of a particle that crosses the detector. In this section the calibration of the scintillator bars using the oxygen beam provided by the GSI facility is discussed. It has been not possible

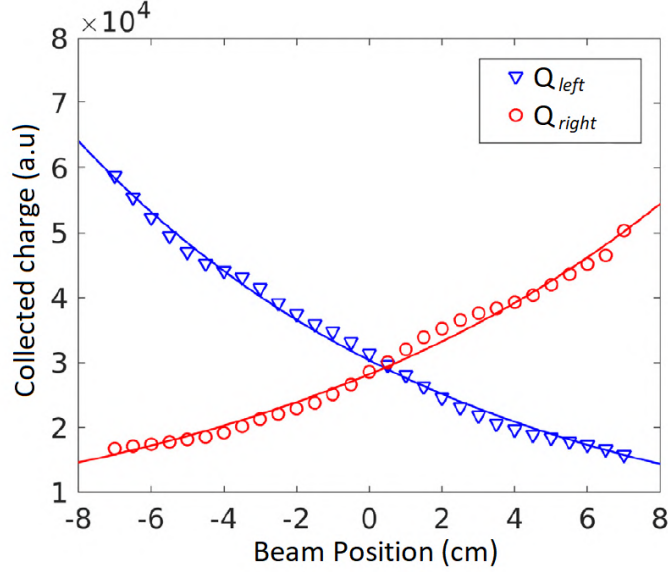


Figure 4.3: Mean collected charge at the two ends of a scintillating bar as a function of the position, for a proton beam with the fixed energy of 170 MeV. The 0 position represent the center of the bar. Solid lines represent the fit to the data with eq. 4.2 [91].

to calibrate all the 40 bars due to a lack of time during the data taking; the calibrated bars are highlighted in the figure 4.2.

te all the Energy equalisation and measurement The charge Q of the electrical signal produced by a scintillating bar depends on the energy lost by the incoming particle and on the position along the bar in which the particle has impinged. This is due to the fact that part of the scintillation light is absorbed by the scintillator material itself before reaching the silicon photomultiplier. The amount of light that reaches the SiPMT depends on the length x of material that it must pass through and on a material-dependant constant λ (attenuation length), thus the collected charge Q is given by

$$Q = Q_0 e^{-\lambda x} \quad (4.1)$$

where Q_0 is charge of the signal supposing no attenuation in the scintillator material. Figure 4.3 shows the charge collected at both the ends of a scintillating bar as a function

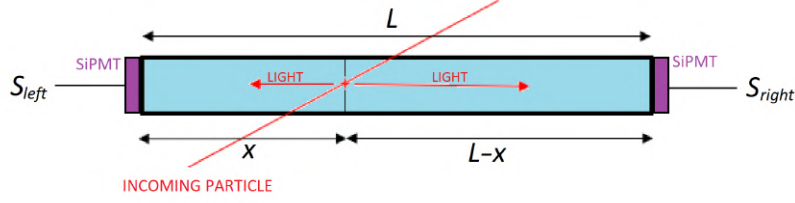


Figura 4.4: Scheme of the scintillator bar read-out. A signal charge independent by the particle hit position can be obtained by multiplying the signal charge at the left end (Q_{left}) by the signal charge at the right end (Q_{right}).

of the beam impinging position. This plot has been obtained using a proton beam as reported in [91]. In the case of the FOOT scintillator, λ is about 40 cm and can be obtained for each bar by fitting the charge collected by the SiPMT at one of its end as a function of the beam position.

Since the read-out of the bars of the scintillator is implemented at both ends (indicated with *left* and *right*), it is possible to obtain a position independent signal in the following way:

$$Q = \sqrt{Q_{\text{left}} \cdot Q_{\text{right}}} = \sqrt{Q_0 e^{-\lambda x} \cdot Q_0 e^{-\lambda(L-x)}} = Q_0 e^{-\lambda \frac{L}{2}} \quad (4.2)$$

where L is the total length of the bar (fig. 4.4).

Even if the energy deposited is the same, the bars do not produce the exact same signal. This is due to small differences that may occur in the scintillating material, in the coupling between the bar and the SiPMT or in the read-out electronics. In order to have a homogeneous response from the whole scintillator, the signal coming from each bar has been equalised so that all the bars produce the same signal charge if crossed by ^{16}O particles with 400 MeV/u kinetic energy. Fig 4.5 shows the distributions of signal charge from two different bars before and after the equalisation. It can be seen that after the equalization the two peaks are centered at the same charge value. In this analysis a threshold equal to 3 (a.u) on the signal charge has been set to define a touched bar.

The equalisation factor (F_{eq}) of each bar has been found as the ratio between an arbitrary chosen equalisation value (in this case equal to 70 a.u.) and the mean value of

the non-equalised distribution (Q_{mean}):

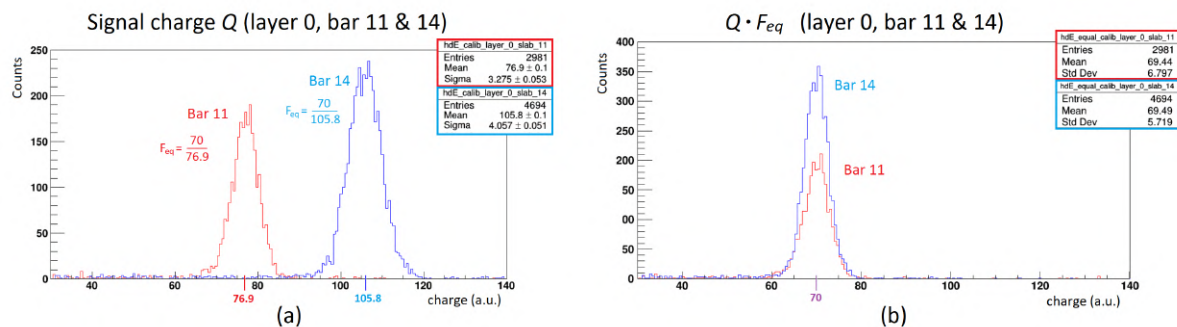


Figure 4.5: (a) Distributions of signal charge from bar 11 and bar 14 of the rear layer of the scintillator obtained with ^{16}O particles (400 MeV/u); F_{eq} is the equalisation factor. (b) Same distributions after equalisation. The equalisation value has been arbitrarily chosen equal to 70.

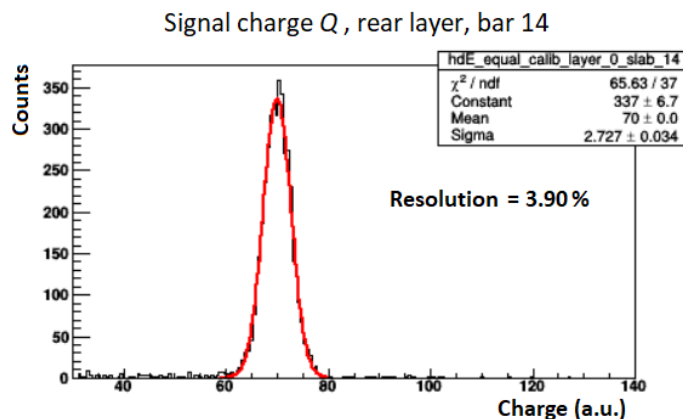


Figure 4.6: Distributions of equalised signal charge from bar 14 of the rear layer.

$$F_{\text{eq,bar}} = \frac{70}{Q_{\text{bar,mean}}} \quad (4.3)$$

Fig. 4.6 shows the distribution of the equalised signal charge from one of the scintillator bars. The resolution of this distribution can be obtained by fitting it with a Gauss

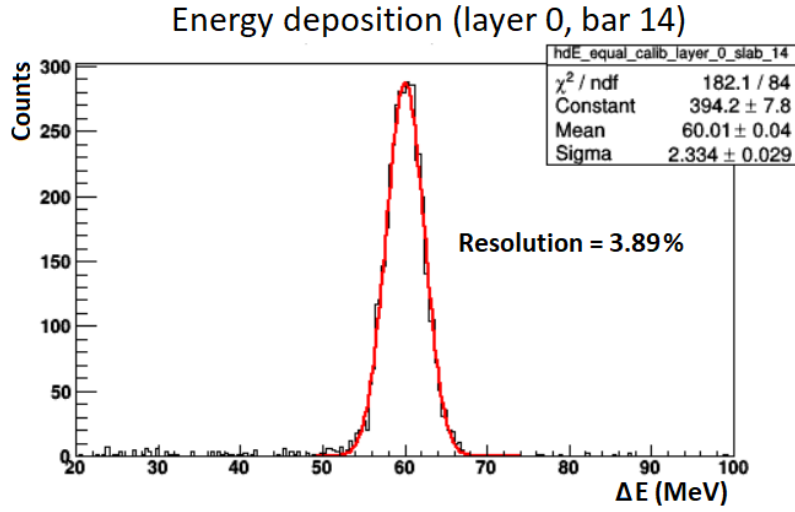


Figura 4.7: Energy deposited by ^{16}O particles (400 MeV/u) in the bar 14 of the scintillator.

function. In table 4.1 the equalisation factors and the resolution obtained for all the equalised bars are listed.

From the MC simulation we know that a 400 MeV ^{16}O particle releases 60 MeV of energy within each layer of the scintillator. This information allows us to obtain the energy loss (dE/dx) of the beam particles in the scintillator material by dividing the energy deposition by the bar thickness (0.3 cm), as in eq. 3.1. In figure 4.7 the distribution of the energy deposited (ΔE) in one scintillator bar is shown. The resolution on ΔE is, within a 0.01% error, the same as that of the signal charge.

In order to have an average precision of the scintillator, the measurements performed by all the bars have been collected in a single distribution. In each event, the charge collected by the bars that have produced signal in the two layers has been summed, as has been done in the analysis of fragmentation events discussed in section 4.2. Fig. 4.8 shows the distribution of the signal charge produced in the scintillator by ^{16}O of 400 MeV/u kinetic energy; a resolution of about 4% is achieved.

Layer	Bar	F_{eq} (a.u.)	Signal charge Q (a.u.)	Resolution (%)
0	9	0.967	72.6 ± 5.1	7.02
0	10	0.836	70.0 ± 2.9	4.21
0	11	0.910	70.0 ± 3.0	4.29
0	12	0.844	70.0 ± 2.8	4.07
0	13	0.776	70.1 ± 2.8	4.05
0	14	0.667	70.0 ± 2.7	3.90
0	15	0.714	70.0 ± 2.8	3.95
0	16	0.865	70.0 ± 2.9	4.10
0	17	1.146	69.9 ± 3.0	4.28
0	18	1,176	69.9 ± 3.0	4.23
0	19	1.043	70.0 ± 2.9	4.16
1	9	0.952	70.0 ± 3.9	5.65
1	10	0.989	69.9 ± 3.2	4.55
1	11	0.994	70.0 ± 2.6	3.77
1	12	0.887	69.9 ± 2.6	3.70
1	13	1.056	70.0 ± 2.7	3.92
1	14	1.034	69.9 ± 3.5	5.06
1	15	1.167	70.0 ± 3.7	5.24
1	16	1.115	70.1 ± 3.6	5.14
1	17	1.186	70.0 ± 3.7	5.26
1	18	1.074	69.9 ± 3.5	5.00
1	19	1.151	70.0 ± 3.4	4.89

Tabella 4.1: Equalisation factors of each equalised bar of the scintillator; mean, standard deviation and resolution of the related signal charge distribution obtained with a 400 MeV ^{16}O beam.

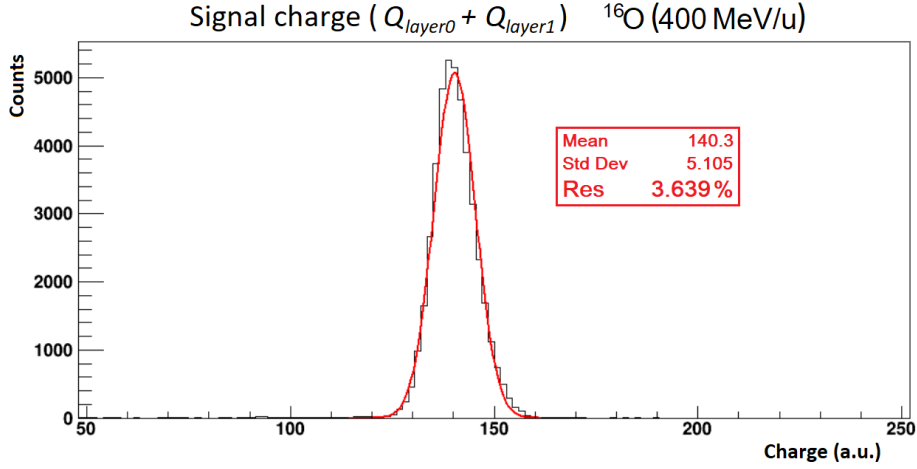


Figure 4.8: Distribution of the signal charge from the scintillator obtained with a 400 MeV/u ^{16}O beam. The signal charge of each event is given by the sum of the charge collected in the two layers.

4.1.1 ToF system calibration and Z reconstruction

The measure of the time of flight is performed by the STC and the SCN. In each event, the time recorded by a scintillator bar hit by a particle (t_{bar}) is given by the mean of the time of the signal coming from its left end and its right end:

$$t_{\text{bar}} = \frac{t_{\text{bar, left}} + t_{\text{bar, right}}}{2} \quad (4.4)$$

The time of the event recorded by the scintillator (t_{SCN}) is then given by the mean of the times obtained from the bars that have been hit in the two layers:

$$t_{\text{SCN}} = \frac{t_{\text{bar, layer0}} + t_{\text{bar, layer1}}}{2} \quad (4.5)$$

All the beam particles travel at the same velocity and, thus, have the same ToF, however, the time measured by the scintillator can vary from bar to bar, due to differences in the read-out electronics, especially in the different length of cables used for

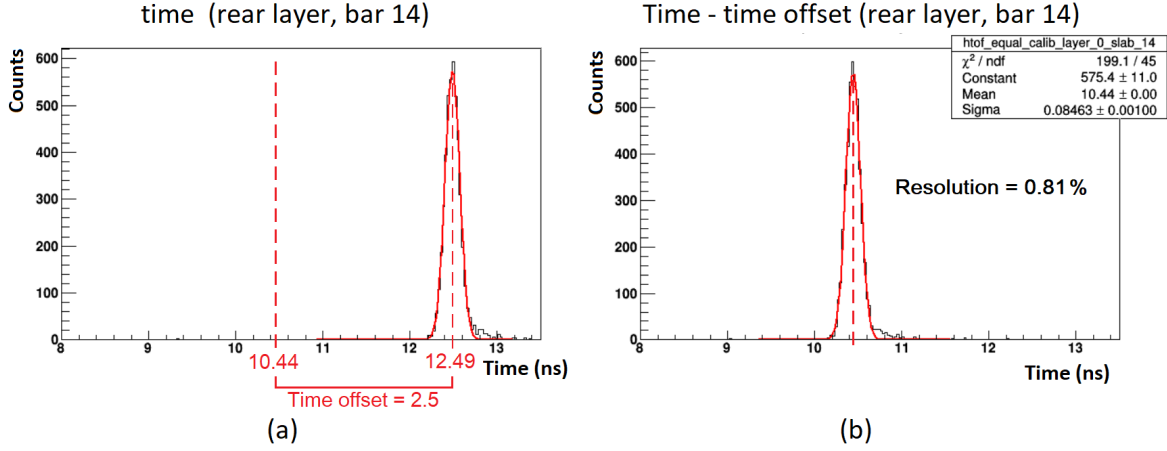


Figure 4.9: Distribution of time measured with the bar 14 of the rear layer of the scintillator before (a) and after the equalisation (b). This distribution has been obtained by detecting only ^{16}O (400 MeV/u) particles coming from the test beam. 10.44 ns is the time that a beam particle takes to travel from the Start Counter to the scintillator; all the bars has been equalised at this time by subtracting the corresponding time offset.

wiring. For this reason, the time signal of each bar of the scintillator has been equalised to 10.44 ns, which is the time that the beam particles takes to travel from the Start Counter to the scintillator (ToF_{beam}) in absence of target. This time value has been obtained analytically, starting from the beam velocity (β_{beam}), and it has been verified with the MC simulation:

$$ToF_{\text{beam}} = \frac{z_{\text{STC}} - z_{\text{SCN}}}{c \cdot \beta_{\text{beam}}} = 10.44 \text{ ns} \quad (4.6)$$

where z_{STC} and z_{SCN} are the positions of the STC and the SCN along the beam axis. The time offset (t_{off}) of each bar has been evaluated as the difference between the reference time of flight in eq. 4.6 and the average time measured by the bar ($t_{\text{bar,mean}}$):

$$t_{\text{off,bar}} = t_{\text{bar,mean}} - ToF_{\text{beam}} \quad (4.7)$$

For each bar, $t_{\text{bar,mean}}$ has been obtained by performing a Gaussian fit on the time

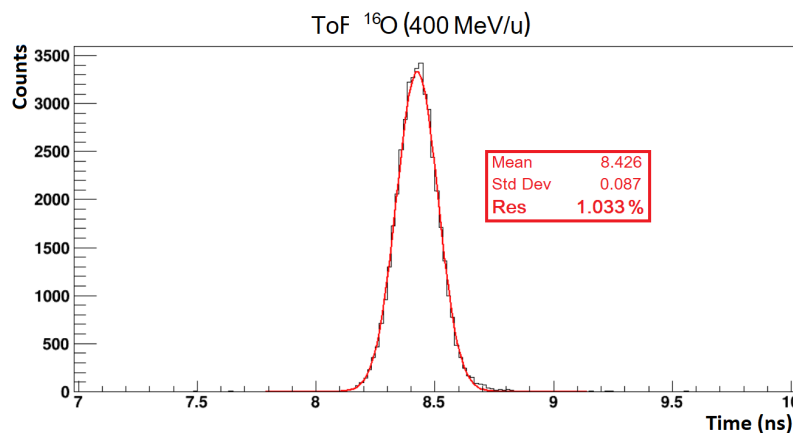


Figure 4.10: Distribution of time of flight of beam particles from the intended target position to the scintillator. This time measurement has been obtained as the mean value of the times measured by the two layer of the scintillator.

distribution obtained with the single bar in the test beam and by taking the mean value of this Gauss function (tab. 4.2). Figure 4.9 shows, as an example, the time distribution obtained with one bar of the scintillator before and after the equalisation and the related time offset and resolution. In table 4.2 the time resolutions of all the calibrated bars are shown: these values ranges between 0.8 and 1 %, corresponding to an uncertainty of the time measurement between 84 and 105 ps.

Figure 4.10 shows the time distribution obtained with the entire scintillator by combining the measurements of the two layer, as indicated in eq. 4.5. Although the target was not present in this run, the time taken by the particles to travel from the detector to the intended target position (2.01 ns) has been subtracted, thus the distribution is centered at 8.43 ns instead of 10.44 ns. This has been done in order to have ToF measures comparable with those performed on fragmentation events.

Layer	Bar	t_{off} (ns)	Mean ToF (ns)	σ (ps)	Resolution (%)
0	9	2.04	10.44	101	0.97
0	10	2.02	10.44	94	0.90
0	11	1.96	10.44	92	0.88
0	12	1.93	10.44	93	0.89
0	13	2.09	10.44	85	0.82
0	14	2.04	10.44	84	0.80
0	15	1.99	10.44	86	0.82
0	16	1.93	10.44	87	0.84
0	17	2.04	10.44	105	1.00
0	18	2.01	10.44	102	0.98
0	19	1.91	10.44	106	1.01
1	9	1.95	10.44	92	0.87
1	10	1.96	10.44	99	0.99
1	11	1.90	10.44	100	0.95
1	12	1.82	10.44	101	0.96
1	13	1.81	10.44	100	0.96
1	14	1.99	10.44	93	0.89
1	15	1.92	10.44	88	0.84
1	16	1.88	10.44	92	0.88
1	17	1.85	10.44	91	0.87
1	18	2.00	10.44	93	0.89
1	19	1.92	10.44	90	0.86

Tabella 4.2: Time offset of each calibrated bar; mean, standard deviation and resolution of the time of flight of 400 MeV ^{16}O particles measured with each scintillator bar.

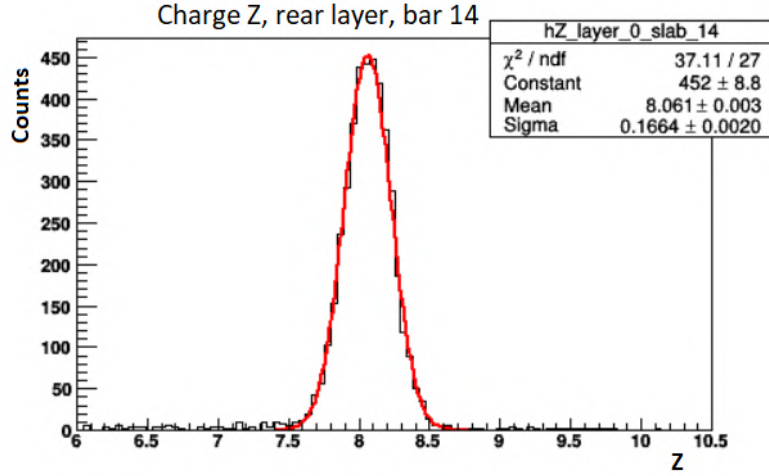


Figura 4.11: Z Distribution obtained with the energy loss and the ToF measured by the bar 14 of the scintillator.

The measure of ToF and energy loss leads to the reconstruction of the charge Z by exploiting the Bethe-bloch formula (eq. 1.1). Fig. 4.11 shows the distribution of Z obtained with one scintillator bar, while mean values and resolutions of the Z reconstructed from the measurement performed by each bar are listed in the table 4.3. The resolution of the charge Z is typically half the resolution of the deposited energy (signal charge), since it depends on the square root of the energy loss. Z depends also on β , and so on the ToF measure, but its precision is $\leq 1\%$ and thus it does not substantially worsen the overall resolution.

Fig. 4.12 shows the Z distribution obtained with the entire scintillator, by combining the measure of ToF and energy loss performed by the two layers, as previously described. As expected, there is only one peak corresponding to the charge of the beam particles ($Z = 8$); the resolution is about 2%, which means that the charge Z can be identified with the precision obtained in the MC data analysis.

Layer	Bar	Z mean	Standard deviation	Resolution (%)
0	9	8.201	0.322	3.93
0	10	8.065	0.182	2.26
0	11	8.064	0.182	2.26
0	12	8.062	0.175	2.17
0	13	8.067	0.171	2.12
0	14	8.061	0.166	2.06
0	15	8.060	0.171	2.12
0	16	8.063	0.173	2.15
0	17	8.055	0.190	2.35
0	18	8.058	0.190	2.35
0	19	8.0572	0.188	2.33
1	9	8.058	0.247	3.06
1	10	8.058	0.194	2.40
1	11	8.062	0.166	2.06
1	12	8.059	0.164	2.04
1	13	8.063	0.174	2.16
1	14	8.057	0.209	2.60
1	15	8.054	0.214	2.65
1	16	8.061	0.212	2.64
1	17	8.062	0.217	2.61
1	18	8.057	0.210	2.61
1	19	8.056	0.204	2.53

Tabella 4.3: Mean, standard deviation and resolution of Z distributions obtained from the measures performed by each scintillator bar on a 400 MeV ^{16}O beam. .

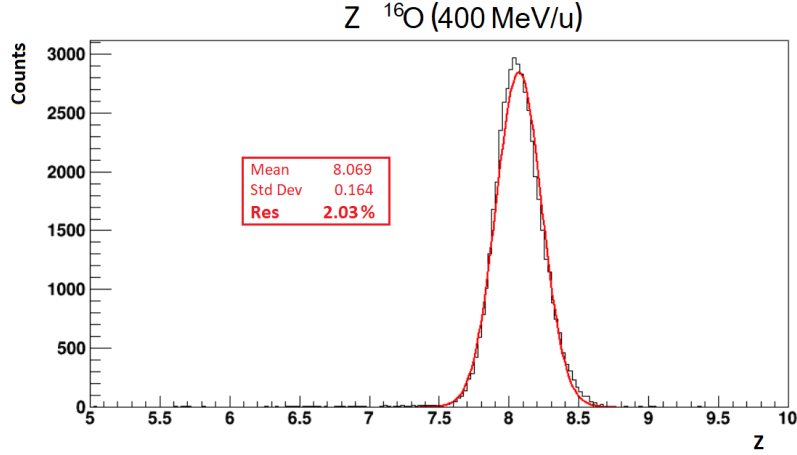


Figura 4.12: Distribution of the charge Z obtained from the scintillator measurements performed on 400 MeV/u ^{16}O particles.

4.2 Fragmentation measurement

Data from fragmentation events produced by a 400 MeV ^{16}O beam on a 5 mm thick carbon target have been analysed in order to measure the energy loss and the ToF of the fragments.

Because of the multiplicity of the produced fragments, the bars of each layer of the scintillator affected in each event are very often more than one. This can generate ambiguities in the reconstruction of the position of the particles and in the number of fragments detected. As an example, if two fragments impinge on the scintillator in different positions (fig. 4.13), four bars produce signal (two in the front layer and two in the back layer), the intersections between the bars are four, but only two of these are due to a crossing particle, while the other two are due to bars activated in the two layers by different fragments (*combinatorial background* or *ghosts*). In order to solve these ambiguities, the analysis software examines each combination of bars that have given signal and decides whether it is an actual particle based on two criteria:

$$\frac{\Delta Q}{Q_{\text{mean}}} = \frac{Q_{\text{layer0}} - Q_{\text{layer1}}}{\frac{1}{2}(Q_{\text{layer0}} + Q_{\text{layer1}})} < 0.1 \quad (4.8)$$

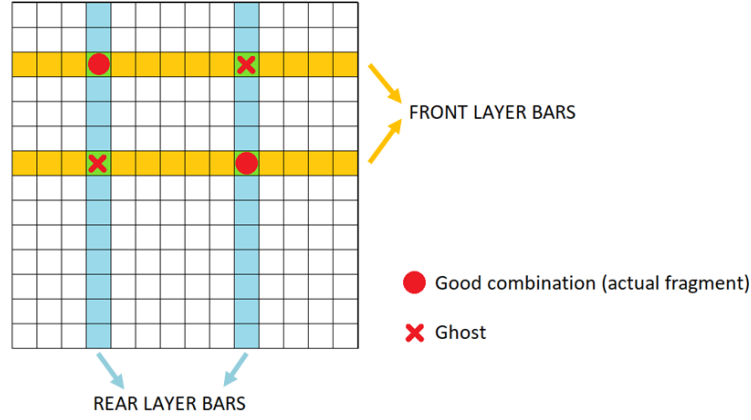


Figura 4.13: Scheme of the ghosting phenomenon in the scintillator: two impinging fragments produce four bar intersections, as the detector has been hit by four particles.

$$\frac{\Delta t}{t_{\text{mean}}} = \frac{t_{\text{layer0}} - t_{\text{layer1}}}{\frac{1}{2}(t_{\text{layer0}} + t_{\text{layer1}})} < 0.02 \quad (4.9)$$

where Q_{layer0} , Q_{layer1} and t_{layer0} , t_{layer1} are the charge and the time of the signals from the rear layer and the front layer respectively. In other words, the analysis selects only the events in which the signal charge and time provided by the front and by the rear layer are in agreement. As for the calibration, a threshold equal to 3 (a.u.) on the charge of the signals coming from the bars has been set.

The distribution of signal charge of the produced fragments provided by the scintillator (calculated as the sum of the signal charge produced in the two layers) is shown in figure 4.14. The calibration in energy performed at GSI is not complete, since only one single-energy beam was available. For this reason, it is not possible to associate the signal charge with the corresponding values of energy deposition and, therefore, to identify the charge Z of the fragments. Anyhow, the distribution in fig. 4.14 already presents characteristic peaks corresponding to the different produced fragments: the oxygen peak is much higher, since about 96% of beam crosses the target and the detectors without interacting; the hydrogen peak is not visible, since the amplification of the signal has been set in order to favor the detection of the heavier fragments, which is the purpose

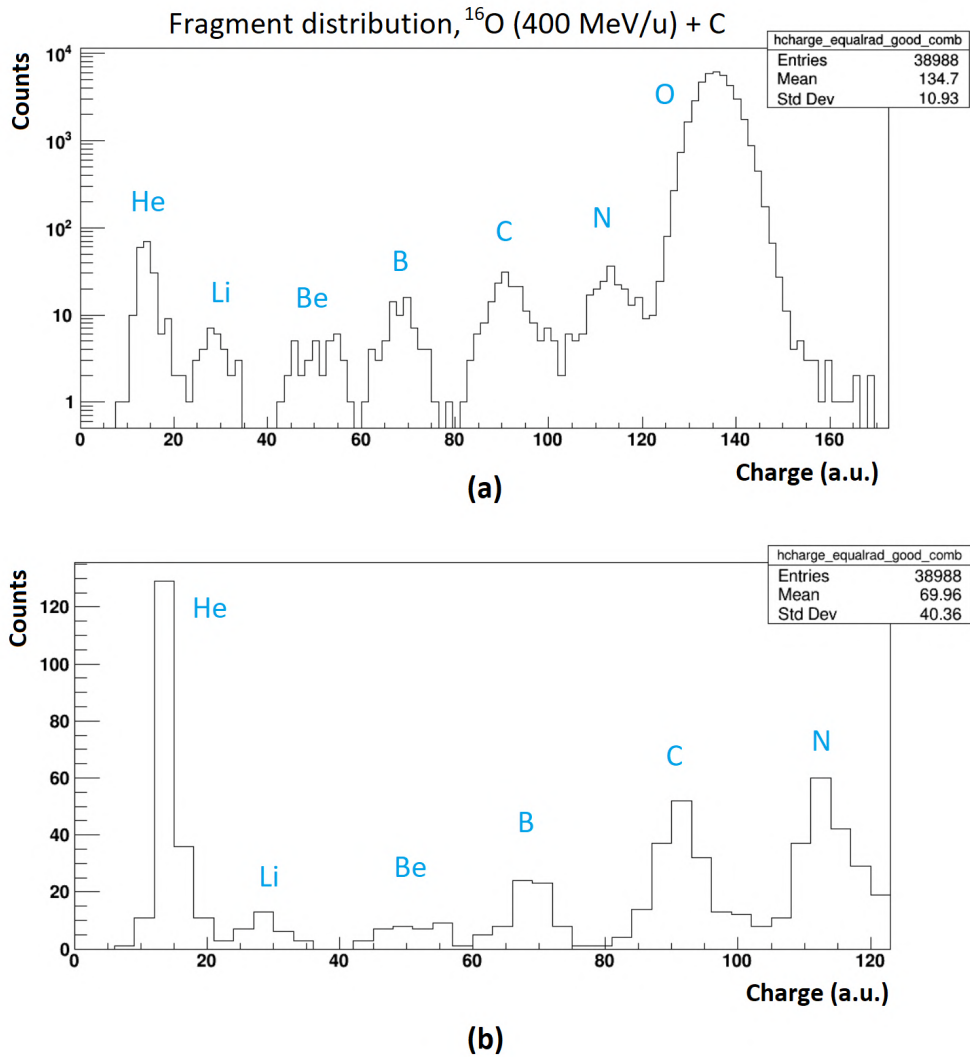


Figure 4.14: (a) Distribution of the signal charge from the scintillator obtained with fragmentation events induced by ^{16}O (400 MeV/u) impinging on a C target. (b) Same distribution, but in linear scale; the oxygen peak has not been included in order to better appreciate the other peaks.

	p (60 MeV)	¹² C (400 MeV/u)	¹² C (260 MeV/u)	¹² C (115 MeV/u)
ΔE_{layer0} (MeV)	3.37 ± 0.16	33.4 ± 1.2	42.2 ± 1.1	74.1 ± 1.1
ΔE_{layer1} (MeV)	3.54 ± 0.17	33.5 ± 1.2	42.5 ± 1.1	77.4 ± 1.1

Tabella 4.4: Energy lost inside the scintillator layers by the particles used at CNAO for calibration.

of this FOOT setup.

4.2.1 CNAO calibration and Z identification

Another calibration of the scintillator has been performed at the CNAO facility (Pavia) using carbon beams at three different energies (115, 260 and 400 MeV/u) and a 60 MeV proton beam. The energy lost by these particles inside the scintillator has been derived from Montecarlo simulations and it is shown in table 4.4.

The charge of the signal collected by the scintillating bars has been measured as described in section 4.1 and the values obtained for each beam type have been plotted and fitted following the Birks' law:

$$Q = p_a \frac{\Delta E}{1 + p_b \Delta E} \quad (4.10)$$

where p_a and p_b are the two parameters of the function: p_a is the absolute normalization, which represents the proportionality between the energy deposited and the signal charge; p_b is the Birks' constant, which depends on the scintillator material and becomes important at high deposited energies, due to quenching effects, moving the Birks' law away from linearity. In fact, the more the energy deposited increases, the lower the percentage of scintillating light collected by the SiPMT is, up to a saturation effect of the produced signal.

The purpose of the calibration is to obtain the p_a and p_b parameters for each bar in order to have a function that associates an energy deposition value to each signal charge. Figure 4.15 shows the calibration of one bar as an example, while table 4.5 shows the parameters p_a and p_b of all the bars calibrated at CNAO.

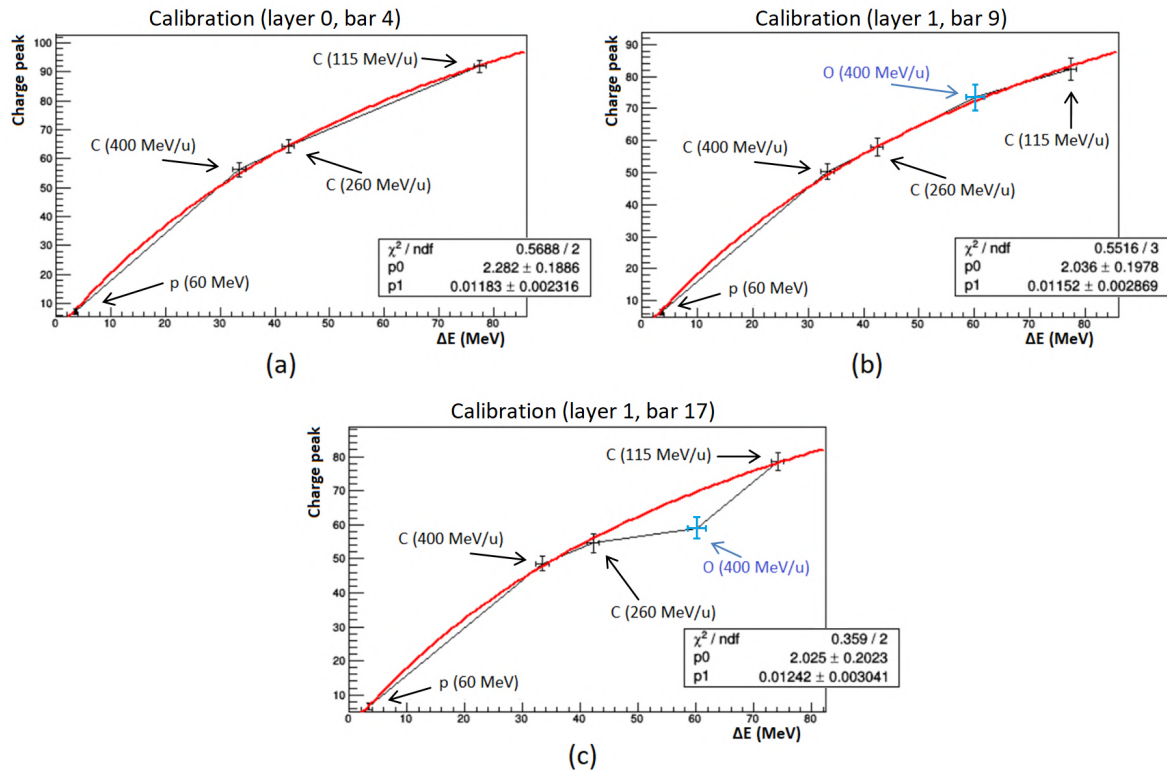


Figure 4.15: Calibration of three scintillator bars. (a) Calibration performed at CNAO with proton and carbon beams. (b) Calibration performed with CNAO and GSI data from proton, carbon and oxygen beams. (c) Calibration performed with CNAO and GSI data; the oxygen point is not in agreement with the other data, therefore it is not included in the fit.

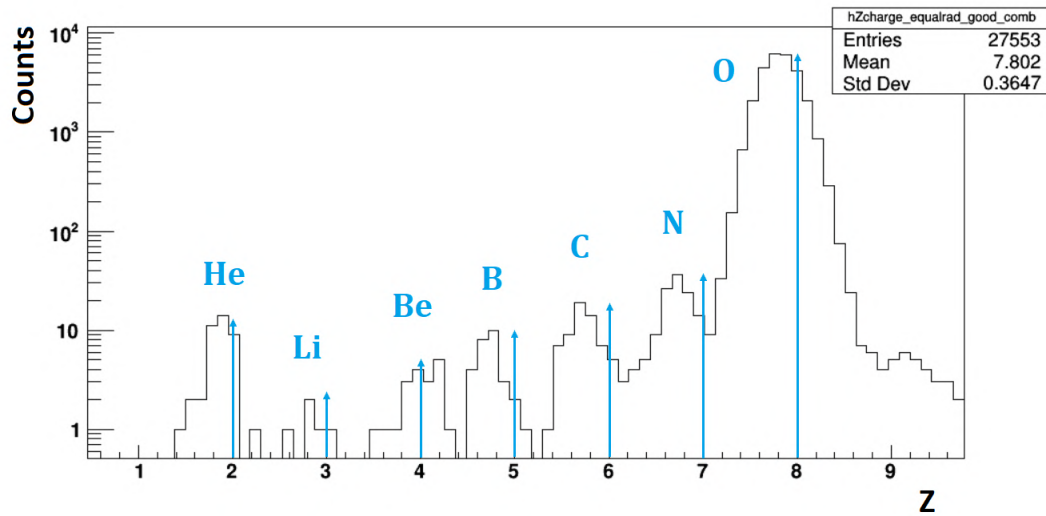


Figura 4.16: Charge Z of the fragments produced at the GSI data taking by using a 400 MeV/u ^{16}O beam impinging on a C target.

Thanks to this calibration, it has been possible to obtain the energy loss of the fragments detected at the GSI data taking and, therefore, to identify their charge Z exploiting the eq. 1.1. Figure 4.16 shows the Z of the fragments produced by a 400 MeV/u ^{16}O beam impinging on a carbon target. It can be seen that the peaks are not perfectly centered at the correct charge value but they are slightly shifted to greater values. This effect is not fully understood, anyway, as a preliminary result obtained with a very low statistics, we can certainly say that FOOT is able to identify the charge of all the produced fragments, as expected from the MC data analysis.

Layer	Bar	p_a (MeV $^{-1}$)	p_b (MeV $^{-1}$)
0	1	2.13 ± 0.21	0.0133 ± 0.0030
0	2	2.31 ± 0.26	0.0139 ± 0.0034
0	3	2.01 ± 0.25	0.0118 ± 0.0038
0	4	2.28 ± 0.19	0.0118 ± 0.0023
0	5	2.33 ± 0.19	0.0127 ± 0.0024
0	6	2.21 ± 0.20	0.0128 ± 0.0026
0	7	2.04 ± 0.17	0.0122 ± 0.0024
0	9	2.06 ± 0.21	0.0119 ± 0.0031
0	17	1.99 ± 0.17	0.0130 ± 0.0026
0	18	1.95 ± 0.18	0.0132 ± 0.0028
1	0	2.33 ± 0.22	0.0149 ± 0.0030
1	1	2.26 ± 0.20	0.0143 ± 0.0028
1	2	2.44 ± 0.20	0.0138 ± 0.0025
1	3	2.18 ± 0.18	0.0132 ± 0.0025
1	5	1.79 ± 0.17	0.0135 ± 0.0030
1	6	2.26 ± 0.20	0.0133 ± 0.0027
1	7	2.35 ± 0.21	0.0135 ± 0.0027
1	8	2.30 ± 0.21	0.0138 ± 0.0028
1	9	2.04 ± 0.20	0.0115 ± 0.0029
1	10	2.16 ± 0.24	0.0132 ± 0.0035
1	11	2.11 ± 0.20	0.0131 ± 0.0029
1	12	2.33 ± 0.19	0.0125 ± 0.0025
1	13	1.97 ± 0.18	0.0126 ± 0.0027
1	14	2.53 ± 0.29	0.0188 ± 0.0045
1	15	1.93 ± 0.20	0.0118 ± 0.0030
1	16	1.98 ± 0.21	0.0116 ± 0.0031
1	17	2.03 ± 0.20	0.0124 ± 0.0030
1	18	2.28 ± 0.21	0.0135 ± 0.0029

Tabella 4.5: Fit parameters of the Birks' function for each calibrated bar of the scintillator.

Conclusions

The purpose of the FOOT experiment is to measure the target and projectile fragmentation cross sections relevant for hadrontherapy. The inverse kinematic approach allows to overcome the problem of short range fragment ($\sim \mu\text{m}$) detection in target fragmentation process, however, proton-induced fragmentations cannot be studied with a pure hydrogen target, since its creation and handling would be difficult. A subtraction method can solve this problem, allowing us to obtain cross section values concerning a H target by exploiting the difference between the cross section measurements performed on C_2H_4 and C targets.

The FOOT electronic setup is the object of this thesis: it consists of a Start Counter, a Beam Monitor, a high precision tracking system in a magnetic field, a time of flight measurement system, and a calorimeter. The MC data analysis shows the excellent capability of this setup in detecting and identifying fragments: the charge Z can be identified with a resolution between 2.7% (for heavy fragments) and 5.7% (for the lighter ones); thanks to the redundancy of mass measurements and the χ^2 -fit method, the mass can be identified with a resolution between 3% and 5%, sufficient for isotopic identification of the fragments. An analysis performed on a MC sample has highlighted the capability of FOOT to measure differential and total cross section of the produced fragments: the precision reached on the cross sections related to C and C_2H_4 targets allowed to obtain also differential and total cross sections concerning a hydrogen target by subtraction. Both the energy differential cross sections and the total cross section for each considered target result in agreement with the theoretical cross sections used in the MC simulation, proving that the all analysis chain correctly works.

A first data taking was performed at the GSI accelerator (Darmstadt) on April 2019.

In particular, an analysis performed on the scintillator proved its capability in performing energy loss measurements with the same resolution expected from the simulation ($\sim 4\%$) and, together with the Start Counter, time of flight measurements with even better precision (80 – 90 ps against the expected 100 ps). By combining these two measures it has been possible to reconstruct the charge Z of the oxygen beam with a resolution of 2%.

Data on fragmentation events, produced by using a 400 MeV ^{16}O beam impinging on a C target, have been also acquired at GSI. Thanks to the the calibration of the scintillator bars performed at CNAO with several proton and carbon beams with different energy, the true energy loss of the fragments produced in the GSI run has been determined. With this calibration it has been possible, for the first time in FOOT, to reconstruct the charge Z of the produced fragments.

The near future goals include completing the electronic setup so as to be able to perform also the measurements needed for the mass reconstruction, which is fundamental for the identification of the fragments and for the measure of the cross section. New data taking are planned for the next years at various facility, in order to investigate several fragmentation processes with different beams, energy and targets.

Appendice A

General information about cross section

Supposing to have a uniform density beam composed of N_{prim} particle impinging with velocity v on a stationary target having a differential thickness dz , area S and differential volume $dV = S \cdot dz$, the number of interactions of the considered type dN_f that occur in the time interval dt is proportional to the flux of projectile particles on the target ($\Phi_{\text{prim}} = n_{\text{prim}} \cdot v$, where n_{prim} is the number of beam particles per unit volume), to the target surface, and to the target particle density n_t :

$$dN_f = \Phi_{\text{prim}} \cdot n_t \cdot \sigma_f \cdot dV dt \quad (\text{A.1})$$

where n_t is given by

$$n_t = \frac{N_A \rho_t}{A_t} \quad (\text{A.2})$$

where $N_A = 6.022 \times 10^{23} \text{ mol}^{-1}$ is the Avogadro's number, ρ_t is the target density in g/cm^3 and A_t is the atomic weight of the target. The proportionality constant σ_f is called *cross section* and it refers to the examined process f . The cross section can be considered as the total interaction area of the target particles when the projectile particles hit the unitary area of the target; it is, therefore, linked to probability that the process f occurs.

If, instead of considering all the interactions, we consider only those that produce particles with energy between E and $E + dE$, the proportionality constant becomes the energy differential cross section, which expresses the probability that an interaction occurs with the emission of a particle of energy E :

$$\frac{dN_f(E)}{dE} = \Phi_{\text{prim}} \cdot n_t \cdot \frac{d\sigma_f}{dE} \cdot dV dt \quad (\text{A.3})$$

Eq. A.3 can be rewritten as

$$\frac{dN_f(E)}{dE} = I_{\text{prim}} \cdot n_t \cdot \frac{d\sigma_f(E)}{dE} \cdot dz dt \quad (\text{A.4})$$

where $I_{\text{prim}} = \Phi_{\text{prim}} \cdot S$ is the number of beam particles impinging on the target per second. Integrating in dz and dt and making the differential cross section explicit, we finally obtain

$$\frac{d\sigma_f(E)}{dE} = \frac{dN_f(E)}{dE \cdot N_{\text{prim}} \cdot n_t \cdot d} \quad (\text{A.5})$$

where d is the total thickness of the target.

In an experimental context, the number of processes N_f as a function of the energy of the produced particle E can be measured as

$$N_f(E) = \frac{Y_f(E) - B_f(E)}{\epsilon} \quad (\text{A.6})$$

where $Y_f(E)$ is the experimental yield, $B_f(E)$ is the number of background events and ϵ is the detection and reconstruction efficiency. Considering that, instead of into an energy differential dE , the differential cross section is evaluated into a discrete energy range ($dE = \Omega_E$), we can find eq. 3.18 from eq. A.5.

Appendice B

Analysis of data from ^{16}O (200 MeV/u)
on C target

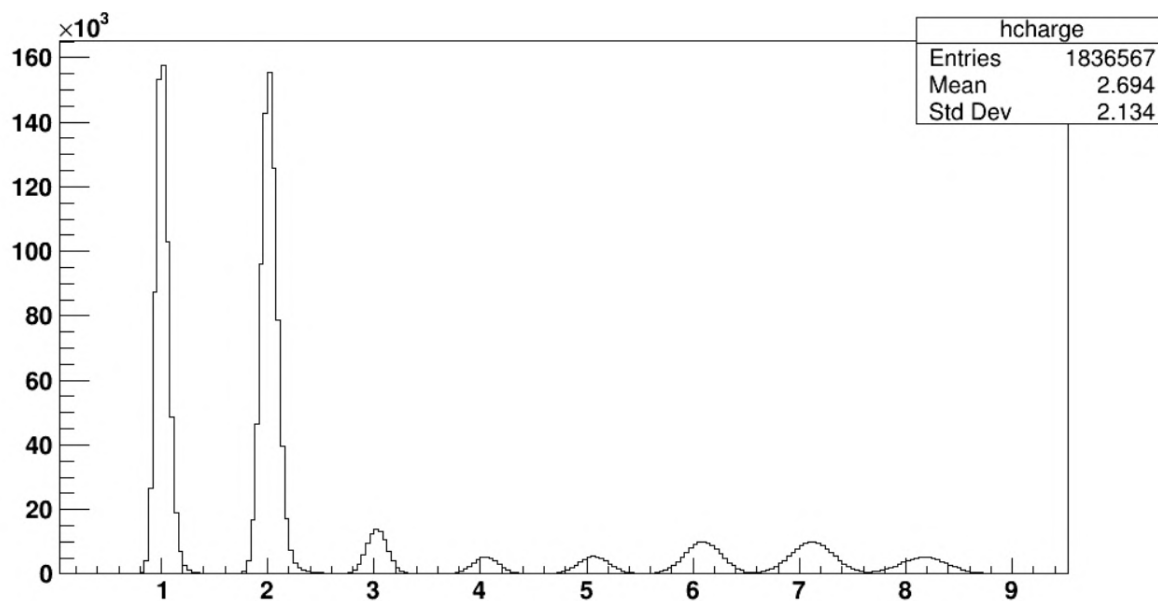
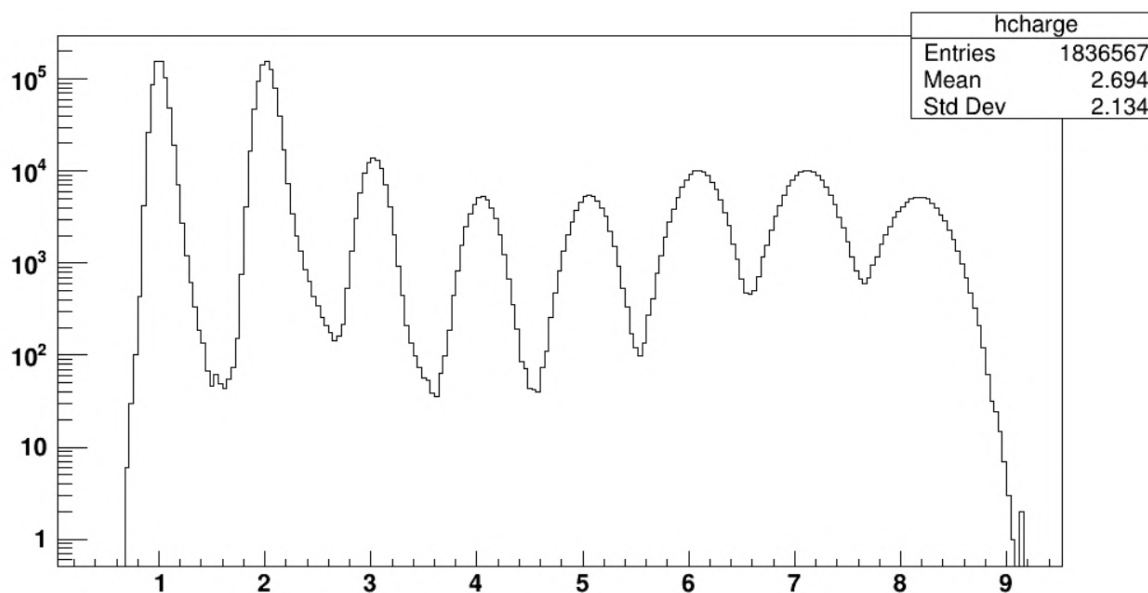


Figure B.1: Charge Z distributions of fragments produced in the fragmentation.

Figure B.2: Charge Z distributions of fragments produced in the fragmentation in logarithmic y scale.

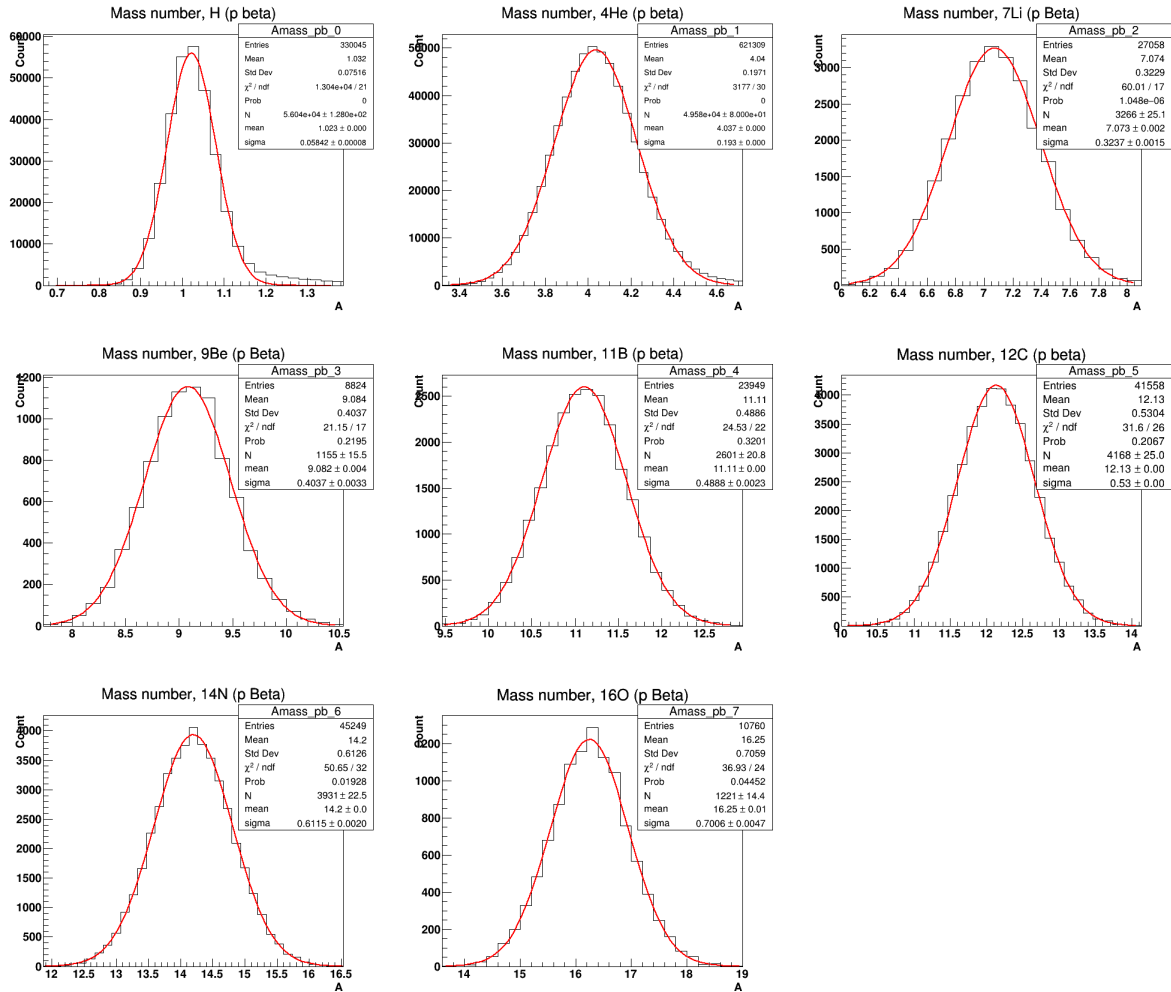


Figure B.3: Mass numbers A_1 from 1 to 16 reconstructed with the ToF and momentum measurement.

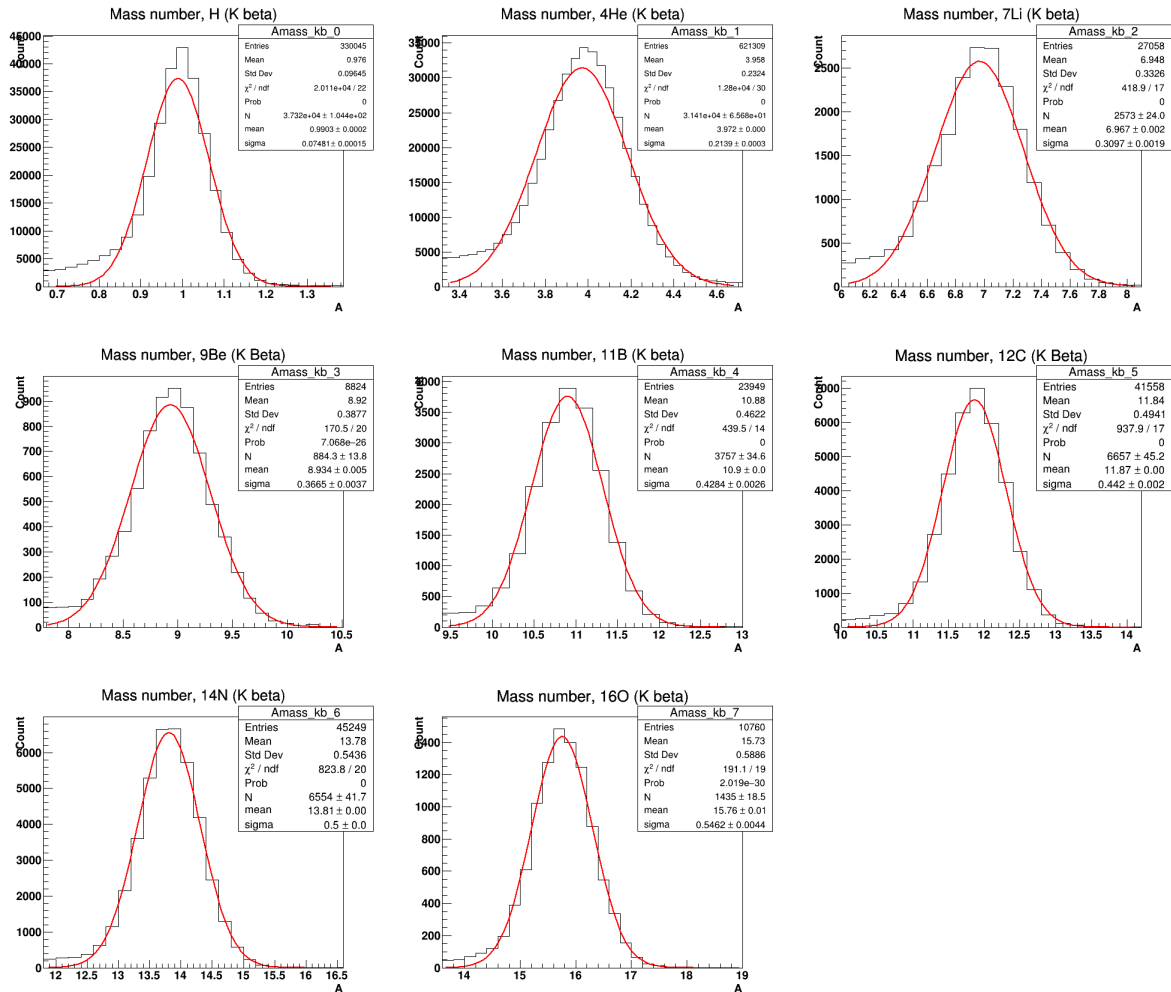


Figure B.4: Mass numbers A_2 from 1 to 16 reconstructed with the kinetic energy and momentum measurement.

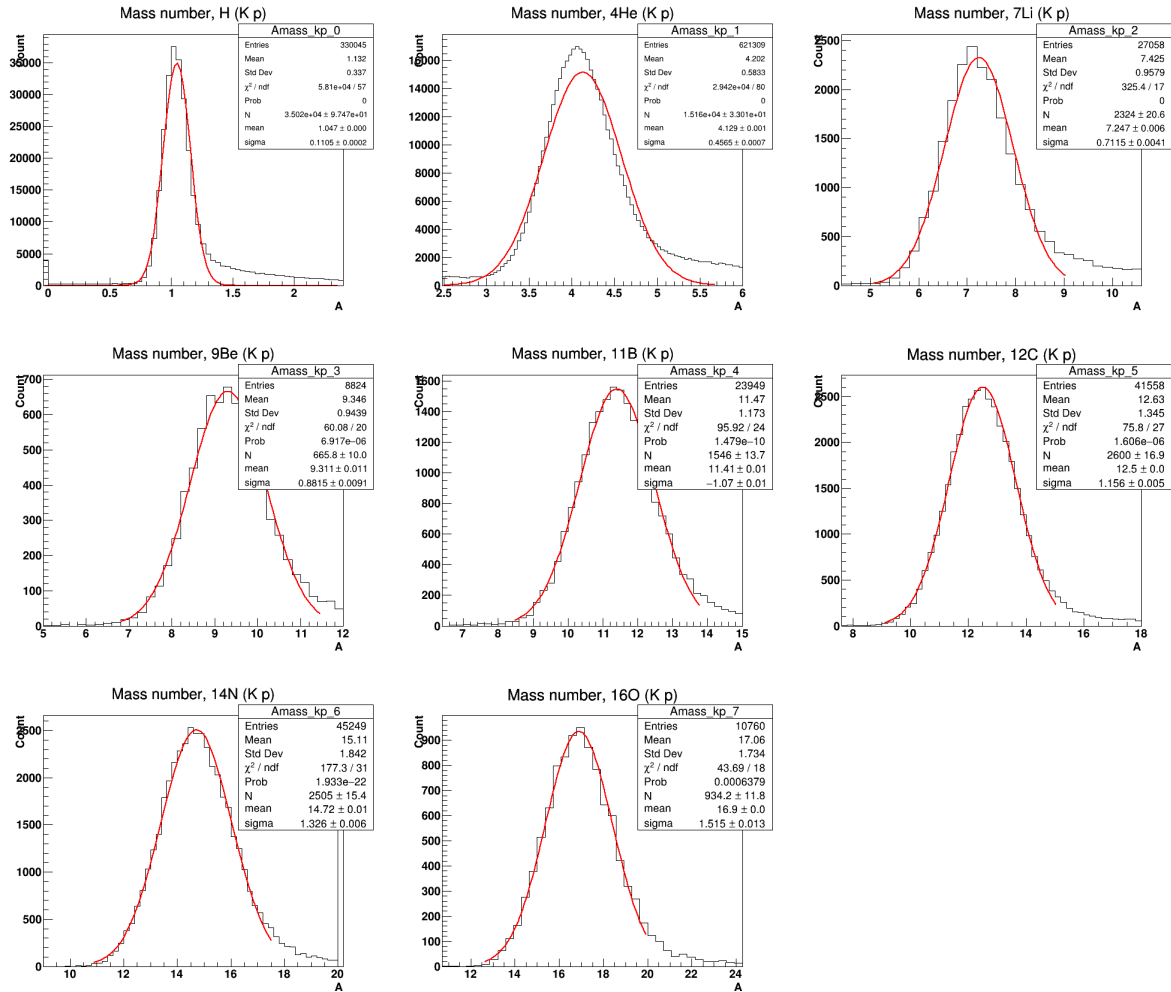


Figure B.5: Mass numbers A_3 from 1 to 16 reconstructed with the ToF and kinetic energy.

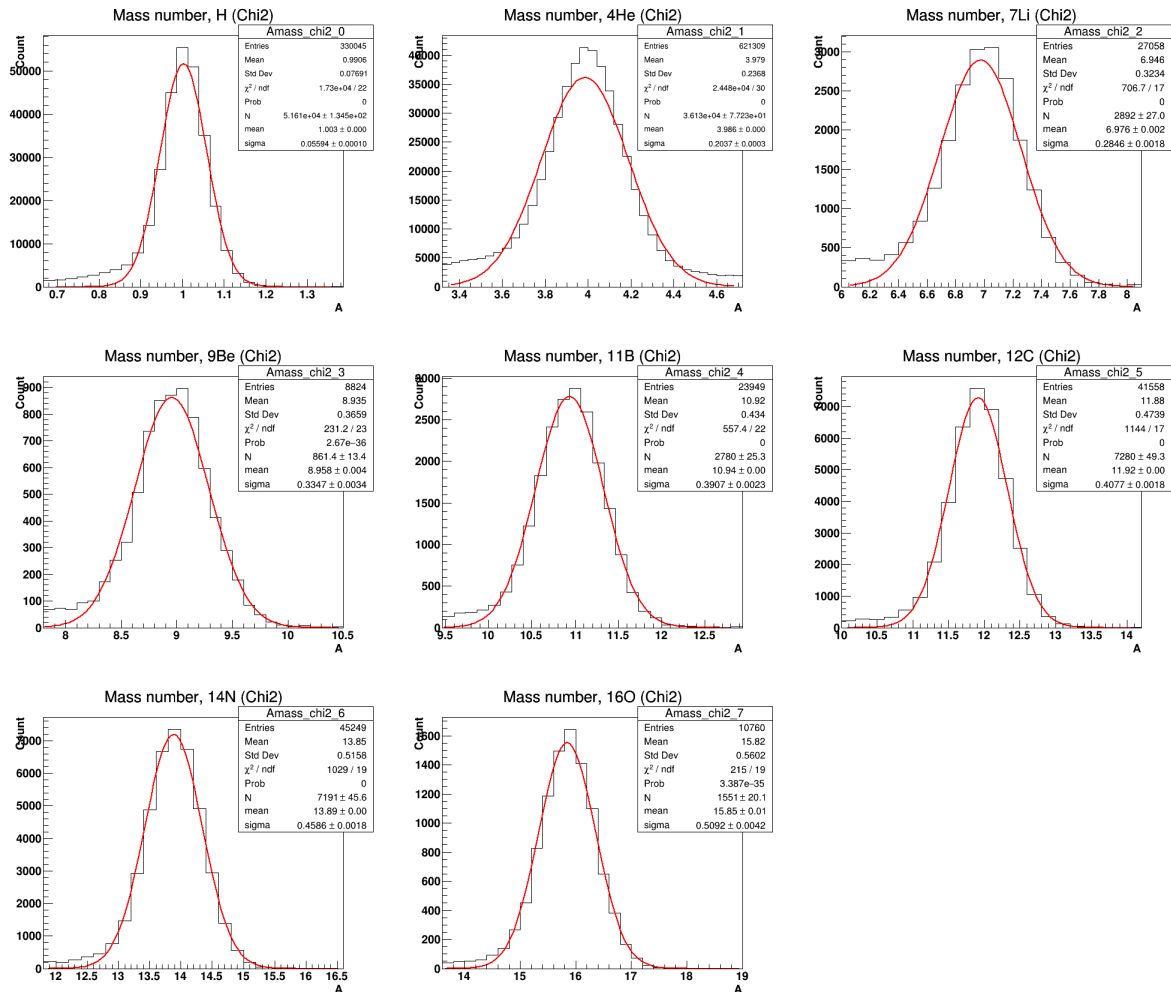


Figure B.6: Mass number distributions obtained with the standard χ^2 minimization method.

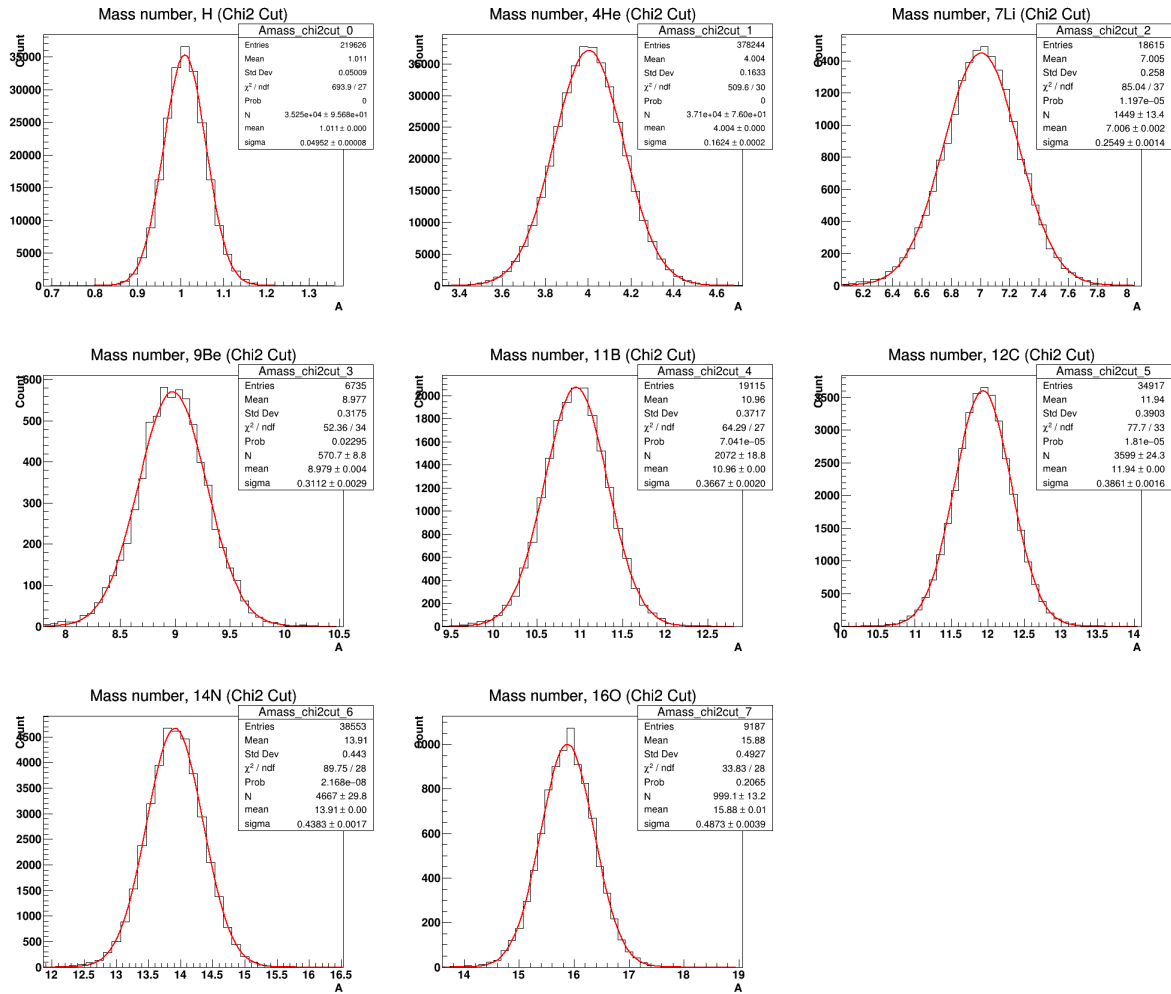


Figure B.7: Cutted distributions ($\chi^2 < 5$ events only) of the mass number obtained with the standard χ^2 minimization method.

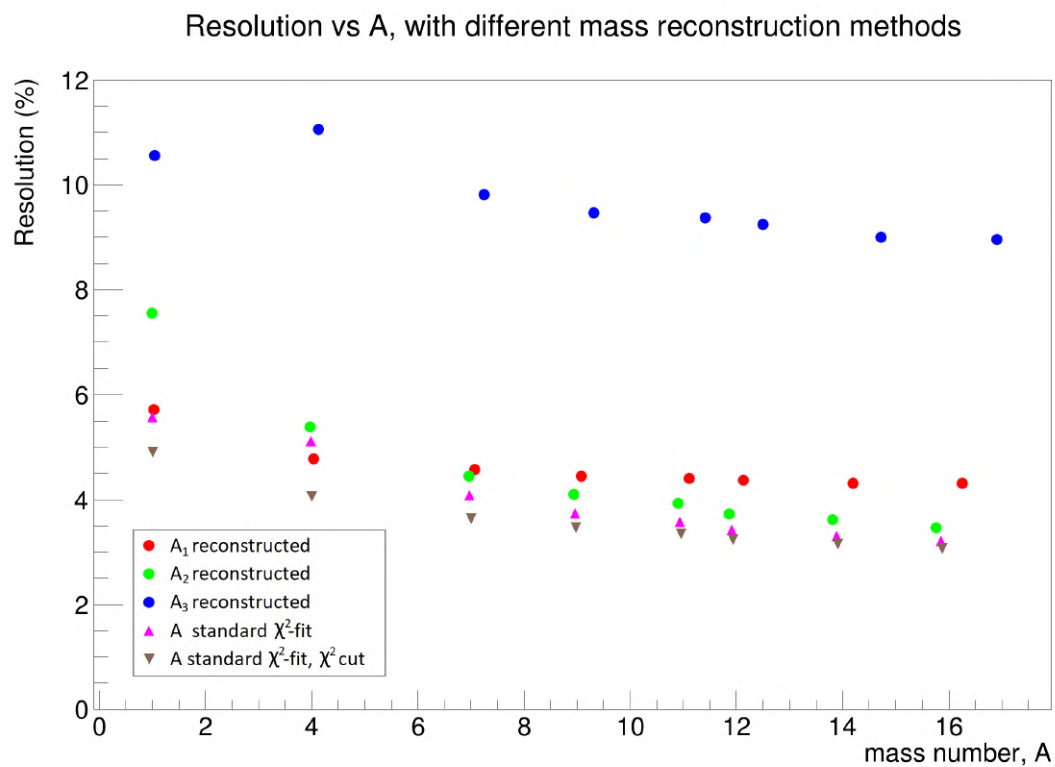


Figure B.8: Mass resolution as a function of the mass number obtained with different mass reconstruction methods.

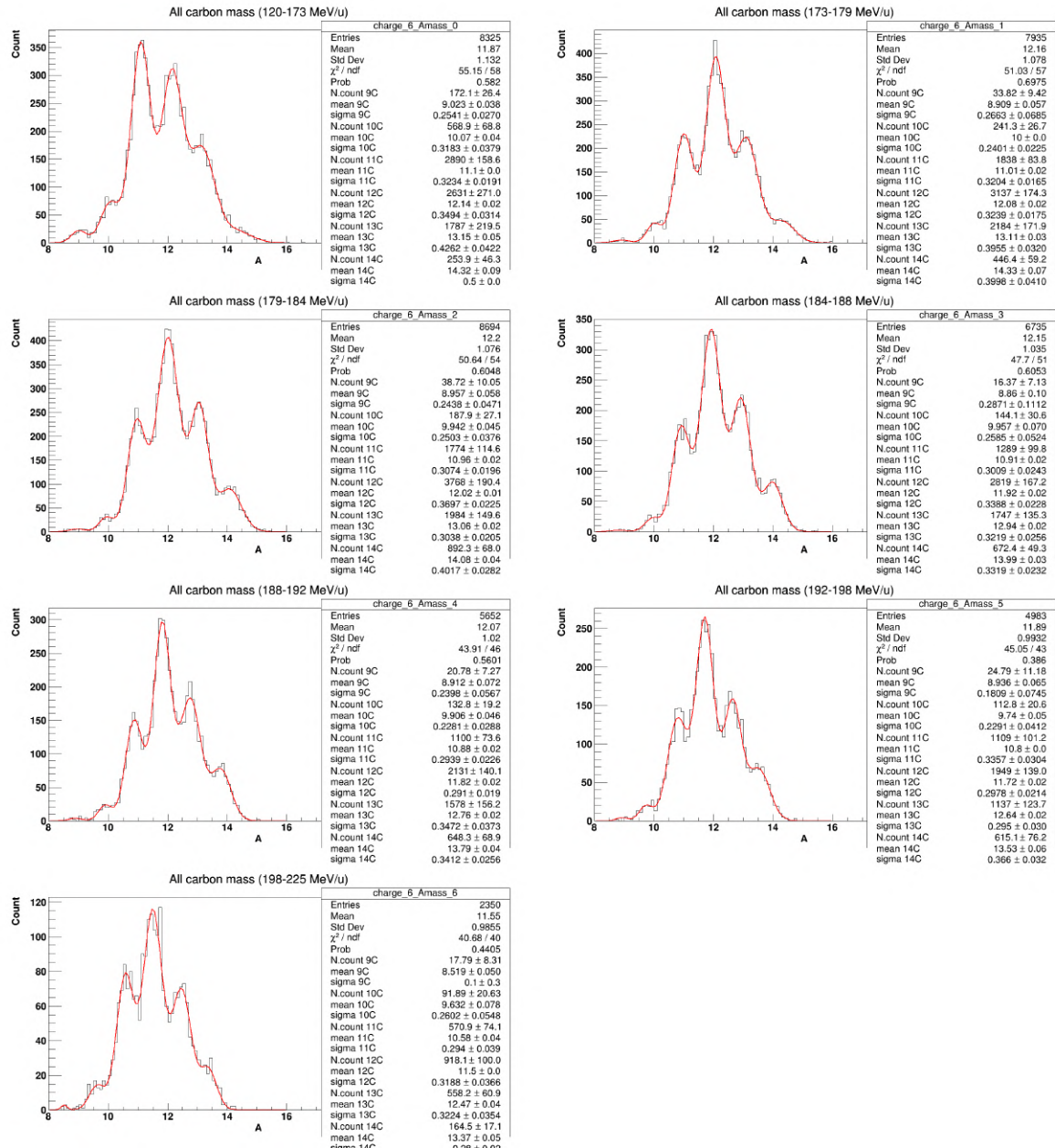


Figure B.9: Mass distributions of carbon fragments in different kinetic energy range.

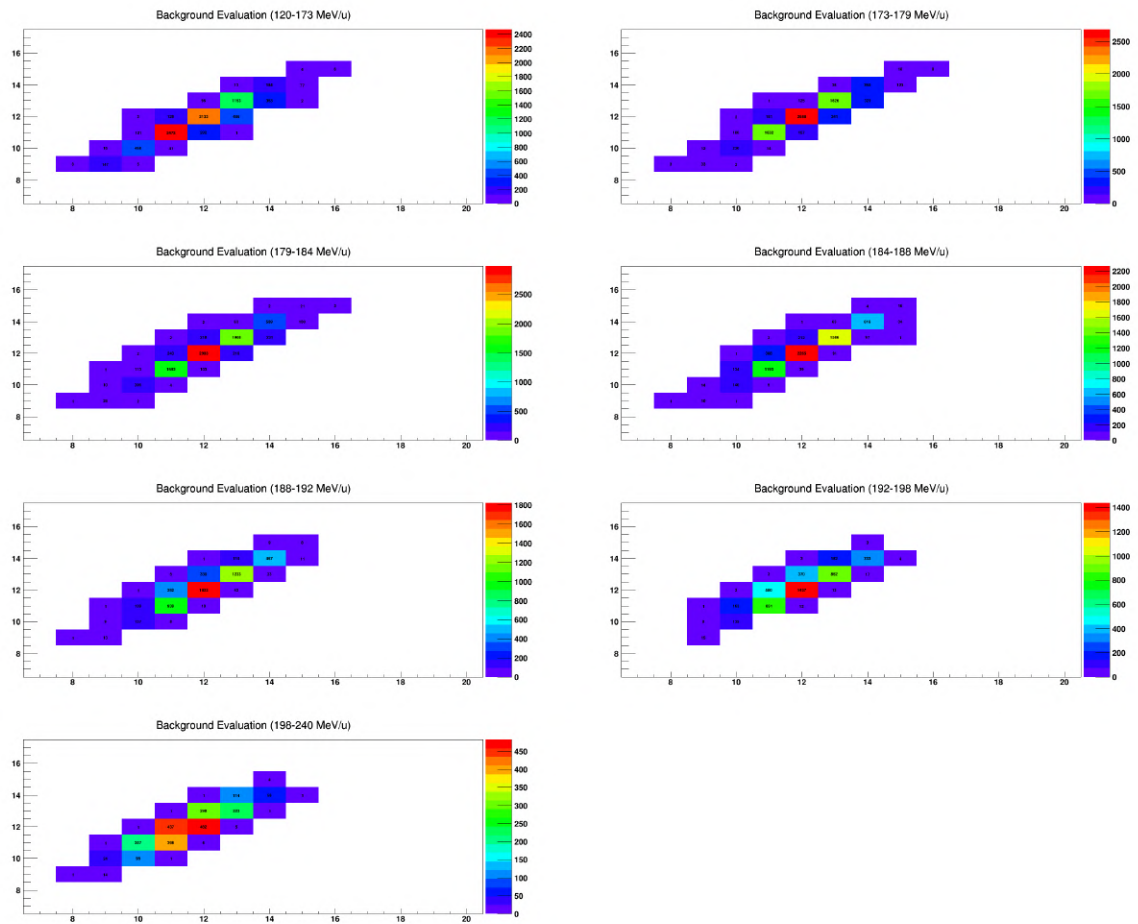


Figure B.10: Migration histograms for the background evaluation of carbon fragments indifferent energy ranges: true mass number A vs reconstructed mass number A .

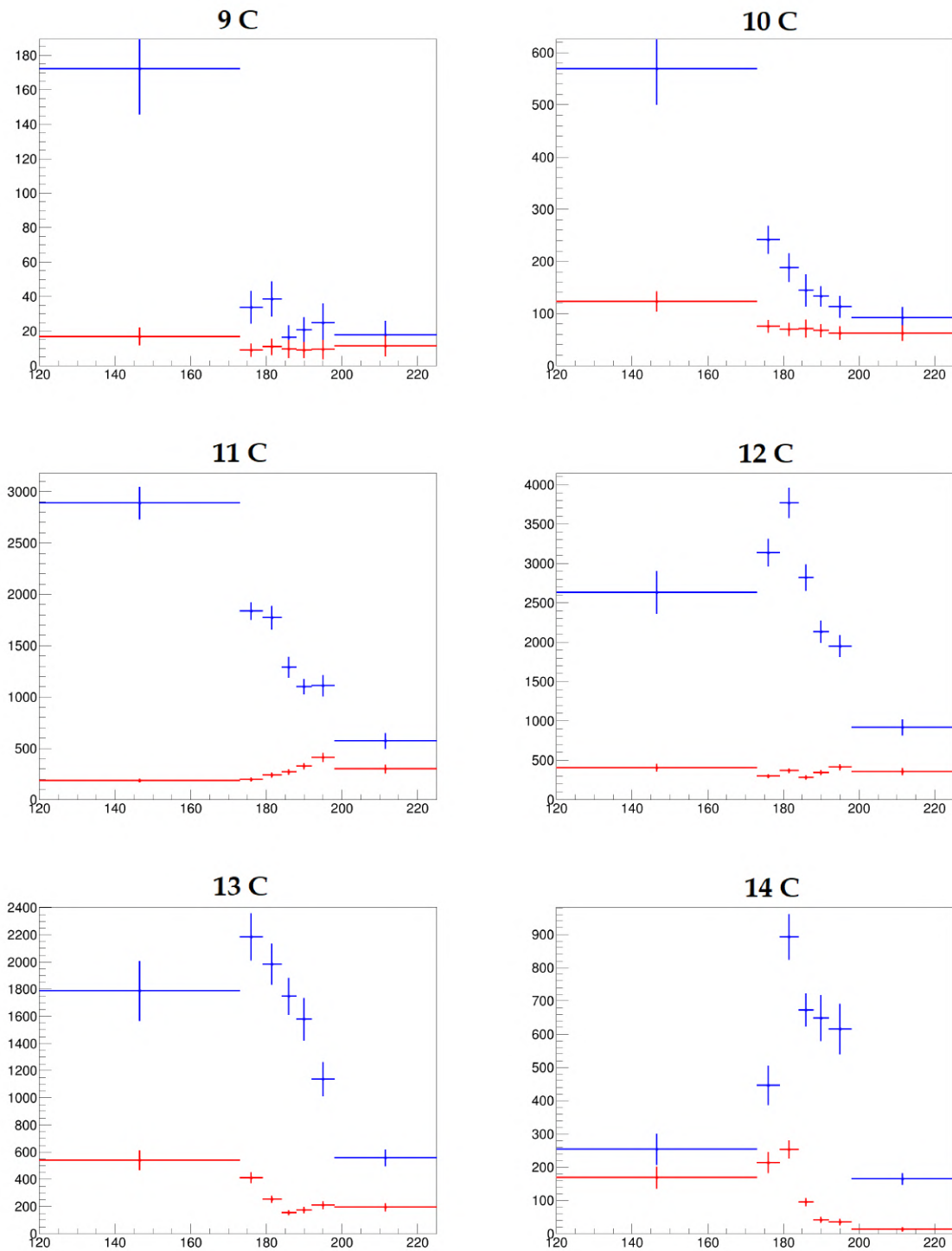


Figure B.11: Production yields (blue lines) and background events (red lines) as a function of kinetic energy (MeV/u) of carbon isotopes.

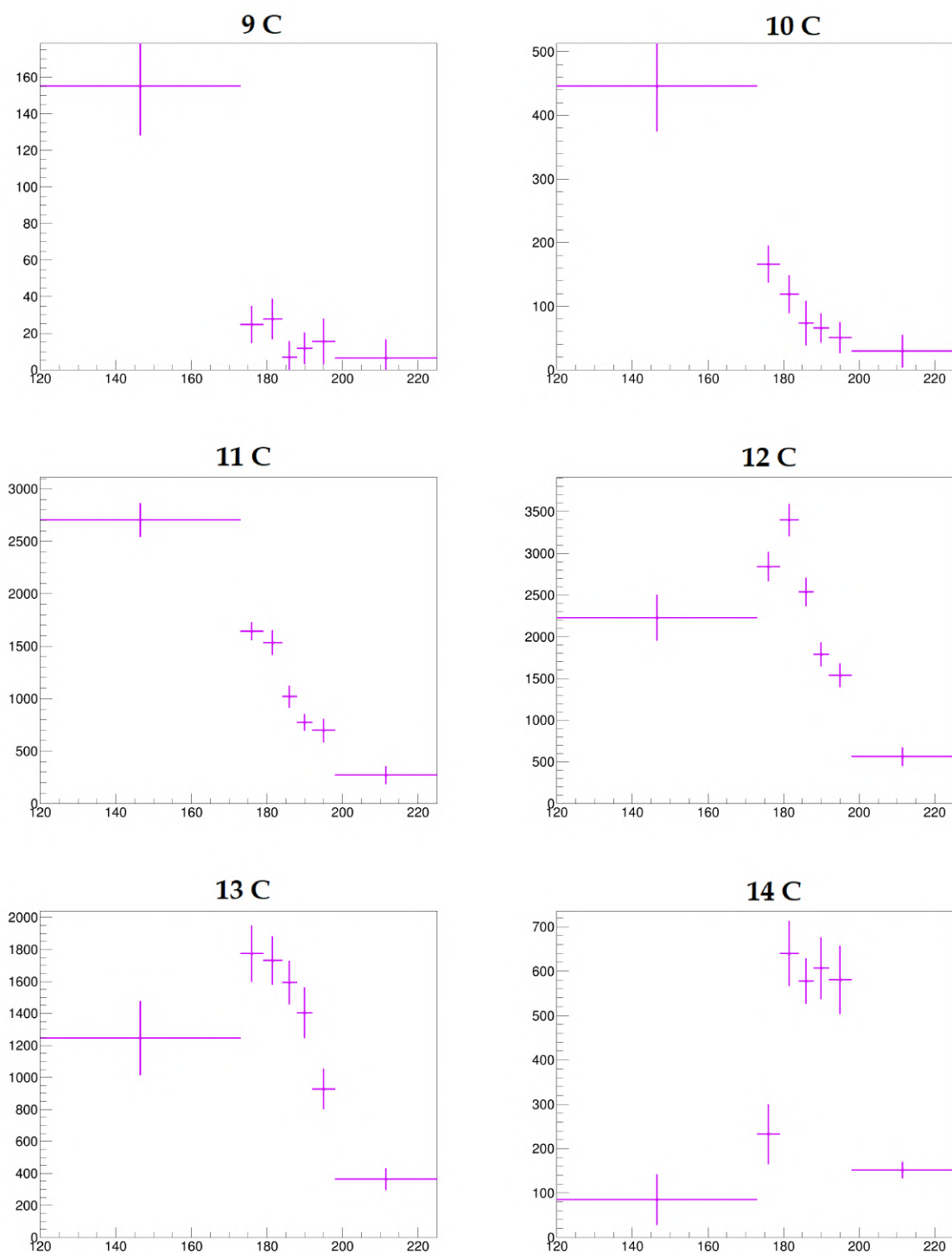


Figure B.12: Production yields background subtracted as a function of kinetic energy (MeV/u) of carbon isotopes.

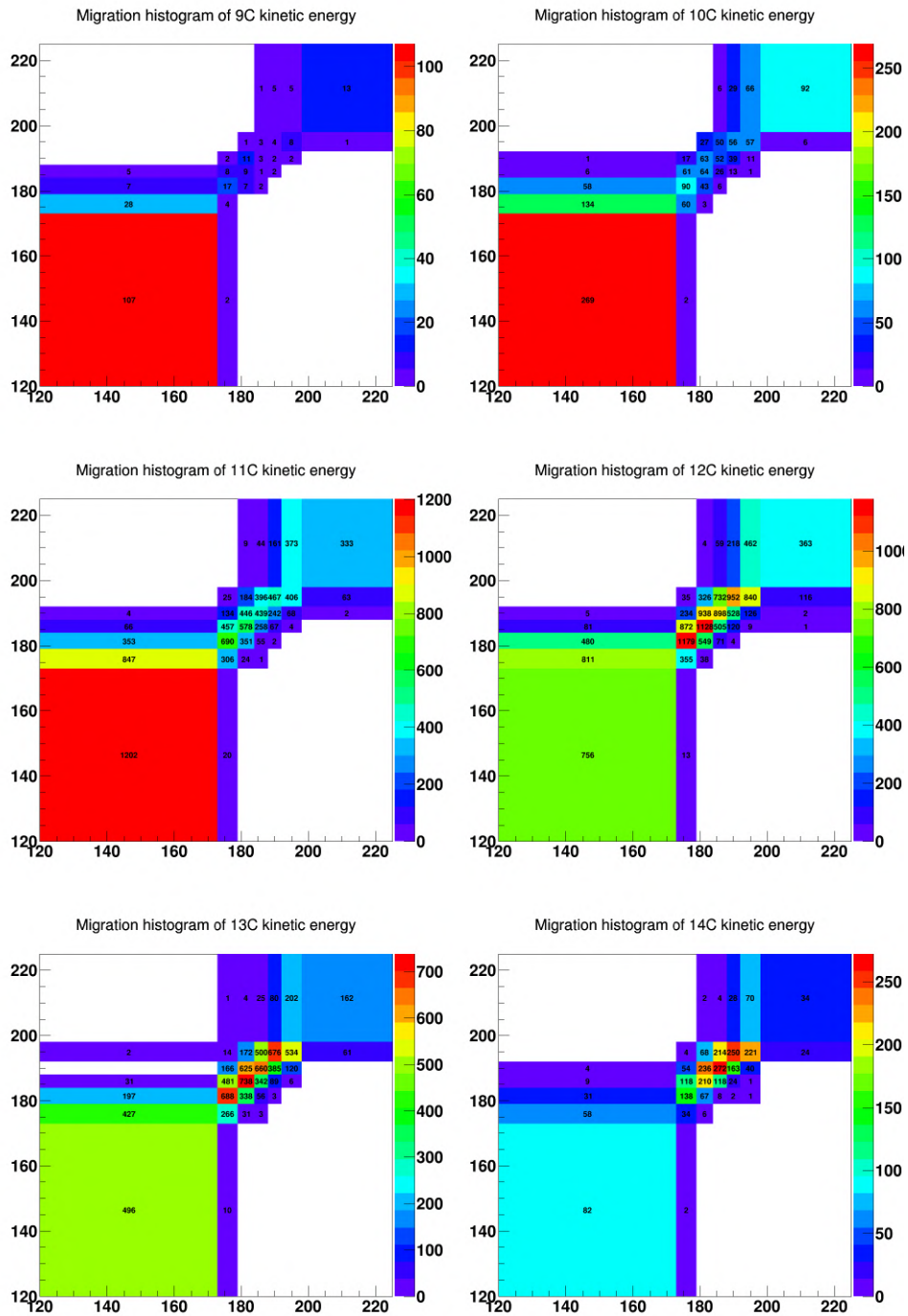


Figura B.13: Migration histograms of kinetic energy (MeV) used in the unfolding procedure: true kinetic energy vs reconstructed kinetic energy.

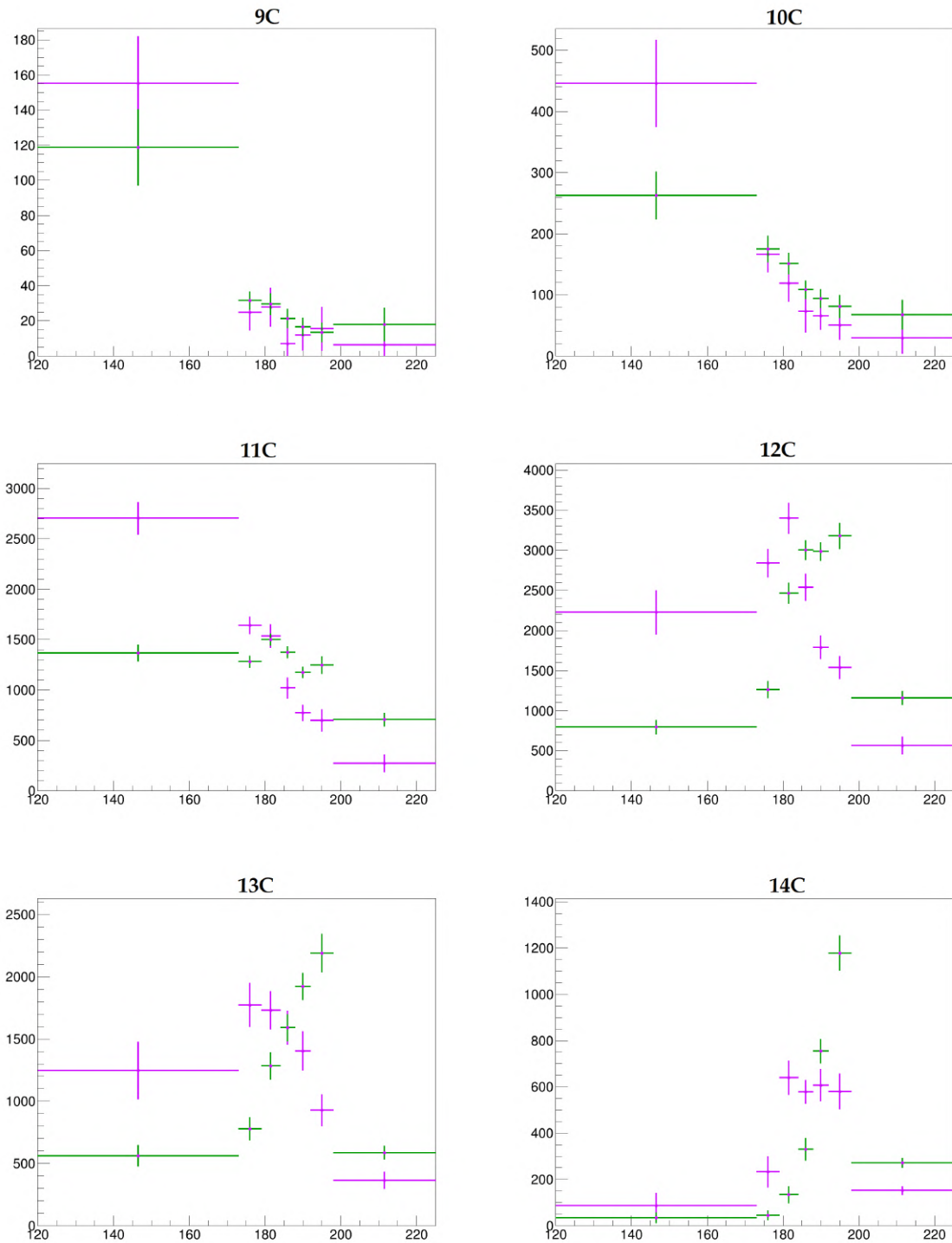


Figure B.14: Production yields background subtracted before (violet lines) and after (green lines) the unfolding procedure as a function of kinetic energy (MeV/u) of carbon isotopes.

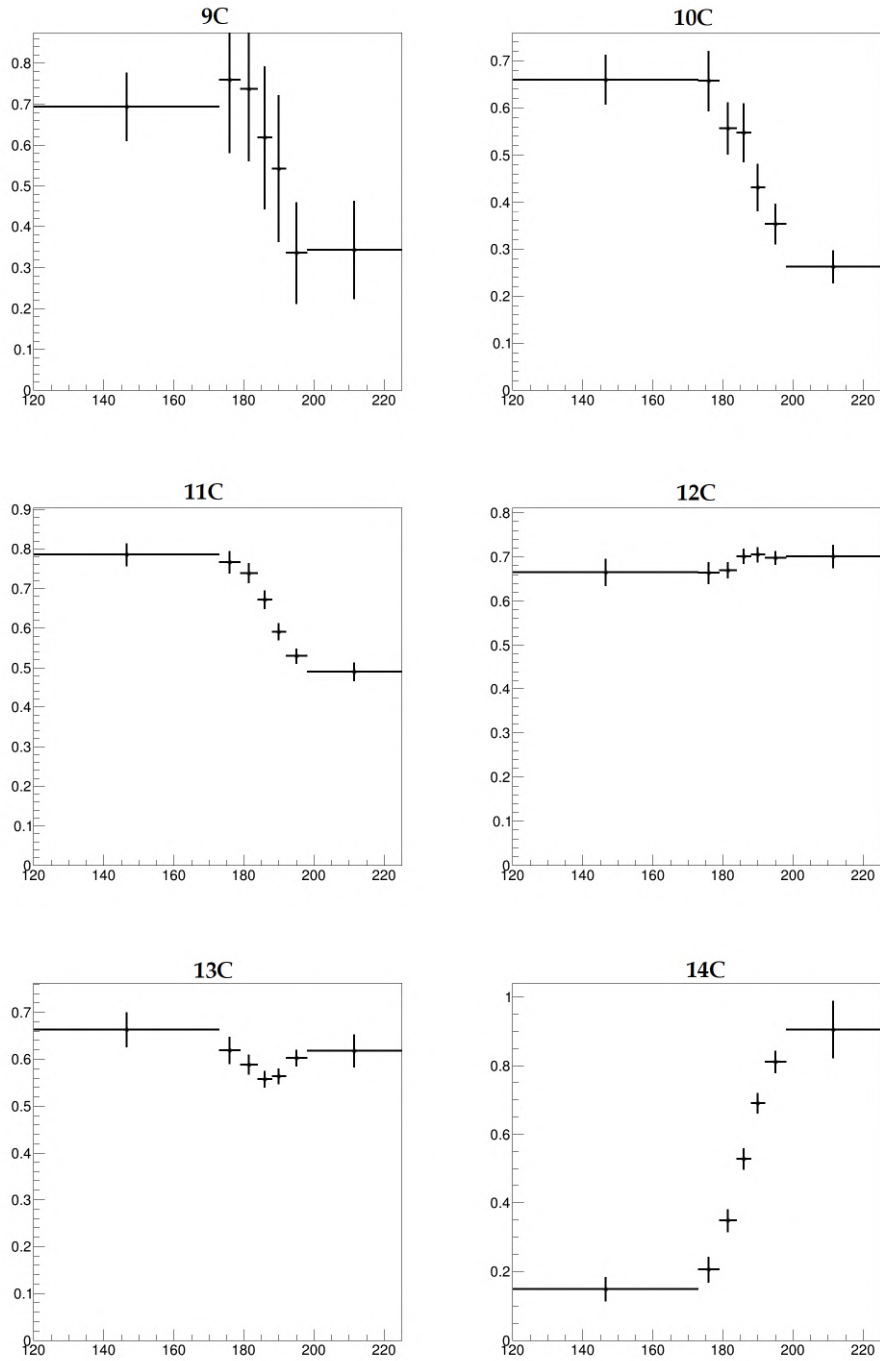


Figura B.15: Reconstruction efficiency as a function of kinetic energy (MeV/u) of each carbon isotope.

Appendice C

Comparison of differential cross sections and FLUKA differential cross sections

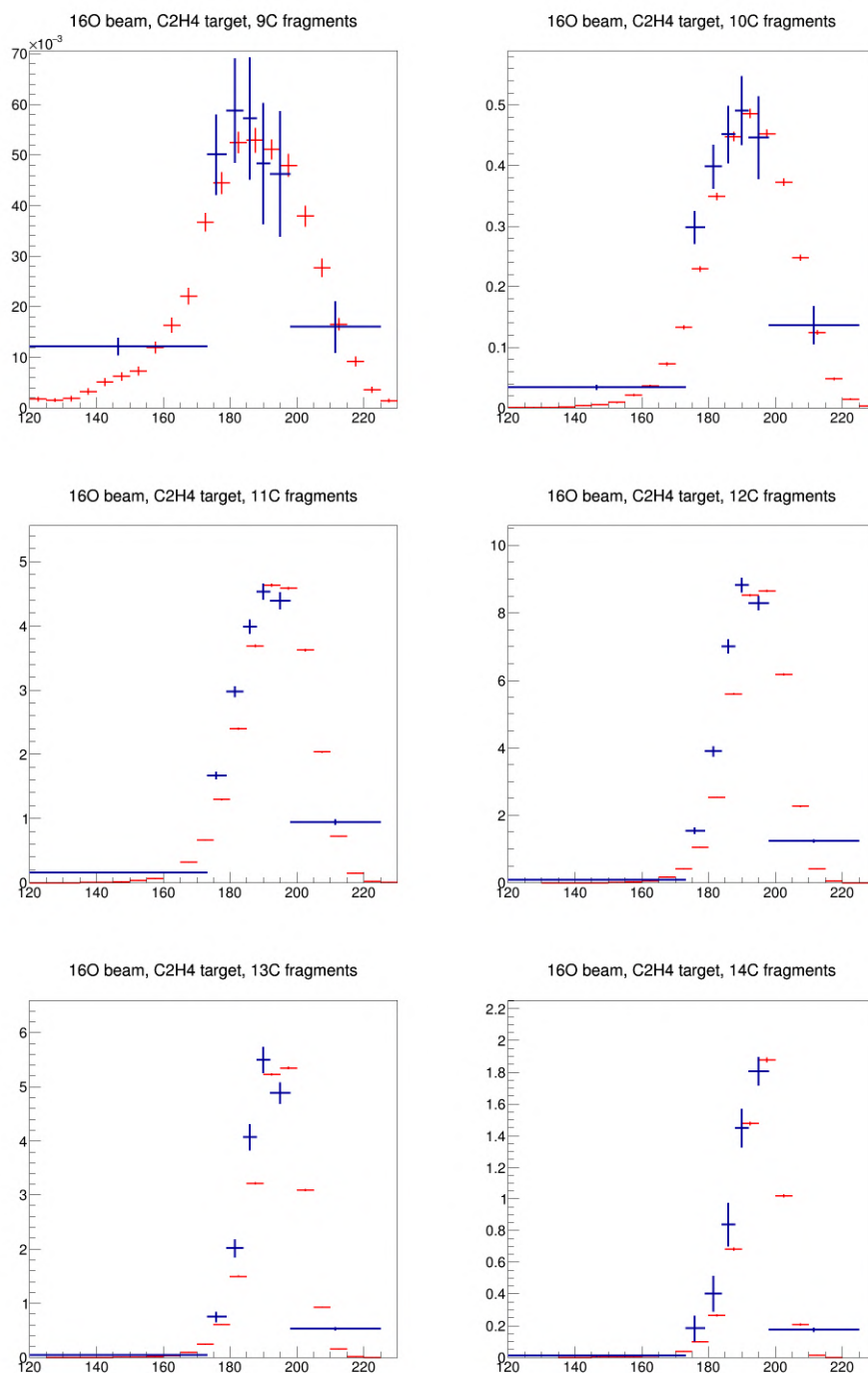


Figura C.1: Differential cross section (mbarn/MeV) as a function of kinetic energy (MeV/u). The blue markers are the differential cross section found in this analysis, the red markers are the differential cross sections used in the FLUKA simulation. The plots refer to the carbon isotopes produced by an oxygen-16 beam (200 MeV/u) impinging on a C₂H₄ target.

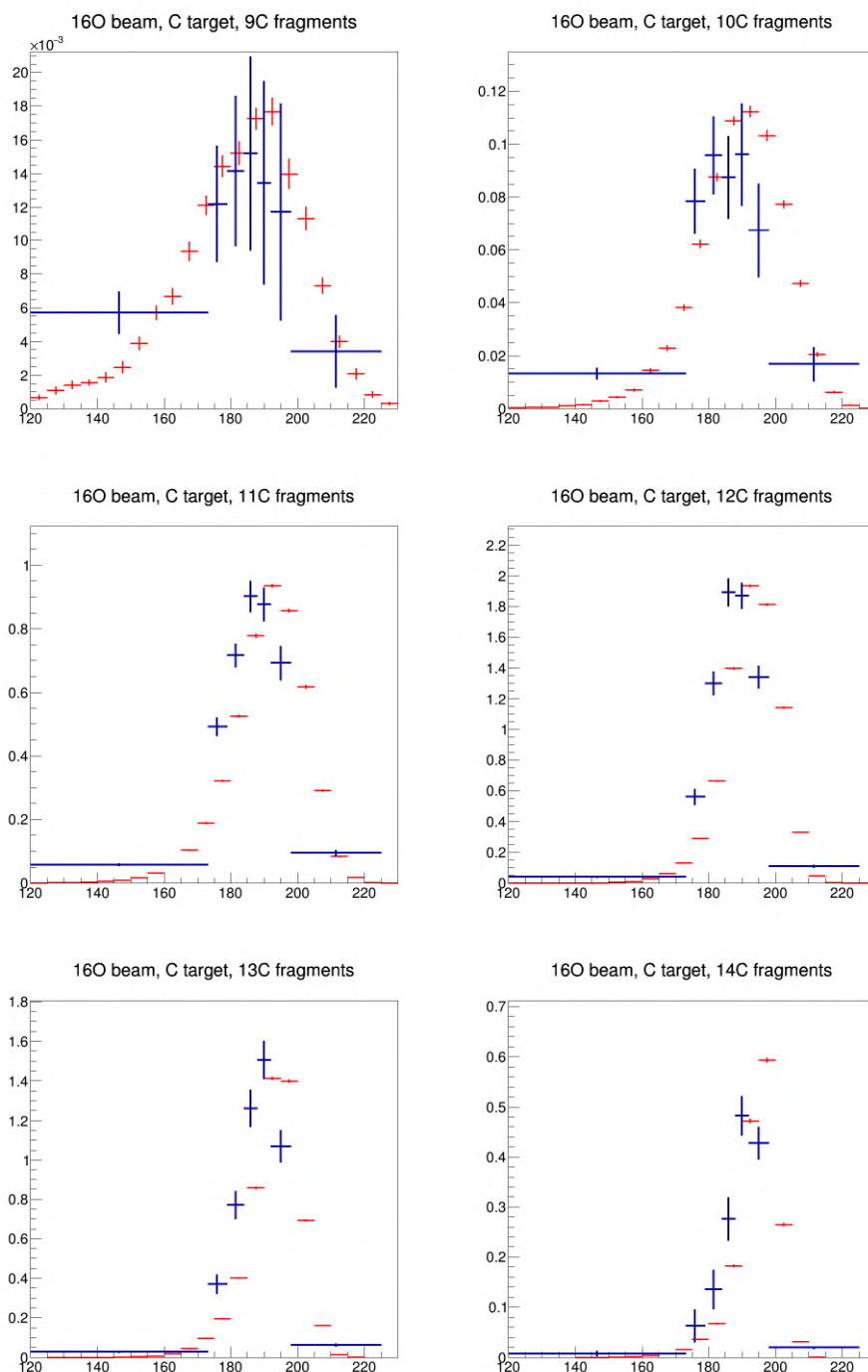


Figura C.2: Differential cross section (mbarn/MeV) as a function of kinetic energy (MeV/u). The blue markers are the differential cross section found in this analysis, the red markers are the differential cross sections used in the FLUKA simulation. The plots refer to the carbon isotopes produced by an oxygen-16 beam (200 MeV/u) impinging on a C target.

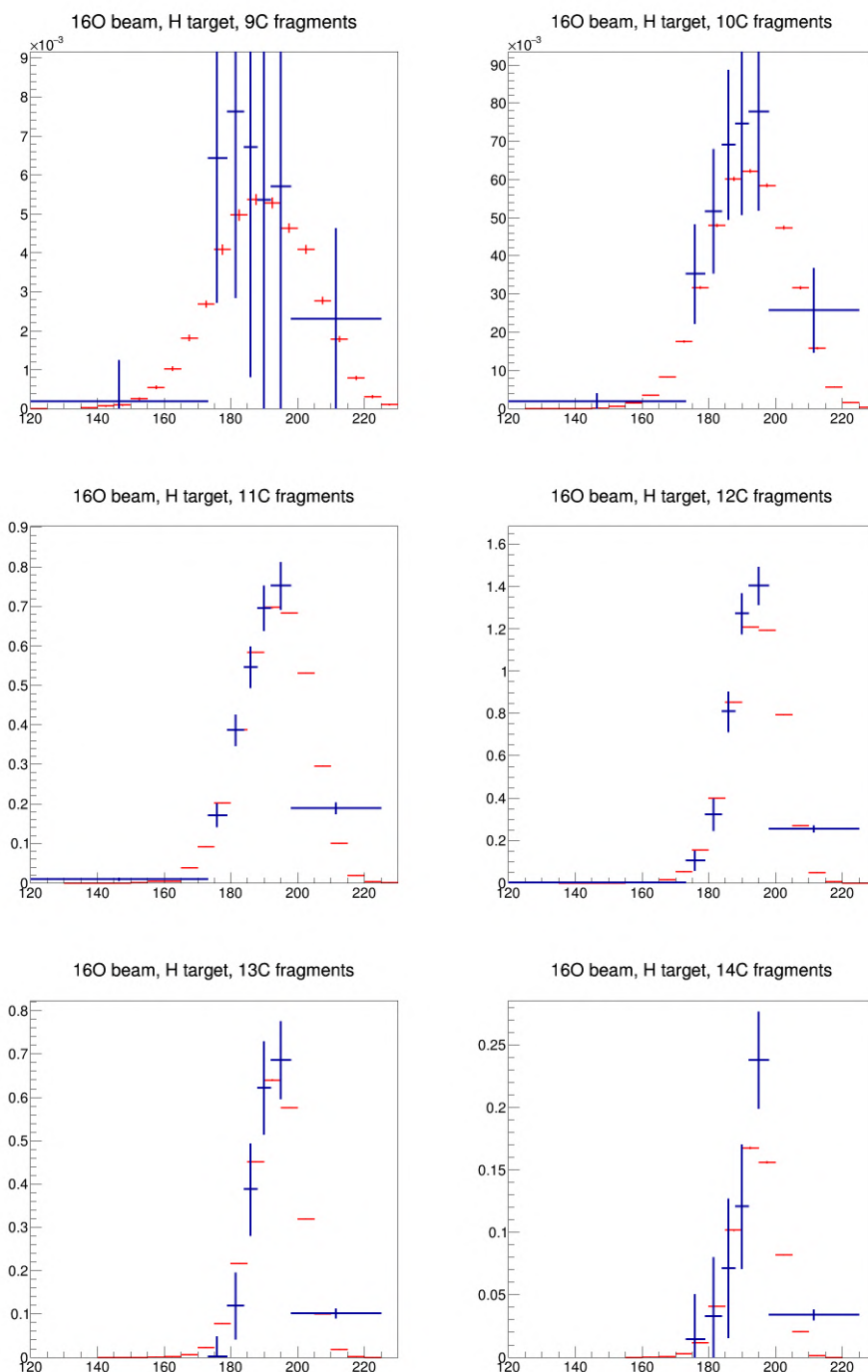


Figura C.3: Differential cross section (mbarn/MeV) as a function of kinetic energy (MeV/u). The blue markers are the differential cross section found in this analysis, the red markers are the differential cross sections used in the FLUKA simulation. The plots refer to the carbon isotopes produced by an oxygen-16 beam (200 MeV/u) impinging on a H target.

Bibliografia

- [1] E. B. Podgorsak, *Radiation in Physics for Medical Physicists*, Springer (2016).
- [2] N. Bohr, *The Penetration of Atomic Particles Through Matter*, Hafner Publishing Company (1948).
- [3] H. A. Bethe, *Zur Theorie des Durchgangs schneller Korpuskularstrahlen durch Materie*, Ann. Physik 5, 325 (1930).
- [4] F. Bloch, *Zur Bremsung rasch bewegter Teilchen beim Durchgang durch Materie*, Ann. Physik 16, 285 (1930).
- [5] Grdanovska, Slavica, *Characterization of Radiation Damage to a Novel Photonic Crystal Sensor*, 10.13016/M2BZ0D (2015).
- [6] W. Bragg, R. Kleeman, *On the alpha particles of radium and their loss of range in passing through various atoms and molecules*, Phil. Mag. 10, 318–40 (1905).
- [7] D. Schardt et al., *Heavy-ion tumor therapy: physical and radiobiological benefits*, Rev. Mod. Phys., 82(1), 383 (2010).
- [8] G. F. Knoll, *Radiation Detection and Measurement*, John Wiley & Sons, p.41 (2000).
- [9] W. Ulmer, E. Matsinos, *Theoretical methods for the calculation of Bragg curves and 3D distributions of proton beams*, The European Physical Journal Special Topics, Volume 190, Issue 1, pp 1-81 (2010).
- [10] K. S. Krane, *Introductory Nuclear Physics*, John Wiley & Sons (1988).
- [11] C. A. Bertulani, *Nuclear Reactions*, Wiley Encyclopedia of Physics (2010).

- [12] R. Serber, *Nuclear reactions at high energies*, Phys. Rev., 72, 1114-5 (1947).
- [13] K. Gunzert-Marx, H. Iwase, D. Schardt and R. S. Simon, *Secondary beam fragments produced by 200 MeV u⁻¹ ¹²C ions in water and their dose contributions in carbon ion radiotherapy*, New Journal of Physics (2008).
- [14] ICRP, *The 2007 Recommendations of the International Commission on Radiological Protection*, Annals of the ICRP Volume 37/2-4, (2008).
- [15] James A. Imlay and Stuart Linn, *NA Damage and Oxygen Radical Toxicity*, Science Vol. 240, No. 4857 (1988).
- [16] M. Valverde et al., *Hydrogen Peroxide-Induced DNA Damage and Repair through the Differentiation of Human Adipose-Derived Mesenchymal Stem Cells*, Stem Cells International (2018).
- [17] Hall E. J. and Hei T. K., *Genomic instability and bystander effects induced by high LET radiation*, Oncogene, 22(45), 7034 (2003).
- [18] Jakel O., *The relative biological effectiveness of proton and ion beams*, Z. Med. Phys., 18(4), 276 – 285 (2008).
- [19] ICRU, *Prescribing, Recording, and Reporting Proton-Beam Therapy*, Report 78 (2007).
- [20] Furusawa Y. et al., *Inactivation of aerobic and hypoxic cells from three different cell lines by accelerated ³He-, ¹²C- and ²⁰Ne-ion beams.*, Radiat. Res., 154(5), 485–496 (2000).
- [21] E. B. Podgorsak, *Review of Radiation Oncology Physics: A Handbook for Teachers and Students* (2005).
- [22] G. W. Barendsen, *The relationships between RBE and LET for different types of lethal damage in mammalian cells: biophysical and molecular mechanisms*, Radiat. Res., 139(3), 257–270 (1994).

- [23] W. Friedland et al., *Simulation of DNA fragment distributions after irradiation with photons*, Radiat. Environ. Bioph., 38(1), 39–47 (1999).
- [24] H. Nikjoo et al., *Quantitative modelling of DNA damage using Monte Carlo track structure method*, Radiat. Environ. Bioph., 38(1), 31–38 (1999).
- [25] E. J. Hall et al., *Radiobiology for the Radiologist*, Vol. 6, Lippincott Williams Wilkins (2006).
- [26] S. C. Short, M. Woodcock, B. Marples, M. C. Joiner, *Effects of cell cycle phase on low-dose hyper-radiosensitivity*, International Journal of Radiation Biology (2003).
- [27] J. Choi, J. O. Kang, *Basics of particle therapy II: relative biological effectiveness*, Radiat. Oncol. J., 30(1), 1 (2012).
- [28] R. Wilson, *Radiological use of fast protons*, Radiology, 47, (487-491) (1946).
- [29] Wayne D. Newhauser and Rui Zhang, *The physics of proton therapy*, Phys. Med. Biol. 60 (2015) R155–R209 (2015).
- [30] W. M. Preston, A. M. Koehler , *Proton beam dosimetry*, Harvard Cyclotron Laboratory, personal communication (1968).
- [31] M. B. Chadwick et al., *ENDF/B-VII.1 Nuclear data for science and technology: cross sections, covariances, fission product yields and decay data*, Nuclear Data Sheets Vol 112 pp 2887–996 (2011).
- [32] *Clinical proton dosimetry: I. beam production, beam delivery, and measurement of absorbed dose*, ICRU Report 59 (1998).
- [33] *The 2007 Recommendations of the International Commission on Radiological Protection*, ICRP publication 103 Ann. ICRP 37 1–332 (2007).
- [34] E. J. Hall, *Intensity-modulated radiation therapy, protons, and the risk of second cancers*, Int. J. Radiat. Oncol. Biol. Phys. 65 1–7 (2006).
- [35] E. J. Hall, D. J. Brenner, *Secondary neutrons in clinical proton radiotherapy: a charged issue*, Radiother. Oncol. 86 165–70 (2008).

- [36] K. Parodi et al., *PET/CT imaging for treatment verification after proton therapy: a study with plastic phantoms and metallic implants*, Med. Phys. 34 419–35 (2007).
- [37] S. W. Peterson, D. Robertson, J. Polf, *Optimizing a three-stage Compton camera for measuring prompt gamma rays emitted during proton radiotherapy*, Phys. Med. Biol. 55 6841–56 (2010).
- [38] C. H. Min et al., *Development of array-type prompt gamma measurement system for in vivo range verification in proton therapy*, Med. Phys. 39 2100–7 (2012).
- [39] J. S. Kim et al., *New concept of a range verification system for proton therapy using a photon counting detector*, Nucl. Instrum. Methods A 677 18–21 (2012).
- [40] P. V. Vavilov, *Ionization losses of high-energy heavy particles*, Sov. Phys. JETP 5 749–51 (1957).
- [41] B. Rossi, *High-Energy Particles*, Prentice-Hall Physics Series (1952).
- [42] Molière, *Theorie der streuung schneller geladener teilchen II, mehrfach-und vielfachstreuung*, Z. Naturforsch. A 3A, 78–97. (1948).
- [43] V. L. Highland, *Some practical remarks on multiple scattering*, Nucl. Instrum. Methods Phys. Res. 129, 497–499 (1975).
- [44] Y. S. Tsai, *Pair production and bremsstrahlung of charged leptons*, Rev. Mod. Phys. 46, 815–851 (1974).
- [45] J. Hüfner, *Heavy fragments produced in protonnucleus and nucleus-nucleus collisions at relativistic energies*, Phys. Rep. 125, 129–185 (1985).
- [46] W. G. Lynch, *Nuclear fragmentation in proton- and heavy-ion-induced reactions*, Annu. Rev. Nucl. Part. Sci. 37, 493–535 (1987).
- [47] E. M. Friedländer, H. H. Heckmann, *Relativistic heavy-ion collisions: experiments*, Treatise on Heavy-Ion Science, edited by D. A. Bromley, Vol. 4, pp. 403–562 (1985).
- [48] M. Golovkov et al., *Fragmentation of 270 A MeV carbon ions in water*, Advances in Hadrontherapy, International Congress Series No. 1144, pp. 316–324 (1997).

- [49] N. Matsufuji et al., *Spatial fragment distribution from a therapeutic pencil-like carbon beam in water*, Phys. Med. Biol. 50, 3393–3403 (2005).
- [50] I. Schall et al., *Charge-changing nuclear reactions of relativistic light-ion beams ($5 \leq Z \leq 10$) passing through thick absorbers*, Nucl. Instrum. Methods Phys. Res. B 117, 221–234 (1996).
- [51] D. Schardt et al., *Precision Bragg-curve measurements for light ion beams in water*, GSI-Report 2008, p. 373 (2008).
- [52] L. Sihver et al., *Depth-dose distributions of high-energy carbon, oxygen and neon beams in water*, Jpn. J. Med. Physics 18, 1–21 (1998).
- [53] K. Gunzert-Marx et al., *Secondary beam fragments produced by 200 MeV/u ^{12}C ions in water and their dose contributions in carbon ion radiotherapy*, New J. Phys. 10, 075003 (2008).
- [54] R. Henderson, *The potential and limitations of neutrons, electrons and X-rays for atomic resolution microscopy of unstained biological molecules*, Quarterly reviews of biophysics (1995).
- [55] F. A. Dilmanian et al., *Charged Particle Therapy with Mini-Segmented Beams*, Frontiers in Oncology, Vol. 5 (2015).
- [56] F. M. Khan, *The Physics of radiation therapy*, 3rd edion, Lippincott Williams & Wilkins (2003).
- [57] K. R. Hogstrom, P. R. Almond, *Review of electron beam therapy physics*, Physics in Medicine & Biology, Vol. 51, N. 13 (2006).
- [58] R. F. Barth et al., *Boron Neutron Capture Therapy of Cancer: Current Status and Future Prospects*, Clin. Cancer Res., 11(11) (2005).
- [59] Battistoni G. et al., *Overview of the FLUKA code*, Ann. Nucl. Energy, 82, 10–18 (2015).

- [60] Böhlen T. et al., *Benchmarking nuclear models of FLUKA and GEANT4 for carbon ion therapy*, Phys. Med. Biol., 55(19), 5833 (2010).
- [61] E. Scifoni et al., *Including oxygen enhancement ratio in ion beam treatment planning: model implementation and experimental verification*, Phys. Med. Biol., vol. 58, no. 11, p. 3871 (2013).
- [62] N. Bassler et al., *LET-painting increases tumour control probability in hypoxic tumours*, Acta Oncol., vol. 53, no. 1, pp. 25–32 (2014).
- [63] C. Grassberger and H. Paganetti, *Elevated let components in clinical proton beams*, Phys. Med. Biol., vol. 56, pp. 6677–6691 (2011).
- [64] F. Tommasino et al., *New ions for therapy*, Int. J. Part. Ther., vol. 2, no. 3, pp. 428–438 (2015).
- [65] R. Grün et al., *Assessment of potential advantages of relevant ions for particle therapy: A model based study*, Med. Phys., vol. 42, no. 2, pp. 1037–1047 (2015).
- [66] M. Rovituso et al., *Fragmentation of 120 and 200 MeV/u ^4He ions in water and PMMA targets*, Phys. Med. Biol., vol. 62, no. 4, p. 1310 (2017).
- [67] M. Krämer et al., *Helium ions for radiotherapy? Physical and biological verifications of a novel 2053 treatment modality*, Med. Phys., vol. 43, no. 4, pp. 1995–2004 (2016).
- [68] M. Marafini et al., *Secondary radiation measurements for particle therapy applications: nuclear fragmentation produced by ^4He ion beams in a PMMA target*, Phys. Med. Biol., vol. 62, no. 4, p. 1291 (2017).
- [69] The FOOT collaboration, *FOOT Conceptual Design Report* (2018).
- [70] M. Toppi et al., *Measurement of fragmentation cross sections of ^{12}C ions on a thin gold target with the FIRST apparatus*, Phys. Rev. C, vol. 93, no. 6 (2016).
- [71] Simos N. et al., *Demagnetization of $\text{Nd}_2\text{Fe}_{14}\text{B}$, $\text{Pr}_2\text{Fe}_{14}\text{B}$, and $\text{Sm}_2\text{Co}_{17}$ Permanent Magnets in Spallation Irradiation Fields*, IEEE T. Magn., 54 (2018).

- [72] www.iphc.cnrs.fr/PICSEL.html.
- [73] www.iphc.cnrs.fr/PLUME.html.
- [74] W. de Boer et al., *Measurements with a CMOS pixel sensor in magnetic fields*, Meth. A, vol. 487, no. 1, pp. 163–169 (2002).
- [75] Morrocchi M. et al., *Development and characterization of a E-TOF detector prototype for the FOOT experiment*, Nuclear Instruments and Methods in Physics Research (2018).
- [76] G. De Lellis et al., *Nuclear emulsions*, in CW Fabjan and H Schopper, "Elementary Particles: Detectors for Particles and Radiation", vol. 21B, Springer (2011).
- [77] T. Nakamura et al., *The OPERA film: New nuclear emulsion for large-scale, high-precision experiments*, Nucl. Instrum. Meth. A, vol. 556, no. 1, pp. 80–86 (2006).
- [78] De Lellis G. et al., *Emulsion Cloud Chamber technique to measure the fragmentation of a high-energy carbon beam*, J. Instrum., 2(06), P06004 (2007).
- [79] De Lellis G. et al., *Measurement of the fragmentation of Carbon nuclei used in hadron-therapy*, Nucl. Phys. A, vol. 853, no. 1, pp. 124–134 (2011).
- [80] N. Armenise et al., *High-speed particle tracking in nuclear emulsion by last-generation automatic microscopes*, Nucl. Instrum. Meth. A, vol. 551, no. 2, pp. 261–270 (2005).
- [81] L. Arrabito et al., *Hardware performance of a scanning system for high speed analysis of nuclear emulsions*, Nucl. Instrum. Meth. A, vol. 568, no. 2, pp. 578–587 (2006).
- [82] Dudouet J. et al., *Double-differential fragmentation cross-sections measurements of 95 MeV/u ^{12}C beams on thin targets for hadrontherapy*, Phys. Rev. C, 88(2), 024606 (2013).
- [83] A. T. Collaboration, *The ATLAS Data Acquisition and High Level Trigger system*, Nucl. Instrum., vol. 11, no. 06, p. P06008 (2016).

- [84] C. Sbarra et al., *The data acquisition system of the superB-SVT beam test*, Nucl. Instrum. Meth. A, vol. 718, pp. 243–244 (2013).
- [85] A. Ferrari et al., *FLUKA: a multi-particle transport code*, CERN-2005-10, INFN TC 05/11, SLAC-R-773 (2005).
- [86] T. Böhlen et al., *Benchmarking nuclear models of FLUKA and GEANT4 for carbon ion therapy*, Phys. Med. Biol., 55(19), 5833 (2010).
- [87] S. Valle, *Design, simulation and performances study of the FOOT experiment*, Phd thesis, University of Milan (2019).
- [88] W. Cho et al., *OPTIMASS: a package for the minimization of kinematic mass functions with constraints*, J. High Energy Phys., vol. 2016, no. 1, p. 26 (2016).
- [89] G. D’Agostini, *A multidimensional unfolding method based on Bayes’ theorem*, Nucl. Instrum. Meth. A, 362(2-3), 487–498 (1995).
- [90] V.C. Klema and A.J. Laub, *The Singular Value Decomposition: its computation and some applications*, IEEE Transactions on Automatic Control, vol. AC-25, no. 2 (1980).
- [91] M. Morrocchi et al., *Development and characterization of a $\Delta E - TOF$ detector prototype for the FOOT experiment*, Nuclear Inst. and Methods in Physics Research, A 911 (2018).